Univerzita Karlova v Praze
Matematicko-fyzikální fakulta

DISERTAČNÍ PRÁCE

Radek Žlebčík

Studium produkce dijetů v difračních interakcích na HERA

Ústav částicové a jaderné fyziky

Vedoucí práce: RNDr. Alice Valkárová, DrSc.
Studijní program: Subjaderná fyzika (F9)

2015

Charles University in Prague
Faculty of Mathematics and Physics

DISSERTATION

Radek Žlebčík

Diffractive Dijet Production with a Leading Proton in *ep* Collisions at HERA

Institute of Particle and Nuclear Physics

Supervisor: RNDr. Alice Valkárová, DrSc.
Study programme: Subnuclear Physics (F9)

2015

Acknowledgements

I would like to express my gratitude towards Alice Valkárová who supervised this work from the very beginning, introduced me to the H1 Collaboration and was always there ready to help and keep supporting me during the studies. We spent many hours in fruitful discussions in Prague, in DESY or in conferences.

I would also like to thank to other members of the Prague H1 group, especially Karel Černý for his help with NLO calculations and H1 computational framework and Boris Pokorný who finalized his complementary diffractive analysis based on large rapidity gap selection in the same time period, thus we could share and confront our findings.

Let me also express my thanks to Laurent Favart, the author of many parts of the VFPS reconstruction code, who made me acquainted with this detector and spent a lot of his precious time by improving the physics reconstruction, often inspired by my reports. I am also grateful to Sergey Levonian who helped me to understand the H1 detector simulation procedure, which allowed me to implement the VFPS detector into the standard simulation chain.

My special thanks go to Stefan Schmitt for explanations concerning the unfolding algorithm used in this analysis and who provided a substantial help to finalize the physics paper based on the results of this thesis.

I apologise to all others, not explicitly mentioned in this short list, who provided stimulating remarks during the collaboration meeting or helped with their comments to improve readability and ensure correctness of statements in the resulting paper.

This work was supported by the following grants of Ministry of Education, Youth and Sports of the Czech Republic (MŠMT): 260219/2015, 260097/2014 and 267309/2013.

Prohlašuji, že jsem svou disertační práci napsal samostatně a výhradně s použitím citovaných pramenů. Souhlasím se zapůjčováním práce a jejím zveřejňováním.

Beru na vědomí, že se na moji práci vztahují práva a povinnosti vyplývající ze zákona č. 121/2000 Sb., autorského zákona v platném znění, zejména skutečnost, že Univerzita Karlova v Praze má právo na uzavření licenční smlouvy o užití této práce jako školního díla podle 60 odst. 1 autorského zákona.

V Praze dne February 24, 2016 Radek Žlebčík

Abstrakt: Tématem práce je měření účinného průřezu difrakční produkce dijetů v pozitron-protonových interakcích za použití detektoru H1 na urychlovači HERA. Difrakční interakce $e^+p \to e^+Xp$ jsou měřeny při těžišťové energii 319 GeV, systém X obsahuje nejméně dva jety a proton je detekován v H1 spektrometru VFPS. Měření je realizováno ve fotoprodukčním režimu definovaném virtualitou fotonu $Q^2 < 2\,\mathrm{GeV}^2$ a v hlubokém nepružném rozptylu s $4\,\mathrm{GeV}^2 < Q^2 < 80\,\mathrm{GeV}^2$. Výsledky jsou srovnány s QCD výpočty vyššího řádu založenými na difrakčních partonových distribučních funkcích získaných z měření inkluzivního účinného přůřezu v difrakčním hluboce nepružném rozptylu. Platnost kolineární QCD faktorizace je testována s využitím naměřených účinných průřezů a jejich poměrů.

Klíčová slova: difrakce, dijety, narušení faktorizace, fotoprodukce, DIS

The cross section of the diffractive process $e^+p \to e^+Xp$ is measured at a centre-of-mass energies of 319 GeV, where the system X contains at least two jets and the leading final state proton p is detected in the H1 Very Forward Proton Spectrometer. The measurement is performed in photoproduction defined by photon virtualities $Q^2 < 2\,\mathrm{GeV}^2$ and in deep-inelastic scattering with $4\,\mathrm{GeV}^2 < Q^2 < 80\,\mathrm{GeV}^2$. The results are compared to next-to-leading order QCD calculations based on diffractive parton distribution functions as extracted from measurements of inclusive cross sections in diffractive deep-inelastic scattering. A collinear QCD factorization theorem is tested against the measured cross sections and their ratios.

Keywords: diffraction, dijet, factorization breaking, photoproduction, DIS

Contents

1 Introduction **4**

2 Theory **7**

2.1 Deep inelastic scattering . . . 7

2.1.1 Kinematics . . . 7

2.1.2 Cross section . . . 8

2.1.3 Parton Model . . . 9

2.2 Quantum Chromodynamics . . . 11

2.2.1 The Hard QCD Factorization in DIS . . . 13

2.3 Diffraction . . . 16

2.3.1 The Regge theory . . . 16

2.3.2 Diffraction . . . 19

2.3.3 Diffraction in ***ep*** Scattering . . . 20

2.3.4 Regge Phenomenology of Diffractive ***ep*** Scattering . . . 22

2.3.5 Factorization in inclusive DIS . . . 23

2.3.6 Diffractive Dijet Production in *ep* Scattering . . . 25

2.3.7 Factorization Breaking in Diffraction . . . 27

2.3.8 Experimental Signature of Diffractive Events . . . 29

2.4 Monte Carlo Generators . . . 33

2.5 NLO QCD Predictions . . . 35

2.6 Jet algorithm . . . 35

3 Experimental Setup **37**

3.1 The HERA Collider . . . 37

3.2 The H1 Detector . . . 39

3.2.1 Tracking System . . . 40

3.2.2 Calorimetry . . . 40

3.2.3 Luminosity System . . . 43

3.2.4 Triggering System . . . 45

4 Overview or Diffractive Measurements **47**
4.1 Inclusive Diffractive DIS . . . 47
4.2 Proton Vertex Factorization . . . 50
4.3 Dijet production in diffractive DIS . . . 51
4.4 Diffractive Dijet Production in Hadron-Hadron Collisions . . . 53
4.5 Diffractive Dijet Photoproduction . . . 55

5 Data Selection and Reconstruction **60**
5.1 Analysed Data Sample . . . 60
5.2 MC Samples . . . 61
5.3 Reconstruction of the Kinematics . . . 63
5.3.1 Leading Proton Kinematics . . . 63
5.3.2 Reconstruction of the HFS Objects . . . 68
5.3.3 DIS Selection . . . 69
5.3.4 Photoproduction Selection . . . 70
5.4 Events Selection . . . 71
5.4.1 Phase Space Definition . . . 71
5.4.2 Trigger selection . . . 72
5.4.3 Vertex Reconstruction . . . 76
5.4.4 The VFPS Selection Criteria . . . 76
5.4.5 Jet Selection . . . 78
5.4.6 Selection of the Photoproduction Events . . . 78
5.4.7 Selection of the DIS Events . . . 80
5.5 Quality of the Detector Simulation and Variables Reconstruction . . . 81

6 Cross Section Measurement **89**
6.1 Correction for the Detection Uncertainties . . . 89
6.1.1 Bin-By-Bin Unfolding Method . . . 89
6.1.2 Purities and Stabilities . . . 90
6.1.3 Regularized Unfolding . . . 93
6.2 Structure of the migration matrix . . . 96
6.3 Systematic Uncertainties . . . 98
6.3.1 Detector Systematic Uncertainties . . . 99
6.3.2 Model Systematic Uncertainties . . . 101
6.4 Hadronization Corrections . . . 105
6.5 Radiative Corrections . . . 105

7 Results **112**
7.1 Integrated Cross Sections . . . 112
7.2 The Differential Diffractive Dijet Cross Sections in DIS . . . 113
7.3 The Differential Diffractive Dijet Cross Sections in Photoproduction . 115

7.4 The Double Ratio of the PHP and DIS Cross Sections 118

8 Conclusion **125**

Chapter 1

Introduction

Processes, $ep \to eXY$, where the systems X and Y are separated by a large non-exponentially suppressed gap in rapidities of the final state particles, have been extensively studied at the electron-proton collider HERA. They can be viewed as being mediated by exchange of quantum numbers of vacuum, usually referred to as a pomeron ($I\!P$), which in turn explains why the system Y often contains only the intact initial state proton with slightly changed kinematics. Such processes are called diffractive. Both the leading proton or gap observation are experimentally used methods for identification of diffractive processes, where the latter one allows the proton to dissociate into states of relatively small masses if compared with total energy of the interaction. If a hard scale can be defined in the system X (associated with the dissociated virtual photon), perturbative approach to Quantum Chromodynamics (p-QCD) is applicable and we speak of hard diffraction. Apart from these extra requirements, the diffractive processes obey the standard definitions of deep inelastic scattering (DIS). In the framework of the collinear factorization theorem [1] diffractive parton distribution functions (DPDFs) may be defined. The factorization theorem predicts that the cross section can be expressed as a convolution of non-perturbative DPDFs and partonic cross sections of the hard subprocess, calculable within p-QCD. The DPDFs have properties similar to the parton distribution functions of the proton, but with the diffractive constraints. The H1 experiment was equipped with two dedicated detectors, the Forward Proton Spectrometer [2] and the Very Forward Proton Spectrometer (VFPS) [3] designed to detect the leading protons.

The mostly used DPDFs from HERA were obtained in analyses of large samples of inclusive diffractive deep-inelastic scattering (DDIS) data [4, 5]. Given the DPDFs, perturbative QCD calculations are expected to be applicable to other processes such as jet and heavy quark production in DDIS[6–9]. Next-to-leading order (NLO) QCD predictions using DPDFs describe these measurements well.

The universality of the DPDFs measured at HERA and the factorization approach

is, however, called into question by measurements of diffractive hadron-hadron interactions, where production of jets was found to be suppressed by about one order of magnitude [10, 11] if compared with predictions based on HERA DPDFs. This observation is often explained by additional partonic interactions between both hadrons which destroy the diffractive event signature [12, 13] and, thus, leading to factorization breaking.

The issues of DPDF applicability and factorization breaking can be also studied in hard diffractive photoproduction (γp), where the virtuality of the exchanged photon Q^2 is close to zero. In leading order, the small photon virtualities allow for partonic fluctuations $\gamma \to q\bar{q}$ that live long enough to interact with the partons in the proton. In that case, only a fraction x_γ of the photon's four-momentum is expected to participate in the hard interaction. Such interactions, where the photon exhibits a hadronic structure, are named "resolved". Still, the photon may couple directly to the partons of the proton and these interactions are then referred to as "direct". The direct photon interactions dominate in DIS. A distinction between these two γp regimes can be made by x_γ which is expected to be equal to one at parton level for the direct contribution and it is expected to be smaller than one in case of the resolved processes.

Factorization breaking effects in diffraction may be expected at HERA $x_\gamma < 1$ where the photoproduction processes resemble hadron-hadron interactions. Looking into greater detail, the resolved photon interactions can be further divided into a hadron-like contribution and an anomalous or point like contribution, the latter one arising from the inhomogeneous term in the PDF evolution equation for the photon [14]. The point-like contribution to the photon structure is expected to be subject to smaller absorptive corrections than the hadron-like part [15] and may generate factorization breaking effects in diffractive photoproduction which are then slightly dependent on the jet transverse energies E_T. Typical suppression factors predicted by this model are $0.7 \div 0.8$ [15].

Diffractive photoproduction of dijets in ep collisions at HERA were measured by H1 [16, 17] and ZEUS [18]. In each of these measurements, diffractive events were selected by requiring a large rapidity gap. Contrary to the expectations, no significant dependence of the ratio of data to the NLO QCD predictions on x_γ was observed. However, different ratios have been measured by H1 and ZEUS: while H1 reported their data to be suppressed by a factor of 0.6 with respect to the next-to-leading order QCD prediction [16, 17], the ZEUS data are compatible with the hypothesis of no factorization breaking [18]. The ZEUS analysis covered somewhat different kinematic region, especially the higher transverse energies of leading and subleading jets were required.

A reliable method to test QCD factorization, first applied at HERA in [17], is given by the examination of the double ratio of measured to predicted cross sections in diffractive photoproduction to the corresponding ratio in diffractive DIS. The double ratios profits from cancellations of many of the experimental and theoretical uncer-

tainties.

In this thesis, new measurements of diffractive dijet cross sections in DIS and photoproduction are presented. The data were collected in the years 2006-2007 with a total integrated luminosity of $30\,\mathrm{pb}^{-1}$ for diffractive photoproduction and $50\,\mathrm{pb}^{-1}$ for diffractive DIS. For the identification of diffractive events, the leading protons are detected in the Very Forward Proton Spectrometer. The results are compared with NLO QCD predictions and the factorization theorem is tested by investigation of the double ratio of the diffractive PHP and DDIS data to the respective prediction.

Chapter 2

Theory

2.1 Deep inelastic scattering

2.1.1 Kinematics

In this section, the kinematic invariants describing the lepton-hadron scattering are introduced. This process can be mediated by charged ($W^{\pm}$) or neutral (γ^*, Z^0) exchange. Further, only neutral-current ep interactions

$$e(k) + p(P) \to e(k') + X(P_X) \tag{2.1}$$

are discussed, where e, p and X denote electron or positron, proton and an arbitrary hadronic system with their corresponding four-momenta, respectively (see Fig. 2.1). The four-momentum of the exchanged virtual photon[1] is denoted as $q = k - k'$.

Inclusive DIS kinematics can be described by the centre-of-mass (CMS) energy squared ($s = (k + P)^2$) and the following invariants:

$$Q^2 = -q^2, \qquad y = \frac{Pq}{Pk}, \qquad x = \frac{Q^2}{2Pq}, \tag{2.2}$$

where Q^2 is the virtuality of the exchanging photon, y is the inelasticity and x is the Bjorken scaling variable which can be interpreted within parton model as the proton momentum fraction entering to the hard subprocess (section 2.1.3).

Quantities in equations (2.2) are related by the formula:

$$xy \simeq \frac{Q^2}{s}, \tag{2.3}$$

where the proton mass squared M_P^2 was neglected with respect to s.

[1] Contribution originating from Z^0 exchange, distinguishing between e^+p and e^-p scattering, can be safely neglected, due to low virtuality of the exchange in this thesis.

Invariant mass of hadronic final state (HFS) system (M_X) is identical to $\gamma^* p$ centre-of-mass energy (W) and can be calculated as

$$W^2 = M_X^2 = (q+P)^2 = M_P^2 + \left(\frac{1}{x} - 1\right) Q^2. \tag{2.4}$$

Note that the ep elastic scattering ($W = M_P$) occurs if $x = 1$, otherwise $W > M_P$.

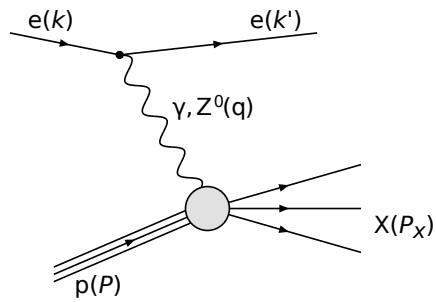

Fig. 2.1: The leading order Feynman diagram for DIS

2.1.2 Cross section

Process (2.1) is called deep inelastic scattering (DIS) if the virtual photon wavelength $\lambda \sim 1/Q$ is much smaller than the proton size (="deep") and if the invariant mass of the HFS system M_X is much higher than the proton mass (="inelastic"). Exchanging virtual photon acts here as a probe of the proton structure with a wavelength $\lambda \sim 1/Q$.

Further discussion is restricted to the kinematic region where the parity violating Z^0 contribution can be safely neglected ($Q^2 \ll M_Z^2$).

Fundamental principles – Lorentz invariance, parity conservation and gauge invariance of electromagnetic interactions constrain the DIS cross section to form

$$\frac{\mathrm{d}\sigma}{\mathrm{d}x\mathrm{d}Q^2} = \frac{4\pi\alpha_{em}^2}{Q^4}\left[\left(1 - y - \frac{M_P^2 xy}{s}\right)\frac{F_2(x,Q^2)}{x} + \frac{1}{2}y^2 2F_1(x,Q^2)\right], \tag{2.5}$$

where α_{em} is electromagnetic coupling constant and $F_{1,2}$ are the DIS structure functions of the proton.

For HERA energies the term containing proton mass can be safely neglected, in addition it can be shown that the $F_L = F_2 - 2xF_1$ is proportional to the cross section of scattering of longitudinally polarised virtual photon on a proton target. Eliminating F_1 and neglecting proton mass term, the relation (2.5) can be expressed as:

$$\frac{\mathrm{d}\sigma}{\mathrm{d}x\mathrm{d}Q^2} = \frac{4\pi\alpha_{em}^2}{Q^4}\left[\left(1 - y + \frac{1}{2}y^2\right)\frac{F_2(x,Q^2)}{x} - \frac{1}{2}y^2\frac{F_L(x,Q^2)}{x}\right]. \tag{2.6}$$

In principle, it is impossible to determine both F_2 and F_L structure functions only from differential cross section for single s.

Therefore, the differential cross sections must be measured at least for two CMS energies $\sqrt{s}$. Then if the $\frac{\mathrm{d}\sigma}{\mathrm{d}x\mathrm{d}Q^2}$ is measured for both these energies $\sqrt{s}$ but the same x and Q^2, the structure functions $F_2(x, Q^2)$ and $F_L(x, Q^2)$ are equal for both energies whereas values of y-termes in formula (2.6) differ, because $y = \frac{Q^2}{xs}$. This approach provides two linear equations for two variables F_2 and F_L.

Experimentally the longitudinal structure function F_L was found to be small [19] and is often neglected. The DIS data are often conveniently shown in terms of the reduced cross section σ_r which is defined by the relation

$$\frac{\mathrm{d}\sigma}{\mathrm{d}x\mathrm{d}Q^2} = \frac{4\pi\alpha_{em}^2}{xQ^4}\left(1 - y + \frac{1}{2}y^2\right)\sigma_r(x, Q^2). \tag{2.7}$$

Compared to the differential cross section $\frac{\mathrm{d}\sigma}{\mathrm{d}x\mathrm{d}Q^2}$ which varies across several orders of magnitude, $\sigma_r \simeq F_2$ has a weaker dependence on x and Q^2.

2.1.3 Parton Model

Flatness of the F_2 with respect to the Q^2 observed in ep scattering at SLAC [19] (Fig. 2.2) led to assumption that electron is scattered on point-like proton's constituents.

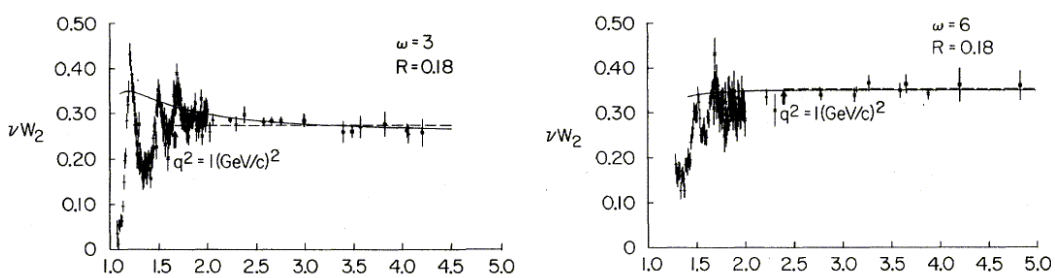

Fig. 2.2: SLAC measurement of $F_2 = \nu W_2$ as a function of $W = Q\sqrt{1/x - 1}$ [GeV] for $x = 1/3$ (left) and $x = 1/6$ (right). Above the resonance region, the F_2 is observed to behave, within the experimental precision, as a constant.

A model was formulated where proton is composed of quasi-free massless objects called partons and consequently γ^* interacts only with individual one while others act as spectators (Fig. 2.3). The fact that these proton's constituents are not observed in the final state is explained by the hadronization phenomenon, occurring at distance around 1 fm corresponding to time $\sim \frac{1}{0.2\,\mathrm{GeV}}$ in the natural units. This parton model picture is applicable if hadronization and hard interaction are well separated in time

and space (Fig. 2.3). Naturally only electrically charged partons are allowed to couple to the photon. If $\tilde{x}$ is the momentum fraction of such parton with respect to the proton momentum, then the zero mass of the scattered parton leads to condition:

$$(\tilde{x}P + q)^2 = 0 \quad \rightarrow \quad \tilde{x} = \frac{Q^2}{2Pq}, \tag{2.8}$$

where the proton mass squared was neglected with respect to Q^2. Formula for $\tilde{x}$ is identical to the definition (2.2) of x, therefore, the Bjorken x has interpretation as the momentum fraction of the struck parton with respect to the proton momentum.

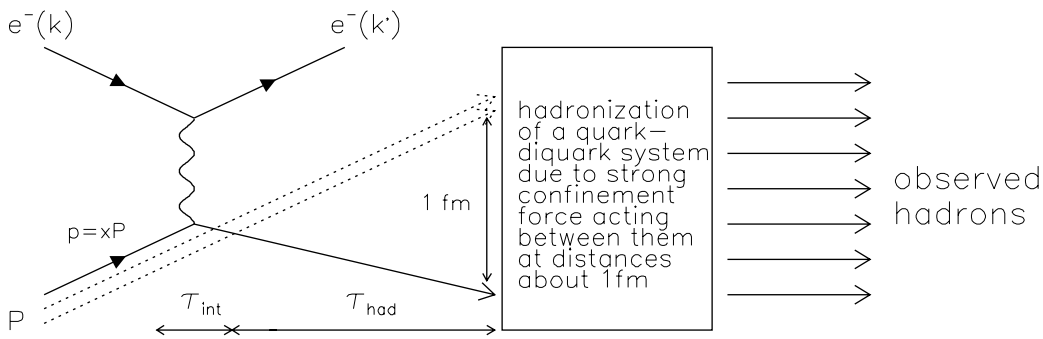

Fig. 2.3: Feynman diagram showing ep interaction within the parton model. Partons which act as spectators are depicted by dashed line. Interaction time is approximately $\tau_{\text{int}} \sim 1/Q$, whereas hadronization starts around $\tau_{\text{had}} \sim 1/\Lambda_{QCD}$ ($\Lambda_{QCD} \simeq 0.2\,\text{GeV}$) after the γ^*-parton interaction [20].

To derive characteristics resulting from parton model, the scattering of two charged particles of spin 1/2 (electron and parton) and negligible masses is considered. According to the quantum electrodynamics (QED) the differential cross section in the lowest order equals to

$$\frac{\mathrm{d}\sigma}{\mathrm{d}Q^2} = \frac{4\pi\alpha_{em}^2}{Q^4}\left(1 - y + \frac{1}{2}y^2\right)e_q^2, \tag{2.9}$$

where e_q denotes electric charge of interacting parton. This formula resembles first term in equation (2.6) under the assumption that proton is composed of charged partons with spin 1/2. If the charged partons were bosons with spin 0 or 1 the scattering formula analogous to (2.9) would not be consistent with experiments. Proton structure function F_2 within parton model then fulfills:

$$\frac{F_2(x, Q^2)}{x} = \sum_i e_i^2 \left(q_i(x) + \overline{q}_i(x)\right), \tag{2.10}$$

where $q_i(x)\mathrm{d}x$ or $\overline{q}_i(x)\mathrm{d}x$ denotes the probability that a parton or anti-parton, respectively, of type i with momentum fraction in interval $(x,x+dx)$ is found inside proton.

Note that F_2 does not depend on Q^2, in agreement with experimental data [19] available at the time when parton model emerged, and the F_L is predicted to be zero which is known as a Callan-Gross relation [21].

From the measurements, it was found that the parton distribution functions (PDF) behave as $\sim x^{-1.5}$ in the small x limit, so the mean number of partons of type i inside proton $(\int_0^1 q_i(x)\,\mathrm{d}x)$ goes hypothetically to infinity. The quantities which relate to the constituent quarks from additive SU(3) quark model [22] are so-called valence distributions

$$q_i^{val}(x) = q_i(x) - \overline{q}_i(x). \tag{2.11}$$

Mean numbers of valence u and d quarks inside the proton are then 2 and 1, respectively, in agreement with additive quark model. The flavour index i denotes up, down, strange, charm, bottom or top quark, but usually only u and d quarks have non-zero valence quark distribution functions for proton.

By means of the electron-nucleon scattering the total momentum fraction carried by all quarks in proton:

$$\int_0^1 \mathrm{d}x\, x\Sigma(x) = \int_0^1 \mathrm{d}x\, x \sum_i (q_i(x) + \overline{q}_i(x))\mathrm{d}x \tag{2.12}$$

can be measured. Value around 0.5, obtained at the early experiments, signaled that there must have been other, electrically neutral partons carrying the remaining half of proton's momentum. These partons were identified as gluons well known from quantum chromodynamics.

2.2 Quantum Chromodynamics

Quantum chromodynamics (QCD) is a non-abelian gauge theory of strong interaction based on SU(3) group which describes interactions between quarks with spin 1/2 by exchange of gluons – massless gauge bosons with spin 1. Each quark has a color ("strong charge"), analogous to the electric charge in quantum electrodynamic (QED). Contrary to quantum electrodynamics, gluons carry color too; therefore interactions between gluons are possible. There exist three colors for quarks and eight colors for gluons which corresponds to the dimension of the fundamental representation and the adjoint representation of SU(3) color group.

Strong interaction is characterized by a strong coupling constant α_s. If this constant is sufficiently small, calculated cross section can be expanded into the perturbative power series of α_s, where coefficients are calculated from corresponding Feynman

diagrams. This approach leads to ultraviolet divergences in higher orders of this expansion coming from the integration over large values of loop momenta. Problem with infinite integrals was resolved by so-called renormalization procedure [23, 24], where the divergent terms are absorbed in the newly defined renormalized quantities, making the coefficients in the perturbative expansion finite. Within this procedure, the renormalization scale μ_r^2 is introduced and the renormalized quantities (coupling, wave functions, particle masses) depend on this scale. However, any measurable quantity should not in principle depend on an arbitrary scale μ_r^2. This condition leads to renormalization group equation, which quantifies the fact that the μ_r^2 dependence of a physical observable $O(\mu_r^2, \alpha_s)$ is compensated by "opposite dependence" of α_s on μ_r^2[2]:

$$\mu_r^2 \left(\frac{\partial O}{\partial \mu_r^2} + \frac{\partial O}{\partial \alpha_s} \frac{\partial \alpha_s}{\partial \mu_r^2} \right) = 0. \tag{2.13}$$

Within perturbative QCD (p-QCD) approach, the cancellation of μ_r^2 dependence in equation (2.13) is required up to the order of perturbative calculations. Scale dependence originating from higher orders in α_s still persists and makes results obtained by p-QCD in reality scale dependent. In addition an ambiguity in the renormalization procedure known as renormalization scheme exists. The most frequently used renormalization scheme $\overline{\text{MS}}$ [25] is based on dimensional regularisation of the integrals. All these unphysical dependencies diminish with increasing order of perturbative calculation.

According to the renormalization group equation, α_s must satisfy the differential equation

$$\frac{\partial \alpha_s}{\partial \ln \mu_r^2} = \beta(\alpha_s) = -\alpha_s \left(\beta_0 \alpha_s + \beta_1 \alpha_s^2 + \cdots \right), \tag{2.14}$$

where coefficients β_i of the β-function [26, 27] are calculated using perturbative QCD. First two β-coefficients are renormalization scheme independent and are functions of the number of active flavour N_f only:

$$\beta_0 = \frac{33 - 2N_f}{12\pi} \qquad \beta_1 = \frac{153 - 19N_f}{24\pi^2}. \tag{2.15}$$

Negative sign of β_0 term in (2.14) results in a decrease of α_s for growing renormalization scale, so for very high energy (small distance) the strength of the strong interaction is negligible. This famous result derived for non-abelian quantum field theories is known as asymptotic freedom [28]. Such behavior especially justifies validity of the parton model in high Q^2 (=high scale μ_r^2) region where α_s is small and therefore electromagnetic interactions dominate. On the other hand for small scales (close to the QCD scale parameter Λ) the strong coupling constant grows which leads to divergence of the perturbative series and therefore to non-applicability of the perturbative theory.

[2] Quark masses are neglected in this simplified discussion.

The approximate solution of (2.14) up to term proportional to $\beta_1 \alpha_s^3$ can be expressed as

$$\alpha_s(\mu_r^2) = \frac{1}{\beta_0 \ln \mu_r^2/\Lambda_{N_f}^2} - \frac{\beta_1}{\beta_0^3} \frac{\ln \ln \mu_r^2/\Lambda_{N_f}^2}{\ln \mu_r^2/\Lambda_{N_f}^2}, \tag{2.16}$$

where the QCD scale $\Lambda_4 \doteq 0.3\,\mathrm{GeV}$ or $\alpha_s(M_Z) \doteq 0.118$ must be determined from experiment. Dependence of the strong coupling constant on μ_r is illustrated in Fig. 2.4.

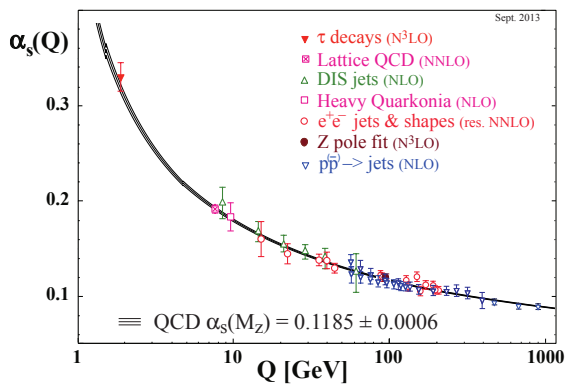

Fig. 2.4: Strong coupling constant α_s as a function of renormalization scale $\mu_r = Q$. Several experimental data points are depicted for scales tween 2 GeV and 900 GeV [29].

The fact that the strength between "color charges" grows with distance causes that only color neutral objects (hadrons) can be stable making the direct observation of quarks (with fractional electric charge) or gluons impossible. This phenomenon is known as confinement [30].

2.2.1 The Hard QCD Factorization in DIS

Perturbative Quantum Chromodynamics enables us to calculate the QCD corrections to the "zero-order" DIS cross section in α_s (2.9), the QED corrections are usually much smaller. In the leading order in α_s, there are QCD-Compton and boson(=photon)-gluon fusion processes (see Fig. 2.5)

$$\gamma^* q \to qg \qquad \gamma^* g \to q\bar{q}. \tag{2.17}$$

Both of them exhibit a divergent behavior of the cross section for small scattering angles. These infrared divergences can be regularised by imposing limit χ on the transverse momenta of the scattered partons for processes (2.17), $|\hat{p}_T^2| > \chi^2$.

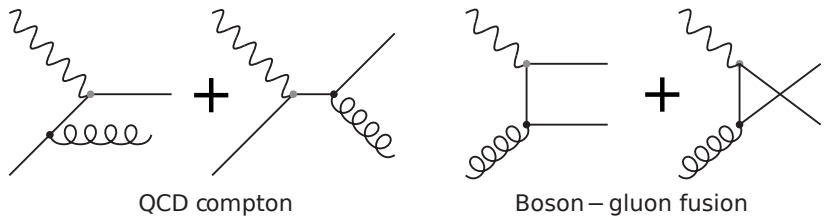

Fig. 2.5: The leading order α_s Feynman diagrams for DIS, $\gamma^* q$ (left) and $\gamma^* g$ scattering (right).

Then the dominant part of F_2 structure function, associated with inclusive DIS cross section, in the leading-order takes form (index j runs over quarks and anti-quarks):

$$\frac{F_2}{x} = \sum_j e_j^2 \left[q_j^{(0)}(x) + \frac{\alpha_s}{2\pi} \int_x^1 \frac{d\xi}{\xi} \left(q_j^{(0)}(\xi) P_{qq}(\frac{x}{\xi}) + g^{(0)}(\xi) P_{qg}(\frac{x}{\xi}) \right) \log \frac{Q^2}{\chi^2} \right]. \quad (2.18)$$

The first α_s^0-term corresponds to the parton model result, the second to QCD-Compton and the third to boson-gluon fusion process. The $P_{qq}(z)$ and $P_{pg}(z)$ are so-called splitting functions [31, 32] representing probability of quark (gluon) to emit quark with momentum fraction z.

To get rid of the cut-off parameter dependence, the factorization scale dependent parton distribution functions $q_j(x, \mu_f^2)$ are introduced

$$q_j(x, \mu_f^2) = q_j^{(0)}(x) + \frac{\alpha_s}{2\pi} \int_x^1 \frac{d\xi}{\xi} \left[q_j^{(0)}(\xi) P_{qq}\left(\frac{x}{\xi}\right) + g^{(0)}(\xi) P_{qg}\left(\frac{x}{\xi}\right) \right] \log \frac{\mu_f^2}{\chi^2}. \quad (2.19)$$

After the substitution:

$$\frac{F_2}{x} = \sum_j e_i^2 \left[q_j(x, \mu_f^2) + \frac{\alpha_s}{2\pi} \int_x^1 \frac{d\xi}{\xi} \left(q_j(\xi, \mu_f^2) P_{qq}\left(\frac{x}{\xi}\right) + g(\xi, \mu_f^2) P_{qg}\left(\frac{x}{\xi}\right) \right) \log \frac{Q^2}{\mu_f^2} \right]. \quad (2.20)$$

The structure function F_2 as a physical observable cannot depend on the scale μ_f^2. Within perturbative theory this cancellation occurs order-by-order. If μ_f-dependency cancellation is imposed in (2.20) only for α_s^0 terms then the PDFs are predicted to be μ_f^2-scale independent which leads to the parton model relation (2.10). If also the α_s^1-part of F_2 is required to be not dependent on factorization scale, then by setting the derivative of F_2 according to μ_f^2 to zero follows:

$$\mu_f^2 \frac{\mathrm{d}q_j(x, \mu_f^2)}{\mathrm{d}\mu_f^2} = \frac{\mathrm{d}q_j(x, \mu_f^2)}{\mathrm{d}\log \mu_f^2} = \frac{\alpha_s(\mu_f^2)}{2\pi} \int_x^1 \frac{\mathrm{d}\xi}{\xi} \left[q_j(\xi, \mu_f^2) P_{qq}\left(\frac{x}{\xi}\right) + g(\xi, \mu_f^2) P_{qg}\left(\frac{x}{\xi}\right) \right] \quad (2.21)$$

Above formula represents one of the integro-differential equations known as an DGLAP evolution[31, 33]. They can be written in the shortened form using Mellin convolution defined as[3]:

$$F(x) = (u \otimes v)(x) = \int \mathrm{d}\xi \mathrm{d}z\, u(\xi) v(z) \delta(z\xi - x) = \int_x^1 \frac{\mathrm{d}\xi}{\xi} u(\xi) v\left(\frac{x}{\xi}\right). \tag{2.22}$$

Then the DGLAP equations take the form (index j runs over quarks and anti-quarks):

$$\frac{\mathrm{d}q_j(x,\mu_f^2)}{\mathrm{d}\ln\mu_f^2} = \frac{\alpha_s(\mu_f^2)}{2\pi}(P_{qq}^0 \otimes q_j + P_{qg}^0 \otimes g) \tag{2.23}$$

$$\frac{\mathrm{d}g(x,\mu_f^2)}{\mathrm{d}\ln\mu_f^2} = \frac{\alpha_s(\mu_f^2)}{2\pi}(\sum_j P_{gq}^0 \otimes q_j + P_{gg}^0 \otimes g). \tag{2.24}$$

These equations allow to calculate PDF at arbitrary scale μ_f^2 from knowledge of PDF at the initial scale μ_{f0}^2. The DGLAP evolution equations together with relation (2.20) are used in QCD fits of the inclusive DIS data $\sigma_r(x, Q^2)$ (Fig. 2.6, Fig. 2.7). The Bjorken Q^2 scaling predicted by the parton model is violated, especially at low-x region, where QCD corrections play the substantial role. On the other hand the predicted logarithmic Q^2 dependency is at higher x quite smooth, in example the constant dependency suggested in Fig. 2.2 for $x = 1/6$, where the reduced cross section was measured up to $Q^2 \simeq 5\,\mathrm{GeV}^2$, holds in reality up to $Q^2 \sim M_Z^2 \sim 10^4\,\mathrm{GeV}^2$.

Equation (2.20) can be rewritten as:

$$F_2(x, Q^2) = \sum_{i=q,\bar{q},g} \int_x^1 \mathrm{d}\xi f_i(\xi, \mu_f^2) \hat{F}_2^i \left(\frac{x}{\xi}, Q^2, \mu_f^2, \mu_r^2\right), \tag{2.25}$$

where $\hat{F}_2^i$ are the coefficient functions that can be calculated using Feynman graphs and are known up to $O(\alpha_s^3)$ [35]. In the lowest order coefficient functions $\hat{F}_2^q = e_q^2 \delta(1-z)$ and $\hat{F}_2^g = 0$ reproduce parton model result (2.10). Note that (2.25) contains both renormalization μ_r^2 and factorization μ_f^2 scales, which relate to subtraction of ultraviolet and infrared divergences of the perturbative calculations. For perturbative calculation up to $O(\alpha_s^N)$, the residual $O(\alpha_s^{N+1})$ uncertainty is associated with the ambiguity in choosing μ_r^2 and μ_f^2, for DIS, the default choice is usually $\mu_r^2 = \mu_f^2 = Q^2$.

Extension of (2.25) to production of the general system F (dijet, W, Z, ...) in collisions, where both beam particles $h_{1,2}$ have partonic structure, takes form

$$\sigma(h_1 + h_2 \to F + X) = \sum_{ij} \int\int \mathrm{d}x_1 \mathrm{d}x_2 f_{i/h_1}(x_1, \mu_f^2) f_{j/h_2}(x_2, \mu_f^2) \sigma_{ij}(x_1 x_2 s, \mu_r^2, \mu_f^2), \tag{2.26}$$

[3]Note that if u, v and F are probability density function, then holds $x^F = \xi^u \cdot z^v$, where i.e. ξ^u means that random variable ξ is distributed according to distribution function $u(\xi)$.

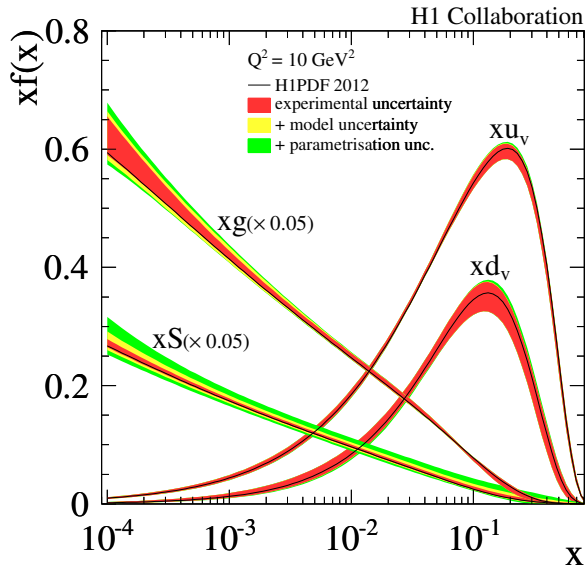

Fig. 2.6: The parton distribution functions at next-to-leading order and scale $\mu_f^2 = 10\,\mathrm{GeV}^2$ of valence u-quark, valence d-quark, sea-quarks and gluon as measured by H1 collaboration [34]. For better visibility, the gluon and sea-quarks distribution functions are multiplied by factor of 0.05.

where σ_{ij} is a partonic subprocess cross section of F production obtained by p-QCD.

Equations (2.25) and (2.26) are manifestations of so-called QCD collinear factorization theorem. It states that a cross section can be expressed as a convolution of universal non-perturbative PDFs of colliding particles and perturbative cross section of the hard subprocess, calculable within p-QCD. Albeit factorization theorem is widely used in perturbative QCD calculation, only a few processes exist, where it has been rigorously proven [36].

2.3 Diffraction

2.3.1 The Regge theory

Since 60th, the Regge theory represents experimentally successful phenomenological approach to describe hadron-hadron interactions. It is based on the unitarity, analyticity and crossing symmetry of the S-matrix [37].

The key idea is an analytical extrapolation of the partial wave amplitudes $a_l(t)$, where l is the integer angular momentum, into the complex values of l, in the t-

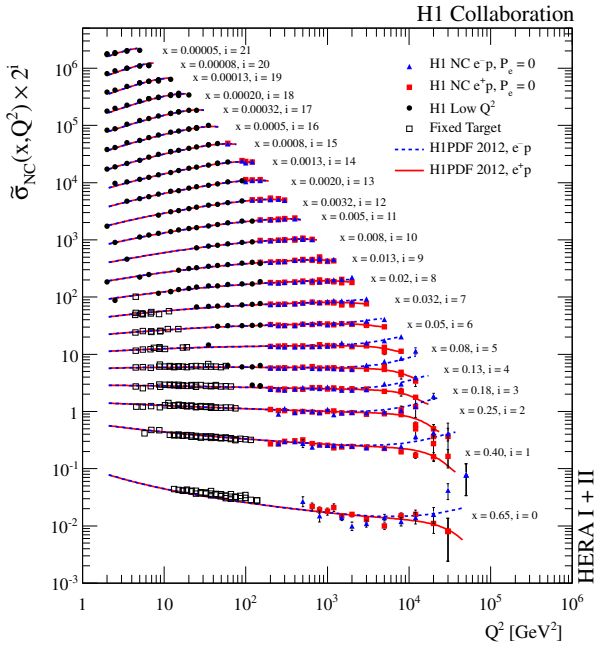

Fig. 2.7: Neutral current DIS reduced cross sections $e^{\pm}p \to eX$ for several x values as a function of Q^2 [34]. Along the data points results of QCD DGLAP fits are plotted. The e^+ and e^- cross sections vary due to non-negligible electroweak exchange contribution at higher Q^2.

channel[4]. This extrapolation was shown to be unique.

Then the asymptotic high energy behavior of the s-channel process amplitude is driven by leading singularity in the l-plane of $a_l(t)$, i.e. the singularity which has the highest "real-coordinate".

To demonstrate this property, let's consider asymptotic high-energy behavior of the hadron-hadron cross section. Many low-energy mesonic resonances exist, which can be considered as exchanging objects, but in Fig. 2.8 only leading resonances, i.e. resonances with the largest Re(α) of the corresponding Regge pole, are plotted into $t-\alpha$ plane, where t is the mass square and α spin of the resonance (l was renamed to α to empathize that it can have complex values).

Points in Fig. 2.8 can be fitted by linear function

$$\alpha(t) = \alpha(0) + \alpha' t, \tag{2.27}$$

where $\alpha(0) \simeq 0.5$ and $\alpha' \simeq 1$ GeV^{-2} which is called reggeon trajectory.

[4]For reaction $1 + 2 \to 3 + 4$ (s-channel) hold $s = (p_1 + p_2)^2$, $t = (p_1 - p_3)^2$, $u = (p_1 - p_4)^2$. These relations hold also for $1 + \bar{3} \to \bar{2} + 4$ (t-channel), where for instance $\bar{3}$ is antiparticle of 3. Particle i has four-momentum p_i and antiparticle $\bar{i}$ $-p_i$.

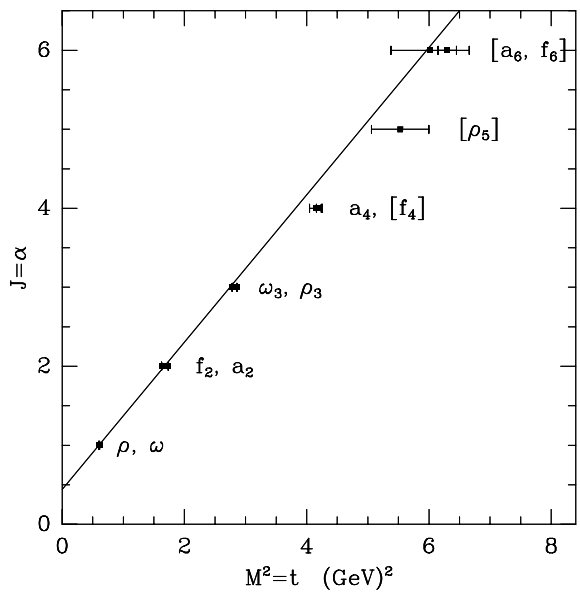

Fig. 2.8: The leading mesonic trajectory (reggeon) superposed by corresponding resonances [38]

It could be shown that the s-channel amplitude in the Regge limit $s \gg |t|$ then behaves asymptotically as

$$A(s,t) \sim \mathrm{i}s^{\alpha(t)}. \tag{2.28}$$

The total cross section is according to the optical theorem given as the imaginary part of the forward amplitude $A(s,0)$ divided by s:

$$\sigma_{tot} \sim s^{\alpha(0)-1}. \tag{2.29}$$

Accordingly, the equation (2.29) predicts for $\alpha(0) \simeq 0.5$ asymptotic decrease of the total cross section with growing energy.

In reality the opposite was observed (Fig. 2.9). To explain this behavior the new trajectory with $\alpha(0) \simeq 1.1$ named pomeron (IP) was introduced. The pomeron trajectory does not correspond to any known particles because all have intercepts $\alpha(0) \leq 0.5$ and is expected to be made by glueballs rather than conventional particles [39] which are being studied using lattice QCD calculations [40]. As a dominant trajectory in the elastic processes, pomeron possesses quantum numbers of the vacuum.

Regge fits made by leading (pomeron) and second leading (reggeon) trajectories are able to sufficiently describe the present-day total cross sections data

$$\sigma = A_{IP}s^{\alpha_{IP}(0)-1} + A_{IR}s^{\alpha_{IR}(0)-1}, \tag{2.30}$$

although power-like rising of total cross section violates unitarity Froissart-Martin bound $\sigma_{tot} < C \ln^2 s$ at extremely large energies $\sqrt{s}$ [41, 42].

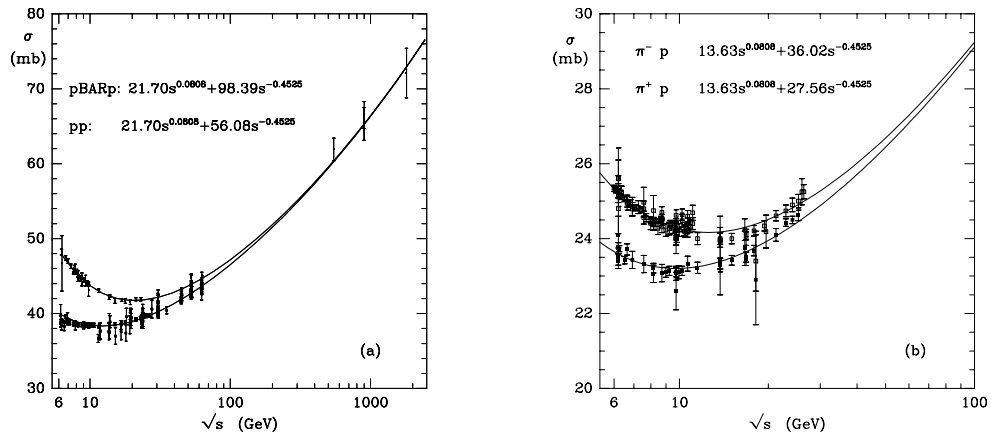

Fig. 2.9: The total cross section of pp, $p\bar{p}$ and $\pi^{\pm}p$ as a function of CMS energy $\sqrt{s}$ [38]. The cross sections measurements are shown together with Donnachie Landshof fit (2.30).

Up to now only elastic and total cross sections were considered. Regge phenomenology can predict also single inclusive $1+2 \to 1' + X$[5] cross section if Mueller's generalisation of optical theorem is employed [43]. This theorem transforms single inclusive process into three-body elastic reaction $1+2+\bar{1}' \to 1+2+\bar{1}'$ where Regge framework of complex angular momenta is applicable.

2.3.2 Diffraction

Diffractive effects were originally known from optics, where the diffractive pattern appears, when the light's wavelength is comparable to the size of the obstacle. In the nuclear high-energy physics, the term "diffraction" was introduced by Landau in 1953 [44]. Diffraction can be defined as "a reaction in which no quantum numbers are, at high energies, exchanged between the colliding particles" [45].

This definition is general enough (Fig. 2.10) to cover elastic scattering

$$1 + 2 \to 1' + 2', \tag{2.31}$$

single dissociation

$$1 + 2 \to 1' + X_2 \tag{2.32}$$

and double dissociation

$$1 + 2 \to X_1 + X_2. \tag{2.33}$$

[5]The system X is arbitrary hadronic state excluding particle $1'$.

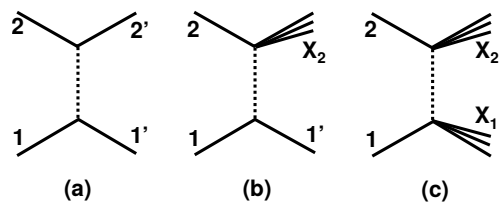

Fig. 2.10: The overview of diffractive processes: elastic scattering (a), single dissociation (b) and double dissociation (c). The exchange with vacuum quantum numbers is depicted by the dashed line.

Where the system X_1 (X_2) has the same quantum numbers as the beam particle 1 (2).

From the empirical point of view, the usage of the definition above is problematic if the final state is not fully reconstructed. In this case the another equivalent definition is beneficial [46]:

"A diffractive reaction is characterized by a large, non-exponentially suppressed, rapidity gap in the final state."

An equivalence of these two definitions follows from the Regge theory. The rapidity, y, is a dimensionless variable frequently used in particle physics[6]. For particle with energy E and momenta $\vec{P} = (P_x, P_y, P_z)$ it is defined as:

$$y = \frac{1}{2} \ln \frac{E + P_z}{E - P_z}. \tag{2.34}$$

Difference in rapidities of two particles is invariant under the Lorentz boost along the z-axis. For very relativistic particles the rapidity corresponds to pseudorapidity $\eta = -\ln \tan \frac{\theta}{2}$, where θ is the polar angle of the particle's momentum.

For example in pp interactions, the maximally possible rapidity gap is $\ln \frac{s}{M_p^2}$, which corresponds to elastic scattering with negligible transverse momenta of the scattered protons in the final state. If one or both beam protons dissociate or gain transverse momenta, then the final state rapidity gap is smaller.

2.3.3 Diffraction in *ep* Scattering

In the ep interactions, the diffraction is observed when the virtual photon γ^* radiated from electron dissociated into hadronic system X, whereas the beam proton stays intact (four-momenta names designed to individual objects are displayed in Fig. 2.11):

$$\gamma^* + p \to X + p. \tag{2.35}$$

[6]Do not confuse with kinematic invariant y denoting inelasticity of the DIS.

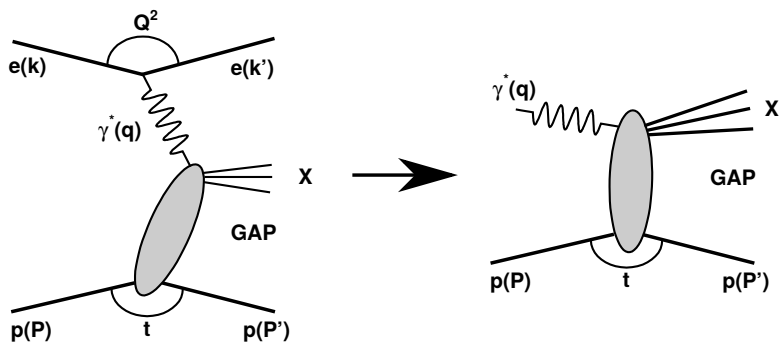

Fig. 2.11: The Feynman diagram of $ep \to epX$ scattering (left) and the "underlying" diffractive process $\gamma^* p \to Xp$ (right).

It is a special case of single dissociative diffractive process (2.32). Masses of all objects must be much smaller than the CMS energy of $\gamma^* p$ collision, i.e. $Q^2 \ll W^2$ and $M_X^2 \ll W^2$, and scattered proton and system X are typically separated by a large rapidity gap.

Kinematics of the diffractive reaction $ep \to epX$ is described by DIS invariants x, y, Q^2 defined before and newly introduced quantities related to the scattered proton. They are the fractional energy loss of the scattered proton:

$$x_{IP} = \frac{q(P - P')}{qP} \simeq \frac{M_X^2 + Q^2}{W^2}, \tag{2.36}$$

which is sometimes also called ξ and is at HERA typically ~ 0.01[7] and the four-momentum transfer squared at the proton vertex:

$$t = (P - P')^2, \tag{2.37}$$

which corresponds approximately to the transverse energy of the scattered proton as $t \simeq -P_T'^2$ and is rather small at HERA, $|t| \sim 0.1\,\mathrm{GeV}^2$.

It is convenient to introduce additional invariant denoted as β

$$\beta = \frac{x}{x_{IP}} = \frac{Q^2}{2q(P - P')} \simeq \frac{Q^2}{M_X^2 + Q^2}, \tag{2.38}$$

whose meaning will be explained later.

Sometimes the scattered proton dissociates into low mass hadronic system as well, which is conventionally denoted as Y

$$\gamma^* p \to XY. \tag{2.39}$$

[7]The x_{IP} variable must be small due to conditions $M_X^2 \ll W^2$ and $Q^2 \ll W^2$ mentioned before.

If mass M_Y of system Y is small and there is a rapidity separation between X and Y systems, these double dissociative (2.33) processes also exhibit diffractive nature. These proton dissociative processes are part of the measured cross section if the events are selected by means of large rapidity gap method.

2.3.4 Regge Phenomenology of Diffractive *ep* Scattering

As was already said also single dissociative diffractive processes can be described by the exchange of pomeron trajectory. According to the Regge theory, the $\gamma^* p$ cross section takes form [47]:

$$\frac{\mathrm{d}\sigma^{\gamma p}}{\mathrm{d}x_{IP}\mathrm{d}t} = f_{IP}(x_{IP}, t)\sigma_{\gamma^* IP}(M_X^2), \tag{2.40}$$

where f_{IP} is the pomeron flux factor depending only on the scattered proton kinematics:

$$f_{IP}(x_{IP}, t) = \frac{1}{16\pi^2}|g_{IP}(t)|^2 x_{IP}^{1-2\alpha_{IP}(t)} \tag{2.41}$$

and $\sigma_{\gamma^* IP}$ is the total cross section of $\gamma^* IP$ scattering with CMS energy M_X

$$\sigma_{\gamma^* IP}(M^2) = g_{3IP}(0) g_{IP}(0)(M_X^2)^{\alpha_{IP}(0)-1}. \tag{2.42}$$

The $g_{3IP}(0)$ is triple pomeron coupling and $g_{IP}(t)$ is pomeron coupling to the proton which typically has exponential behavior

$$g_{IP}(t) = g_{IP}(0)\mathrm{e}^{B_{IP}t/2}. \tag{2.43}$$

Note that since pomeron is not real particle this factorization is not unique and especially the pomeron flux normalization is ambiguous. Within the Regge picture, x_{IP} is interpreted as a momentum fraction of the pomeron with respect to the proton and $(-t)$ as the pomeron's virtuality.

Following equations (2.40-2.43), the Regge prediction for the differential cross section at $t = 0$ is proportional to

$$\left.\frac{\mathrm{d}\sigma^{\gamma p}}{\mathrm{d}x_{IP}\mathrm{d}t}\right|_{t=0} \sim (W^2)^{\alpha_{IP}(0)-1}\frac{1}{x_{IP}^{\alpha(0)}}, \tag{2.44}$$

so for $\gamma^* p$ scattering at high energy W and small x_{IP} the diffractive interactions mediated by pomeron dominate while for higher x_{IP} the sub-leading reggeon trajectory $\alpha_{IR}(0) \simeq 0.5$ plays a non-negligible role.

Substituting $g_{IP}(t)$ from formula (2.43), the pomeron and/or reggeon flux turns to its usual form

$$f_{IP,IR}(x_{IP}, t) = A_{IP,IR}\frac{\mathrm{e}^{B_{IP,IR}t}}{x_{IP}^{2\alpha_{IP,IR}(t)-1}}, \tag{2.45}$$

	IP	IR
$\alpha(0)$	1.12 ± 0.01	0.5 ± 0.1
$\alpha'[\mathrm{GeV}^{-2}]$	$0.06^{+0.19}_{-0.06}$	$0.3^{+0.6}_{-0.3}$
$B[\mathrm{GeV}^{-2}]$	$5.5^{+0.7}_{-2.0}$	$1.6^{+0.4}_{-1.6}$

Tab. 2.1: Parameters of pomeron (IP) and reggeon (IR) trajectories and the B factors of corresponding Regge poles as used and measured in [4].

where $A_{IP,IR}$ are normalization factors, $B_{IP,IR}$ relate to the t-slope of the cross section and trajectories $\alpha_{IP,IR}(t)$ are commonly set to have a linear form (2.27). Approximate values of these parameters are summarised in Tab. 2.1

2.3.5 Factorization in inclusive DIS

If the square root of photon virtuality Q is substantially larger than QCD scale Λ, Q^2 provides hard scale for process (2.35) and perturbative theory is applicable.

In perfect analogy with inclusive DIS (2.6), the diffractive DIS differential cross section can be written using two structure functions F_2^D and F_L^D which depend on four variables x, Q^2, x_{IP} and t:

$$\frac{\mathrm{d}\sigma_{ep}^D}{\mathrm{d}x\mathrm{d}Q^2\mathrm{d}x_{IP}\mathrm{d}t} = \frac{4\pi\alpha_{em}^2}{xQ^4}\left[\left(1 - y + \frac{y^2}{2}\right)F_2^D(x, Q^2, x_{IP}, t) - \frac{1}{2}y^2 F_L^D(x, Q^2, x_{IP}, t)\right]. \tag{2.46}$$

Similarly to non-diffractive case, the longitudinal structure function F_L^D is much smaller than F_2^D for $\beta < 0.8$ and can be therefore safely neglected in this range.

It has been proven by Collins [1] in perturbative QCD that similarly to what happens in inclusive DIS, the factorization theorem holds for diffractive structure function, if the hard scale $Q^2 \gg \Lambda^2$:

$$F_2^D(x, Q^2, x_{IP}, t) = \sum_{i=q,\bar{q},g} \int_x^{x_{IP}} \mathrm{d}\xi f_i^D(\xi, \mu_f^2, x_{IP}, t)\hat{F}_2^i\left(\frac{x}{\xi}, Q^2, \mu_f^2, \mu_r^2\right), \tag{2.47}$$

where the coefficient functions $\hat{F}_2^i$ calculable within p-QCD are exactly the same as in DIS and $f_i^D(\xi, \mu_f, x_{IP}, t)$ are the diffractive parton distribution functions (DPDF) which describe the probability to find a parton of type i carrying momentum fraction ξ in proton, under the requirement that the proton remains intact and its kinematics is described by x_{IP} and t. These DPDFs obey the same QCD DGLAP evolution equation as non-diffractive parton densities (2.24) and were extracted from DGLAP fits of reduced cross sections $\sigma_r^D \simeq F_2^D$ of HERA inclusive diffractive data.

Within Regge theory, these diffractive proton densities can be viewed as a pomeron PDFs multiplied by the pomeron flux factor, i.e. probability to find pomeron inside

the proton. Resulting factorization formula is analogous to (2.40) and takes form

$$f_i^D(x, Q^2, x_{IP}, t) = f_{IP}(x_{IP}, t) f_{i/IP}(\beta = x/x_{IP}, Q^2) \tag{2.48}$$

where β has interpretation as momentum fraction of the struck parton with respect to the pomeron and the pomeron flux f_{IP} is usually parametrized by formula (2.45).

The pomeron PDF was at the stating scale Q_0^2 of the QCD evolution in [4] parametrized as $\beta f_{q/IP}(\beta, Q_0^2) = A_q \beta^{B_q}(1-\beta)^{C_q}$ and $\beta f_{g/IP}(\beta, Q_0^2) = A_g \beta^{B_g}(1-\beta)^{C_g}$, where the identical distribution functions were assumed for all considered quarks distributions (=u, d, s, $\bar{u}$, $\bar{d}$ and $\bar{s}$). This form of pomeron parametrization is physically motivated by its vacuum nature, especially by its zero electric charge and zero isospin.

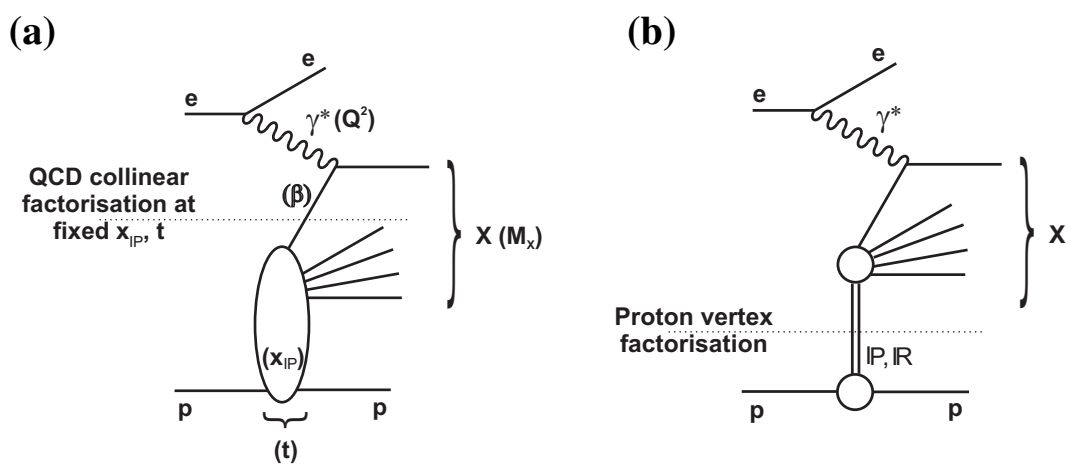

Fig. 2.12: The leading order Feynman diagrams of diffractive DIS interactions $ep \to eXp$. The hard subprocess is $\gamma^* q \to q'$. The dotted lines show the place where the diagram can be divided under the assumption of QCD collinear factorization (a) and proton vertex factorization. Pomeron and sub-leading reggeon exchanges are represented by the double line.

The DPDFs parametrization form described above was used and it's validity successfully experimentally tested at HERA. For higher values of $x_{IP} > 0.02$, the sub-leading reggeon trajectory has to be included to describe the data.

Both types of factorization are shown in Fig. 2.12. It must be stressed, that the QCD collinear factorization was proved within p-QCD and is therefore much more fundamental compared to the proton vertex factorization resulting from Regge theory. Origin of the Regge theory is linked to non-relativistic quantum mechanics, where it stands on a firm ground, while the high-energy extension relies on a series of assumptions. Within the procedure of the DPDFs fitting, the proton vertex factorization is utilized just as successful guess of the DPDFs parametrization on the starting scale

of the QCD evolution and does not necessary represent any deeper physical principle, similarly to the initial pomeron parametrization at the starting scale.

2.3.6 Diffractive Dijet Production in *ep* Scattering

The diffractive parton densities extracted from inclusive DDIS can be used to predict cross section of others, less inclusive processes. One of such processes is high-p_T dijet production

$$e + p \to e + p + jj + X', \tag{2.49}$$

where system X' is the hadronic final state system X excluding the two jets.

For diffractive dijet production two additional invariants are introduced. Denoting u and v the four-momenta entering to the hard subprocess from photon and pomeron side, respectively, x_γ (z_{IP}) is the longitudinal fraction of photon (pomeron) momentum entering to the hard subprocess (Fig. 2.13). Exact definitions of these variables take form:

$$z_{IP} = \frac{qv}{q(P - P')} \qquad x_\gamma = \frac{Pu}{Pq}. \tag{2.50}$$

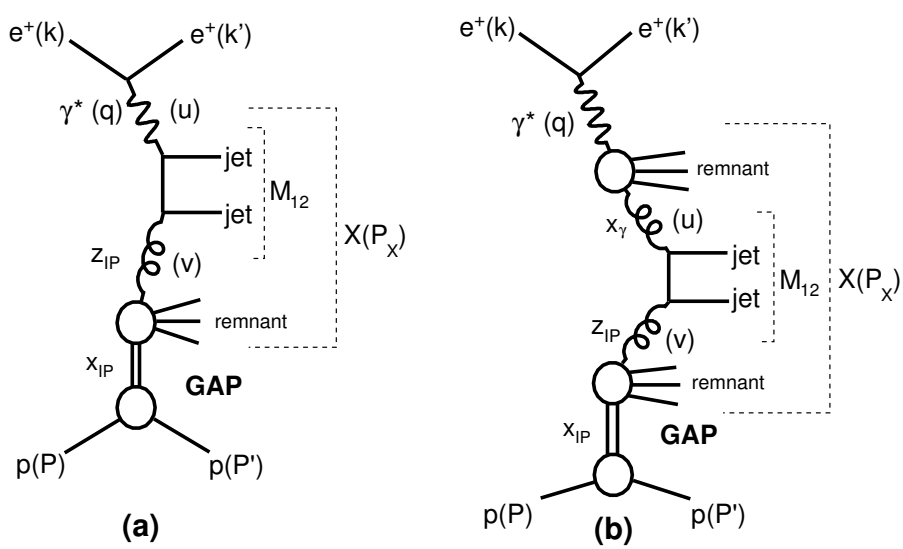

Fig. 2.13: The leading order Feynman diagram for the direct (left) and resolved (right) diffractive dijet production. In direct production four-momenta u and q are identical.

To be stressed, for the dijet production the invariant x no longer plays the role of the momentum's fraction of parton entering to the hard subprocess. Repeating

procedure of (2.8) and denoting this fraction as $\tilde{x}$ leads to:

$$(P\tilde{x}+q)^2 = M_{12}^2 \quad \rightarrow \quad \tilde{x} = \frac{M_{12}^2+Q^2}{2Pq} = \frac{M_{12}^2+Q^2}{W^2}, \tag{2.51}$$

where the proton mass squared as well as Q^2 were neglected with respect to the W^2. Due to the M_{12} term really $\tilde{x} \neq x$. It can be shown, that relation analogical to (2.38) takes for dijet production form:

$$z_{IP} = \frac{\tilde{x}}{x_{IP}}, \tag{2.52}$$

where x_{IP} ($\tilde{x}$) is momentum fraction of the pomeron (interacting parton) with respect to the proton and z_{IP} momentum fraction of the interacting parton with respect to the pomeron.

Two regimes of the diffractive dijet production exist in the leading order picture (Fig. 2.13). For direct processes, which dominate in high Q^2 region, photon enters directly into the hard subprocess and variable x_γ is identically equal to 1. On the other hand, if the photon virtuality Q^2 is small, instead of photon, long living partonic fluctuations $\gamma \rightarrow q\bar{q}$ can interact with partons in proton (resolved processes). These hadronic fluctuations exhibit non-perturbative nature, therefore photon parton distribution function (γ-PDF) is employed to describe the structure of resolved photon. This γ-PDF $f_{j/\gamma}(x_\gamma, \mu_f^2)$ represents the probability of finding parton j inside of real photon when photon is probed on scale μ_f^2. Photon parton densities were extracted from events of type $e^+e^- \rightarrow e^+e^-\gamma^*\gamma \rightarrow e^+e^- +$ hadrons, which were studied at LEP [48]. In these events, the hadronic structure of real photon γ is probed by short wavelength virtual photon γ^*. In this thesis GRV [49] and AFG [50] as an alternative NLO γ-PDF will be used for theoretical calculations.

Employing QCD collinear factorization theorem for diffractive processes, the cross section of direct processes is given by the convolution of partonic cross sections $\mathrm{d}\hat{\sigma}$ with diffractive parton distributions $f_{i/p}^D$ [8]:

$$\begin{aligned} \mathrm{d}\sigma(ep \rightarrow e + 2\,\mathrm{jets} + X' + p) = \sum_i \int \mathrm{d}t \int \mathrm{d}x_{IP} \int \mathrm{d}z_{IP} \\ \mathrm{d}\hat{\sigma}_{ei\rightarrow 2\,\mathrm{jets}}(\hat{s}, \mu_R^2, \mu_F^2) \otimes f_{i/p}^D(z_{IP}, \mu_F^2, x_{IP}, t). \end{aligned} \tag{2.53}$$

Here the integrals extend over accepted phase space and the sum runs over all partons i contributing to the cross section. Subprocess invariant energy squared is labeled as $\hat{s} \sim x_{IP} z_{IP} ys - Q^2$ and μ_f^2 and μ_r^2 represent factorization and renormalization scales. In the DIS region ($Q^2 \gg \Lambda^2$) is the direct process (2.53) the only relevant contribution to the cross section.

[8] In contrast to the f_i^D defined by relation (2.47), the first argument of $f_{i/p}^D$ is here momentum of parton entering to the hard subprocess with respect to the pomeron, instead of the proton.

In the photoproduction regime ($Q^2 \lesssim \Lambda^2$) also the resolved interactions contribute, the cross section for these processes (Fig. 2.13b) is given by

$$\mathrm{d}\sigma(ep \to e + 2\,\mathrm{jets} + X' + p) = \sum_{i,j} \int \mathrm{d}t \int \mathrm{d}x_{IP} \int \mathrm{d}z_{IP}$$

$$\int \mathrm{d}y\; f_{\gamma/e}(y) \int \mathrm{d}x_\gamma\; f_{j/\gamma}(x_\gamma, \mu_F^2) \times \mathrm{d}\hat{\sigma}_{ij\to 2\,\mathrm{jets}}(\hat{s}, \mu_R^2, \mu_F^2) \otimes f^D_{i/p}(z_{IP}, \mu_F^2, x_{IP}, t), \quad (2.54)$$

where $f_{\gamma/e}$ is the Weizäcker-Williams equivalent photon flux [51, 52] integrated over the measured Q^2 range and $f_{j/\gamma}$ is the photon PDF. In this case, the CMS energy squared of the hard subprocess is approximately $\hat{s} \sim x_\gamma x_{IP} z_{IP} y s$.

The equivalent photon flux approximation can be safely used in the photoproduction regime, where Q^2 is small and emitted photon is nearly collinear to the incoming electron. The flux factor is then given by

$$f_{\gamma/e}(y) = \frac{\alpha_{em}}{2\pi} \left[\frac{1 + (1-y)^2}{y} \ln \frac{Q^2_{max}}{Q^2_{min}} - 2m_e^2 y \left(\frac{1}{Q^2_{min}} - \frac{1}{Q^2_{max}} \right) \right], \quad (2.55)$$

where Q^2_{min} is the lowest kinematically allowed value, $Q^2_{min} = \frac{m_e^2 y^2}{1-y}$ and Q^2_{max} is determined by the measurement setup.

2.3.7 Factorization Breaking in Diffraction

In 1997 the QCD collinear factorization theorem was proven for diffractive dijet production in the DIS region within perturbative QCD by Collins [1]. On the other hand, there were theoretical indications [13, 53] that the factorization theorem is being broken in diffractive hadron-hadron interactions and diffractive photoproduction as well.

The factorization breaking was firstly experimentally observed at Tevatron [10]. The measured cross section was suppressed by around one order of magnitude compared to the theoretical predictions based on HERA DPDFs and QCD collinear theorem.

Factorization breaking can be explained as a consequence of the additional soft rescattering which populates the rapidity gap by secondary particles and destroys the leading proton. Within the simple one-channel eikonal model, the gap survival probability S^2, which describes the suppression of the cross section with respect to the predictions based on QCD collinear model is [54]

$$S^2 = \frac{\int |M(s,b)|^2 P^S(s,b)\, \mathrm{d}^2 b}{\int |M(s,b)|^2\, \mathrm{d}^2 b}, \quad (2.56)$$

where the integration is done in the impact parameter space. The $P^S(s,b)$ is the probability that no inelastic soft interaction results in inelasticity of the final state

(s, b) and is calculated by means of opacity Ω as $P^S = \mathrm{e}^{-\Omega(s,b)}$, where the opacity is Gaussian-distributed:

$$\Omega(s, b) = \nu(s) \frac{1}{\pi R^2(s)} \mathrm{e}^{-\frac{b^2}{R^2(s)}}. \tag{2.57}$$

Functions $\nu(s)$ and $R^2(s)$ are obtained from the fits of the total, elastic, and inelastic hadron-hadron cross sections. The matrix element in the impact parameter space $M(s, b)$ is process dependent [55], especially for single-dissociative diffractive pp interaction takes form:

$$|M|^2 \sim \exp\left(-\frac{b^2}{3 \cdot 2B}\right), \tag{2.58}$$

where $2B \sim 5\,\mathrm{GeV}^{-2}$ is the slope of the diffractive inclusive cross section. This model describes reasonably well the suppression factor of diffractive hadron-hadron cross section.

Naively, the resolved photon interactions in the diffractive γp scattering resemble diffractive pp collisions, because two objects with partonic structure interact, whereas the direct photon interaction are expected to be unsuppressed. However, the hadronic nature of photon and proton differs. The photon parton densities can be divided into the hadron-like and the point-like contribution. The later is arising from the inhomogeneous term (corresponding to splitting $\gamma \to q\bar{q}$) in the QCD evolution equations for the photon [14] and exhibits perturbative nature. The size of such $q\bar{q}$ dipole representing the point-like contribution is smaller and therefore is expected to generate smaller absorptive corrections compared to the hadron-like part [15]. The suppression factor predicted for the "point-like" photon slightly depends on the jet transverse energies E_T and equals about $0.7 - 0.8$ for the phase space of the HERA measurements [15].

The cross section originating from the hadron-like photon contribution is expected to be suppressed by factor of ~ 0.34 [12], which is similar value to the suppression of diffractive pp interactions at the HERA CMS energies. The hadron-like part occurs only at lowest values of photon four-momentum fractions $x_\gamma \sim 0.1$ which are experimentally hardly accessible at HERA and, therefore, represents only small fraction of the cross section.

Unfortunately, the situation is even more complex due to ambiguity in the cross section division to the direct and resolved photon interactions at the next-to-leading order. This division in example depends on the factorization scheme of the γ-PDF, hence only the sum of both photon components is physically meaningful. In addition, direct $x_\gamma = 1$ interactions are smeared by the hadronization and detector resolution towards lower x_γ values, which prevents from unequivocal identification of such interactions in the measurement.

2.3.8 Experimental Signature of Diffractive Events

There are three techniques to select diffractive events, large rapidity gap method (LRG), M_X-subtraction method and forward proton detection. Discussion is focused on diffractive $\gamma^* p \to XY$ processes, with leading system Y in beam proton direction, but is mostly valid also for hadron-hadron diffractive processes.

M_X-Subtraction method

Approximative Regge theory prediction (2.44) for the cross section differential in $\ln M_X^2$

$$M_X^2 \frac{\mathrm{d}\sigma}{\mathrm{d}M_X^2} = \frac{\mathrm{d}\sigma}{\mathrm{d}\ln M_X^2} \sim \frac{1}{(M_X^2)^{\alpha(0)-1}} \sim \exp((1-\alpha(0))\ln M_X^2) \tag{2.59}$$

shows that in case of diffractive events ($\alpha(0) \simeq 1$) the distribution is nearly constant whereas decreases exponentially for small $\ln M_X^2$ in case of non-pomeron trajectories ($\alpha(0) \lesssim 0.5$).

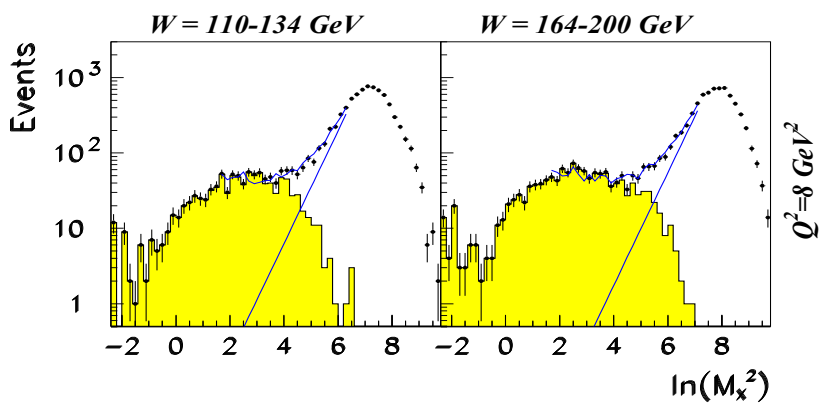

Fig. 2.14: The events rates of reaction $ep \to eX + anything$, where X is the system observed in the detector [56], as a function of $\ln M_X^2$. The yellow histogram shows the distribution of events with the additional requirement of no hadronic activity in the forward region above pseudorapidity 1.5 ($\eta_{max} < 1.5$). The straight lines give the nondiffractive contribution as obtained from the fits.

It allows to subtract exponentially suppressed non-diffractive background in small-M_X region. This method was used only by ZEUS collaboration [56] (Fig. 2.14) and was abandoned in newer papers due to substantial model dependent proton dissociative background of system Y.

Large Rapidity Gap Method

Another selection technique follows from approximate relation for size Δy of the rapidity gap:

$$\Delta y \simeq \ln \frac{1}{x_{IP}} \simeq \ln \frac{W^2}{M_X^2}, \tag{2.60}$$

where W is centre-of-mass energy of the diffractive collision. Assuming constant W, the relation (2.59) turns to

$$\frac{\mathrm{d}\sigma}{\mathrm{d}\Delta y} \sim \exp(-(1-\alpha(0))\Delta y), \tag{2.61}$$

therefore the rapidity gap size is exponentially suppressed for non-diffractive events ($\alpha(0) \lesssim 0.5$) whilst diffractive events ($\alpha(0) \simeq 1$) exhibit constant $\frac{\mathrm{d}\sigma}{\mathrm{d}\Delta y}$ behavior.

In the typical inclusive DIS event, the rapidity interval between the proton remnant and the struck quark is filled by hadronic activity, which is a consequence of the color connection between these objects. Relation (2.61) can be interpreted as a Poisson distribution, if $(1-\alpha(0))$ is the mean number of hadronic emissions per the unit of rapidity. For the diffractive interactions mediated by the color singlet pomeron no such color reconnection exists, resulting in no hadronic activity between the diffractive systems. The event pictures of typical non-diffractive and diffractive events are presented in Fig. 2.15. Note that in the depict diffractive event the leading proton left detector undetected.

The rapidity of the forward proton reaches at HERA maximally $y_{\max} = 7.6$. Within experimental setup, rapidity is normally substituted to pseudorapidity η, which depends only on the scattered angle and condition on no hadronic activity within certain pseudorapidity interval is imposed. In contrast to rapidity, the pseudorapidity η has no upper bound. For illustration, the mean η value for HERA diffractive events is about 9, averaged over scattered proton angles and neglecting scattered proton energy loss ($x_{IP} = 0$). Efficient LRG selection requires good pseudorapidity coverage of the forward region by the detectors. H1 experiment is equipped by forward detectors with coverage up to $\eta \sim 7.5$, which allows to require no hadronic activity between $\eta = 3.2$ and $\eta = 7.5$ yielding to rapidity gap size $\Delta\eta = 4.3$. Such experimental condition efficiently suppresses non-diffractive and proton dissociative background and allows to measure higher M_X-mass diffractive states, inaccessible by the M_X-subtraction method. More specifically, events with p_T of diffractive systems Y above 1 GeV and masses above 1.6 GeV, i.e. $M_Y > 1.6$ GeV, can be excluded by such selection.

In the proton dissociative event, system Y consists usually of N^* resonance, decaying primarily to nucleon and pion. To demonstrate, how can be such resonance detected, let's consider Y system being $N^*(1680)$, which is slightly above H1 acceptance limit $M_Y = 1.6$ GeV. Assuming isotropic angular distribution of N^* decays, the

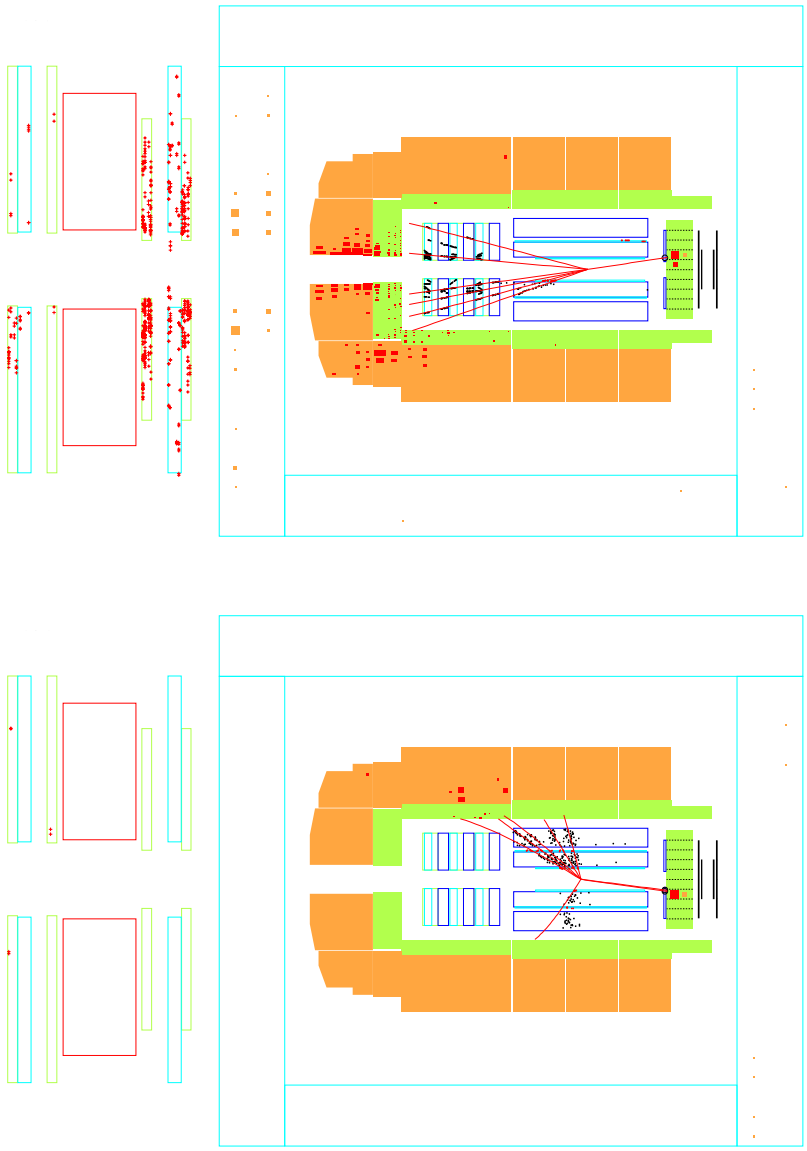

Fig. 2.15: A "standard" DIS event (top) compared to event with the large rapidity gap (bottom), i.e. no activity in the forward region of the detector (=on the left), as seen by H1 detector at HERA.

pion's p_T would be around 0.4 GeV and energy $\sim$120 GeV. Resulting pion's pseudorapidity $\eta \simeq 6.4$ indicates that this dissociative state could be vetoed by H1 forward detectors.

Leading Proton Detection

In principle, the cleanest way to select the diffractive events is to detect the leading proton (the most energetic proton in the final state). The spectrum of the momentum fraction of the leading protons with respect to the incoming proton x_L is shown in Fig. 2.16[9]. The diffractive peak $x_L \simeq 1$ is dominated by the pomeron exchange (dashed line) while at values $x_L \lesssim 0.95$ the reggeon exchange, the proton dissociation and the inclusive DIS events play a role which makes here the distinction between diffractive and non-diffractive events rather difficult [47].

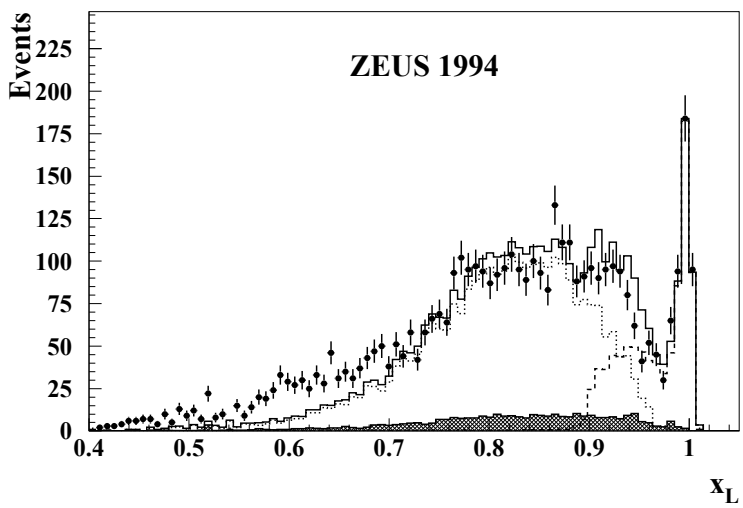

Fig. 2.16: The observed spectrum of the leading proton fractional momentum $x_L = 1-x_{IP}$ as measured by ZEUS collaboration by the Leading Proton Spectrometer (LPS) [57]. The diffractive signal modeled by MC Rapgap is represented by the dashed line. The pion exchange contribution is denoted by the dotted line and the shaded area corresponds to the proton dissociation. Note that the distribution is not corrected for the detector acceptance, especially acceptance falls by almost an order of magnitude between $x_L \simeq 1$ and $x_L \simeq 0.8$.

The leading diffractive protons tend to have small transverse momenta and $x_L \simeq 1$, therefore they stay very close to the nominal beam which makes their detection

[9]Note that due to the momentum conservation law, there cannot be any other, more energetic particle if any with $x_L \gtrsim 0.5$ is detected.

challenging. There are two ways (not clearly separated) how to measure the diffractive protons of $x_L \sim 0.98$.

The first possibility is to detect only protons with non-zero transverse momenta (=angular deflection), at HERA typically $p_T \gtrsim 0.1$GeV which results in deviation ~ 1 cm with respect to the beam line at distance of 80 m from the interaction point. This principle was used by the H1 Forward Proton Spectrometer (FPS) [2] with two stations 61 and 80 meters away from the interaction point and by the ZEUS Leading Proton Spectrometer (LPS) [58] which consists of six stations located between $z = 20$ m and $z = 80$ m. Acceptance of this method is for $x_L \sim 0.98$ quite limited because the transverse momenta distribution of the scattered protons decrease exponentially.

The another possibility is to fully utilize the spectroscopic effect which causes that the trajectories of protons with smaller energies tend to be more curved due to the magnetic field of HERA collider. Hence the less energetic protons are well separated from the nominal beam and therefore measurable. This idea was used by the H1 Very Forward Proton Spectrometer (VFPS) [3] which consists of two stations situated 218 m and 222 m away from the interaction point. Such higher distance makes the spectroscopic effect dominant. This approach allows to measure protons without any angular deflection which results in better acceptance in discussed x_L region. On the other hand protons with lower energies of about $x_L \sim 0.9$ are absorbed by the material around the beam before they reach the detector.

These two approaches are nicely demonstrated in Fig. 3.8, which shows that the FPS hit position dominantly depends on the leading proton angle while the VFPS hit position on its energy.

2.4 Monte Carlo Generators

Monte Carlo (MC) generators became an essential tool in high energy physics which provide either the theoretical predictions of the measured cross section or are used to correct the measured data for the detector effects. Based on the random number generator, MC can generate unweighted[10] real-like events, i.e. events with stable particles and "real-world" event rates.

Parton Level

Monte Carlo generator Rapgap [59] usable in both diffractive and non-diffractive *ep* scattering is based on leading order partonic QCD cross section of simulated subprocess. Rapgap manages to simulate both direct and resolved diffractive dijet production in the LO α_s accuracy. Relevant higher order contributions are mimicked using

[10] Event weights are sometimes utilized to reduce amount of the uninteresting typically low p_T soft events in the generated MC sample.

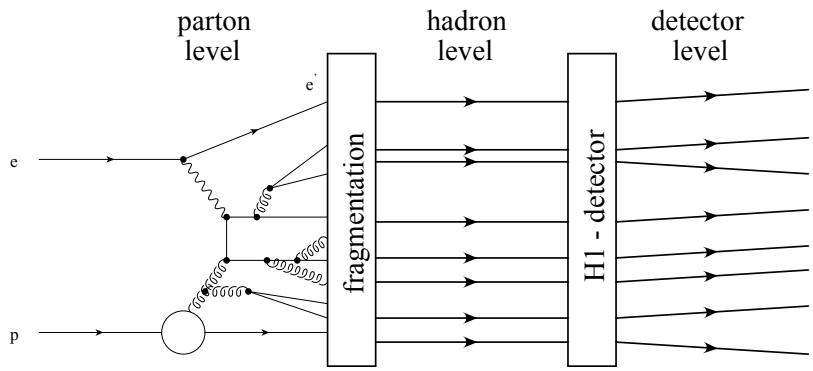

Fig. 2.17: Schematic explanation of the parton, hadron and detector level event stage.

initial and final state leading logarithm parton showers. These parton showers are usually rather successful in describing event shape, but the overall cross section normalization may be wrong due to the absence of true higher order matrix elements of the partonic subprocess. The stage of the simulation, where event contains scattered lepton and partons originating from the hard subprocess, parton showers and the proton (pomeron) remnant is known as a *parton level* (Fig. 2.17).

Hadron Level

In the next phase of the simulation partons from hard subprocess, parton showers and beam (pomeron) remnant enter to the hadronization algorithm which produces colorless hadrons. These phenomenological models of hadronization are very sensitive to the color topology of the event which is described by so-called color lines within partons, employing the $N_c \to \infty$ picture [60]. In Rapgap the hadronization is implemented by means of the Lund string model which is also used by the Pythia MC generator [61]. An alternative model of hadronization, the so-called cluster model is used in Herwig [62] and in corresponding diffractive version Pomwig [63]. Effects of the QED initial and final state radiation, as well as virtual corrections, are simulated using HERACLES [64] interfaced with Rapgap. Event stage of final state stable hadrons is known as the *hadron level*.

Detector Level

For completeness, the *detector level* of the event includes in addition simulation of the detector acceptance, resolution, and detector inefficiencies. These detector effects are commonly simulated using GEANT program [65] which models passage of particles through the matter (detector's layers) and response of the detector's electronics.

2.5 NLO QCD Predictions

For the diffractive dijet cross section, the next-to-leading contribution in α_s to the total cross section is by no means negligible and needs to be evaluated using special programs. These programs manage to calculate two jets NLO QCD cross section at the parton level.

Here the program of Frixione at al. [66] was used for photoproduction and NLOJET++ [67] for DIS. Both programs were adapted for hard diffraction based on the Resolved Pomeron Model [68]. The ep scattering is effectively replaced by the eIP scattering, where the pomeron beam energy is downscaled with respect to the nominal proton beam energy by a factor of x_{IP}. The calculations are performed in the central values of the x_{IP} intervals $(x_{IP} - \Delta x_{IP}/2,\ x_{IP} + \Delta x_{IP}/2)$ and the resulting ep cross section corresponds to the sum of these intermediate results where the Δx_{IP} is sufficiently small to mimic continuous distribution. For the resolved photoproduction a similar approach is applied also from the electron side, i.e. effectively the γIP interactions are evaluated.

The NLO calculations are performed with the number of flavors fixed to 5 and QCD scale parameter set to $\Lambda_5 = 0.228\,\mathrm{GeV}$, corresponding to a 2-loop $\alpha_s(M_Z)$ equals to 0.118. The renormalization and factorization scales are set to be equal and are calculated from the leading jet and sub-leading jet transverse energy in the $\gamma^* p$ frame[11] and the momentum transfer Q^2 as[12]:

$$\mu_R = \mu_F = \sqrt{\langle E_T^{*\mathrm{jets}} \rangle^2 + Q^2}. \tag{2.62}$$

Note that for photoproduction, Q^2 is taken as zero. The sensitivity of the calculated cross section on the scale choice is studied by varying both scales simultaneously by a factor of two up and down. The NLO calculations for photoproduction were verified with an alternative NLO QCD program of Klasen and Kramer [69, 70]. Similarly, the NLOJET++ predictions were checked with DISENT NLO [71].

2.6 Jet algorithm

Parton dynamics of the hard process is smeared by parton showering, hadronization, and detector resolution. Jet algorithm is a procedure of clustering close objects into jets, which properties resemble original final-state partons of the hard subprocess. Furthermore, jet algorithm rescues p-QCD cross section from singularities stemming

[11] In the $\gamma^* p$ rest frame conventionally incoming proton momentum is pointing towards positive z'-axis and azimuthal angle ϕ' of the scattered electron is zero.

[12] The variable $\langle E_T^{*\mathrm{jets}} \rangle$ denotes the mean transverse energy of the dijet system in the $\gamma^* p$ frame, $\langle E_T^{*\mathrm{jets}} \rangle = \frac{1}{2}\left(E_T^{*\mathrm{jet1}} + E_T^{*\mathrm{jet2}}\right)$

from emissions of collinear and soft partons, because the ambivalence in the final state is removed by merging these objects into single jet.

In this thesis, the inclusive k_T jet algorithm [72] applied in the $\gamma^* p$ rest frame is used. It fulfils all necessary features like infrared and collinear safety, z'-boost invariance, good correspondence of jet's dynamics between different levels (parton, hadron and detector) and small dependence on the hadronization model. Roughly saying this algorithm merges sequentially pairs of objects which have small distance in the (η, ϕ) plane together. This distance is weighted by the minimum P_T of this pair, causing that the soft emissions are merged preferentially.

Inclusive k_T algorithm works with proto-jets which are identified, depending on the event-level, with the final state particles, partons or calorimeter energy clusters in the beginning. The workflow of the k_T algorithm is the following:

1. Define distances D_i and D_{ij} for each proto-jet and each proto-jet pair:

$$D_{ij} = \min\left(P_{Ti}^2, P_{Tj}^2\right)\frac{(\eta_j - \eta_i)^2 + (\phi_j - \phi_i)^2}{R^2} \qquad D_i = P_{Ti}^2 \tag{2.63}$$

2. Find the smallest value of D_i and D_{ij} distances.

   - If this value is D_{kl} then merge proto-jets k and l into proto-jet m.

$$P_{T,m} = P_{T,k} + P_{T,l} \tag{2.64}$$

$$\eta_m = \frac{P_{T,k}\eta_k + P_{T,l}\eta_l}{P_{T,m}} \tag{2.65}$$

$$\phi_m = \frac{P_{T,k}\phi_k + P_{T,l}\phi_l}{P_{T,m}} \tag{2.66}$$

   - If the smallest value is D_k then the corresponding proto-jet k turns into the jet and is removed from the proto-jet list.

3. Go to step 1 until any proto-jet remains.

In the algorithm description η denotes pseudorapidity, ϕ azimuthal angle and P_T transverse momentum of the proto-jet in the $\gamma^* p$-frame.

The anti-k_T algorithm [73], widely used at LHC, gives at HERA comparable results as was studied in [74]. The only difference between k_T and anti-k_T algorithm consists in distance formulas (2.63), where the anti-k_T algorithm is obtained by substituting $P_T^2 \to P_T^{-2}$. Consequently, the anti-k_T algorithm recombines first the hardest particles (typically in the jet centre) in contrast to the k_T-algorithm.

Chapter 3

Experimental Setup

3.1 The HERA Collider

The HERA (Hadron-Elektron-Ring-Anlage) was ring particle accelerator located at the DESY[1] facility in Hamburg. At HERA, electrons were collided with protons at a CMS energy up to 319 GeV, which represents the highest achieved energy of ep interactions.

High collisions energies were allowed due to a series of smaller preaccelerators which injected protons of 40 GeV and 14 GeV electrons into the main HERA ring. The HERA tunnel (Fig. 3.1) has a circumference of 6.3 km and is located around 15 to 30 m underground. During the operation, the circulating electrons were bended by the conventional 0.17 T dipole magnets while protons required superconducting coils with strength 4.5 T [2].

In HERA-I operation phase (1992-2000) the p and e beam energies were 820 GeV and 27.5 GeV and the integrated luminosity of 130 pb^{-1} was achieved. After the high-luminosity upgrade (HERA-II phase in years 2004-2007) additional data of luminosity about 360 pb^{-1} were collected, with corresponding energies of protons and electrons of 920 GeV and 27.6 GeV, respectively. The last phase of HERA-II operation with reduced proton beam energies of 460 and 575 GeV enabled the direct measurement of longitudinal proton structure function (Fig. 3.2). In reality, not only electrons, but both electrons and positrons beams were employed (Fig. 3.2), which allowed for detailed study of the parity violating electroweak interactions.

Two multi-purpose experiments were located at HERA, H1 and ZEUS, in addition, there were fixed target experiments HERA-B and HERMES to study CP violations in the B-meson system and electron-nucleon scattering, respectively. The measured ep interactions are due to the different e and p beam energies highly asymmetric and both

[1] Deutsches Elektronen Synchrotron

[2] Note that charged particle trajectory curvature is proportional to B/p.

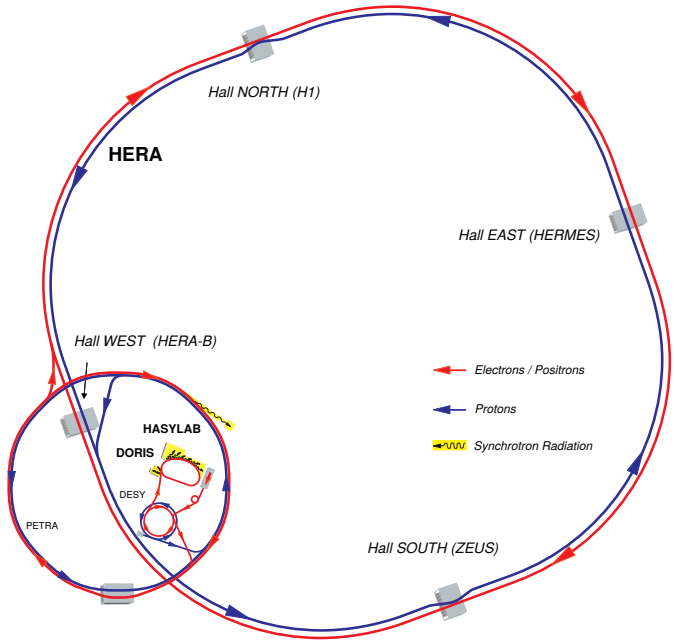

Fig. 3.1: The HERA collider.

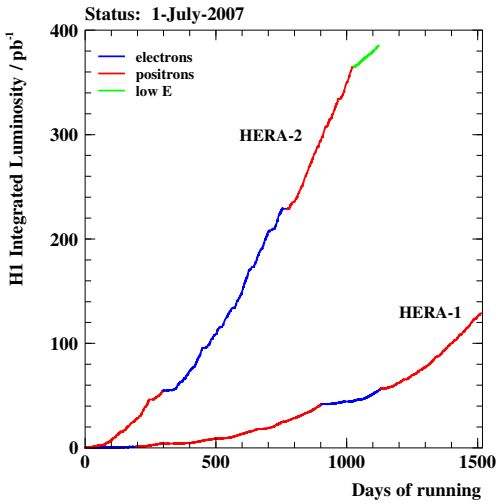

Fig. 3.2: The H1 integrated luminosity as a function of time for HERA-I and HERA-II phase.

general purpose detectors must reflect this property, especially most energy deposit is in the forward region[3] of the detectors (pseudorapidities $\sim$1.8).

The HERA beam survived typically for 12 hours (so-called Fill), at the end of Fill the actual luminosity decreased by about 60%. Fill is split into several Runs, where detector and trigger setup during each run is by definition stable. Time interval of 96 ns between collisions corresponds to 220 bunches in the accelerator. Effectively only $\sim$180 bunches are used for physical analyses, the others are important i.e. for beam condition monitoring.

The peak luminosity of the HERA operation was $50\,\mu\mathrm{b}^{-1}/\mathrm{s}$ which corresponds to about twenty interactions per hour for 100 pb process, the typical value of the diffractive dijet cross sections discussed in this thesis.

3.2 The H1 Detector

The H1 was multi-purpose 2800 tones weighted detector with classical onion-like design of the detector's components (Fig. 3.3).

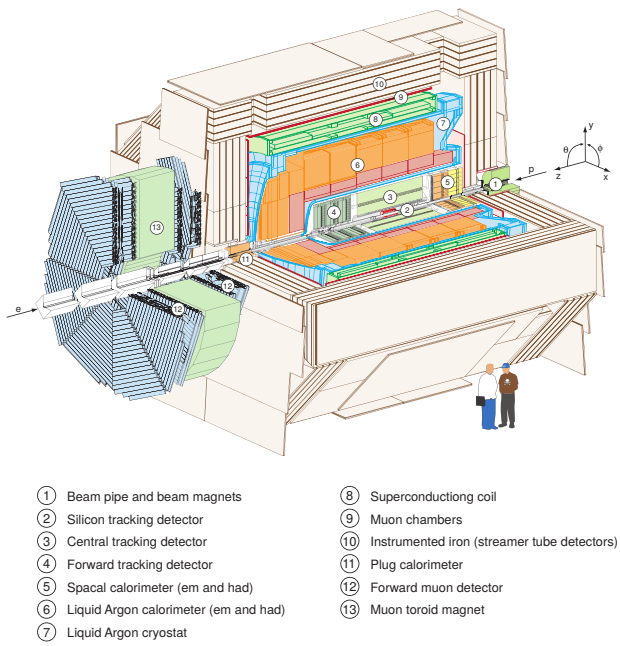

Fig. 3.3: Schematic drawing of the H1 detector. See the graphical explanation of H1 coordinate system on the right side of the figure, especially angles θ and ϕ.

[3] A right-handed coordinate system is employed with the origin at the nominal ep interaction point and with the positive z-axis pointing to the proton beam direction (the incoming proton's momentum). The x-axis is pointing in the horizontal direction to the center of the HERA ring.

The interaction point is surrounded by the Central Tracking Detector (CTD) supplemented by silicon detectors located inside drift chambers, Forward Tracking Detector (FTD) and Backward Proportional Chambers (BPC). Here the charged particle trajectories are bent by solenoidal homogeneous magnetic field of 1.16 T. Calorimetry system consists of Liquid Argon calorimeter (LAr) and SpaCal calorimeter in the backward direction for precise scattered electron measurement. In the outer part of H1 are muon detectors.

Detailed description of this experimental facility can be found elsewhere [75–77].

3.2.1 Tracking System

Due to large asymmetry of HERA *ep* collision the H1 tracking system is divided according to the polar angle into central (CTD) $15° < \theta < 165°$ and forward tracking system (FTD) $7° < \theta < 25°$[4]. Whole tracking system is situated inside 1.16 T solenoidal magnetic field created by a superconducting coil.

The CTD reconstruction is based on two large concentric drift chambers CJC1 and CJC2 (Fig. 3.4) where wires are strung parallel to the beam axes. This configuration allows track measurement with $r - \phi$ resolution of 170 μm and around 22 mm in the z-coordinate. To improve z-reconstruction two thin drift chambers CIZ and COZ are employed. These chambers have sense wire perpendicular to the beam axis which leads to 300 μm resolution in the z-coordinate. The resulting transverse momentum resolution is $\Delta p_T/p_T = 0.2\% \times p_T/\mathrm{GeV} \oplus 1.5\%$.

Fast multi-wire proportional chambers CIP and COP are used for triggering.

Closest to the interaction point (6 cm and 10 cm away from the beam pipe) are the silicon trackers (FST, CST, BST) which are mainly used for secondary vertex measurement important for heavy quark identification and also for triggering.

The Forward Track Detector (FTD) extends CTD coverage and consists of several drift chambers of different wire geometries. Its typical resolution in the $r - \phi$ plane is 210 μm.

3.2.2 Calorimetry

Liquid Argon Calorimeter

The non-compensation high-granularity Liquid Argon calorimeter (LAr) covers the polar range $4° < \theta < 154°$ (Fig. 3.5).

High spatial resolution is ensured by 45000 calorimeter's cells filled by 90 K liquid argon as an active medium. This sampling calorimeter uses 2.4 mm thick lead plates as absorber in the electromagnetic part and stainless steel plates of 16 mm thickness in the hadronic part.

[4]The Backward Proportional Chambers (BPC) are not used in presented measurement.

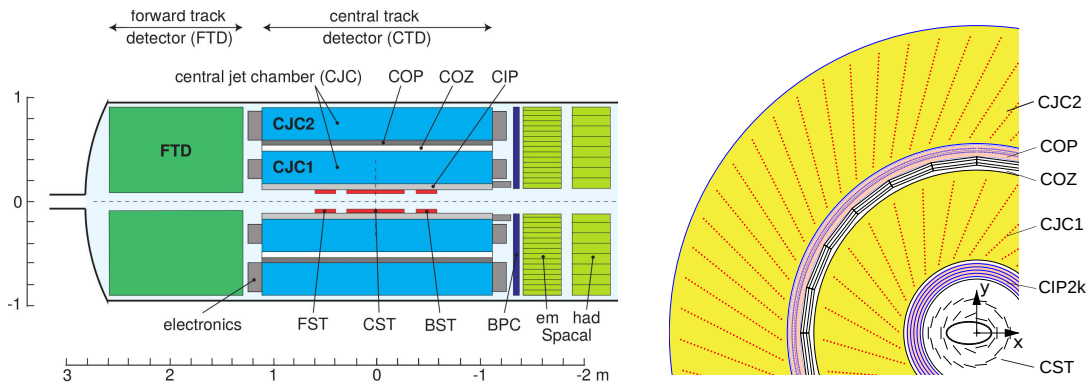

Fig. 3.4: Schematic view of H1 tracking system.

The inner electromagnetic part is 20-30 radiation length thick whereas the size of hadronic part is 5-8 interaction lengths, both numbers depend on angle θ.

The calorimeter response to the hadron induced shower is about 30% smaller than to the electromagnetic shower. Therefore, the resulting energy of the hadronic showers must be obtained by the off-line software reconstruction.

The calorimeter resolution measured in the test beams is $11\%/\sqrt{E/\mathrm{GeV}} \oplus 1\%$ for electromagnetic showers and $50\%/\sqrt{E/\mathrm{GeV}} \oplus 2\%$ for hadronic showers.

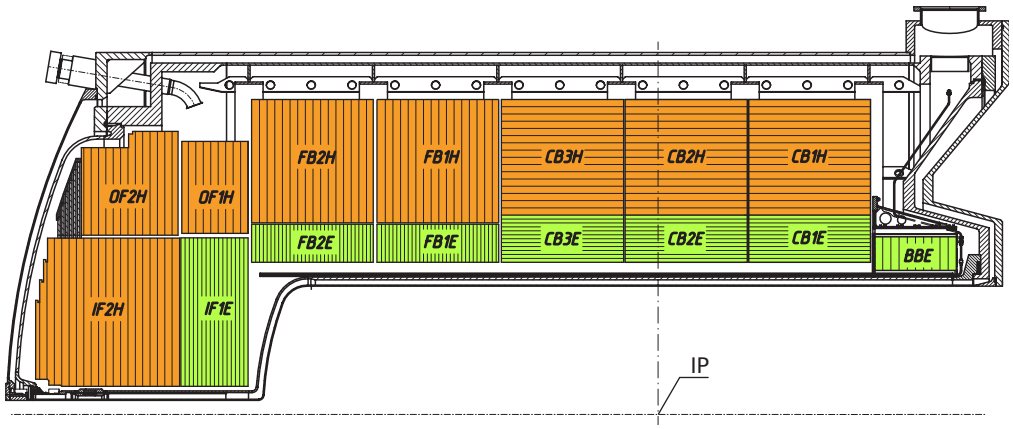

Fig. 3.5: Schematic drawing of the LAr calorimeter.

SpaCal

The backward region $153° < \theta < 178°$ is covered by so-called "Spaghetti" Calorimeter (SpaCal) [77] which was designed for precise scattered electron measurement in DIS

(Fig. 3.6). Electromagnetic and hadronic parts of this sampling calorimeter consist of lead modules with embedded scintillating fibers as an active material. The electromagnetic part corresponds to 28 radiation lengths while the hadronic part corresponds to 1 interaction length only which makes SpaCal unfeasible for the jet measurement.

Calorimeter resolution is $7\%/\sqrt{E/\mathrm{GeV}} \oplus 1\%$ for electromagnetic showers and $50\%/\sqrt{E/\mathrm{GeV}} \oplus 2\%$ for hadron induced showering.

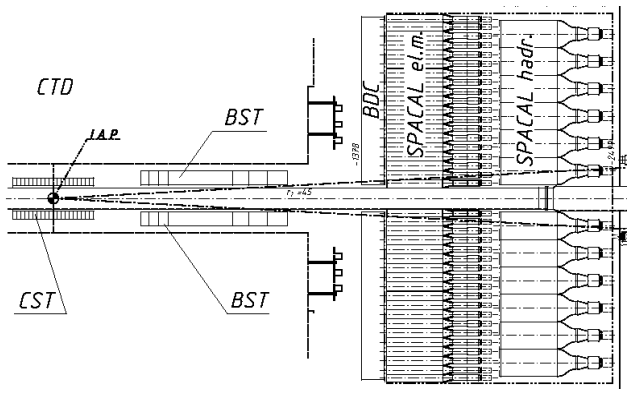

Fig. 3.6: Schematic drawing of the SpaCal calorimeter.

Very Forward Proton Spectrometer

The aim of the Very Forward Proton Spectrometer (VFPS) was to measure scattered proton kinematics in the diffractive events. With its acceptance it accompanied existing Forward Proton Spectrometer situated closer to the main H1 detector. VFPS consisted of two Roman pot stations 218 m (VFPS1) and 222 m (VFPS2) away from the interaction point. These pots were moved closer to the beam when the running conditions were stable. The scattered proton energy loss is due to a spectroscopic effect roughly proportional to the distance between proton's hit and the beam center. Using both Roman pots, global hit coordinates x, y and tilts x', y'[5] were used for full diffractive proton kinematics reconstruction.

Each VFPS Roman pot (Fig. 3.7) contains two sub-detectors measuring each the u, v coordinates oriented $\pm 45°$ with respect to the horizontal coordinate x. In total 5 planes of 120 scintillating fibers with 480 μm diameter are employed to determine u and v hit coordinates in each of the sub-detectors. In total 20 fibers from four different places are connected to the single channel of the position-sensitive photomultiplier (PSPM). Ambiguity in the hit reconstruction were solved by four trigger tiles in

[5]Global x coordinate is defined as $x = (x_1 + x_2)/2$ and tilt as $x' = (x_2 - x_1)/D_{12}$, where x_1 and x_2 are hit coordinates in VFPS1 and VFPS2, respectively. Distance between VFPS1 and VFPS2 is label by D_{12}

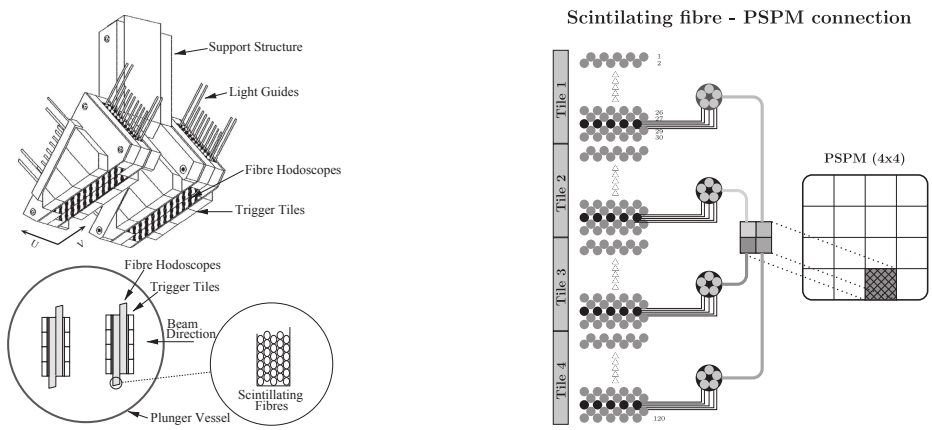

Fig. 3.7: Schematic view of VFPS Roman pot and the readout topology.

front and behind scintillating fiber horoscopes connected to separate photomultipliers. Therefore, the VFPS station incorporates four planes of trigger tiles (Fig. 3.7), where two of these planes are segmented in u-direction and two in v-direction (together 16 trigger tiles). The trigger signal from single VFPS station is positive if at least three of four expected planes fired. This triggering signal arrives at the main H1 trigger within $2\,\mu$s, fast enough to enter as level-1 trigger element.

In reality, the VFPS Roman pots were moved closer or further to the beam pipe depending on actual beam conditions. Therefore, the diffractive variables depend in addition to the hit fibers and tiles also on the Roman pots positions with respect to the beam pipe and on the beam position inside the beam pipe. The latest parameter was determined using Beam Position Monitor (BPM) located halfway the VFPS1 and VFPS2 stations, i.e. about 220 from the interaction point.

Schematic view of the beam envelope in the forward region is shown in Fig. 3.8. In the region closer than 12σ-beam from the nominal beam center (black lines) the high radiation level forbids presence of the Roman Pots stations. Hence the Forward Proton Spectrometer (FPS) can measure $x_{IP} = 0.02$ protons only if $|t| > 0.5\,\mathrm{GeV}^2$ whereas VFPS acceptance covers mainly small-t region, which has much higher cross section. On the contrary, VFPS is unable to measure protons with $x_{IP} > 0.024$ (accessible to FPS) due to shadowing by the aperture (blue).

3.2.3 Luminosity System

At HERA the actual luminosity $\mathcal{L}$ was measured using Bethe-Heitler Bremsstrahlung [78]

$$ep \to ep\gamma. \tag{3.1}$$

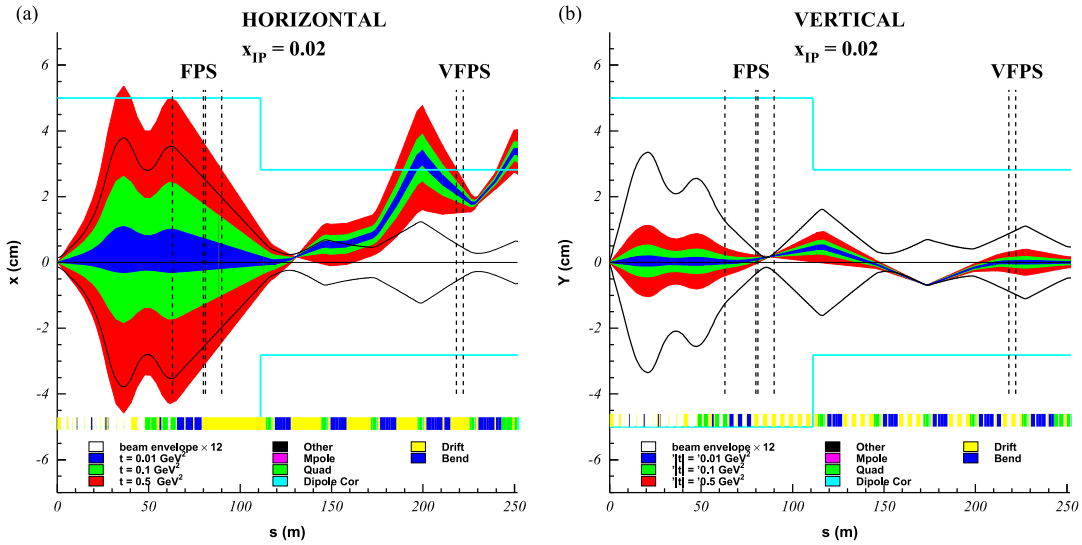

Fig. 3.8: The beam envelope [3] as a function of the distance s to the H1 vertex in the x and y projection for the p-beam and the diffractive protons at $x_{IP} = 0.02$ and $|t| = 0.01$, 0.1 and 0.5 GeV^2. The locations of the FPS/VFPS stations are indicated by the vertical dashed lines.

The luminosity is proportional to the event rate N of this process:

$$\mathcal{L} = \frac{N}{\varepsilon\sigma}, \tag{3.2}$$

where the cross section σ is calculable with high precision within perturbative QED and ε accounts for detection efficiency. Essential for luminosity measurement is high event rate of the reference process, here about $\sim$0.4 MHz. In this Bethe-Heitler process the scattered electron e is bent by very small angle of order of 20 μrad and is measured using electron tagger (Fig. 3.9) situated 33 m from the interaction point. Photon γ is measured in coincidence with electron using Cherenkov calorimeter (-103 m) with tungsten absorbers. Unfortunately due to the residual beam gas the measured event rate is contaminated by $\sim$10% background from $eA \to eA\gamma$ interactions, which have larger cross section, especially for heavy nuclei A with high electric charge. Amount of background is measured using electrons collisions with "empty" proton bunches.

Due to high event rate the Bethe-Heitler Bremsstrahlung is suitable for actual luminosity measurement. For the integrated luminosity, the detection efficiency is the highest source of the luminosity error. During HERA-II running period the integrated luminosity was determined using QED Compton process, which is the same as (3.1) but e and γ have sizable transverse momenta. In this case, e and γ are detected in the main H1 detector. Although the statistic is much smaller the overall error 2.3%

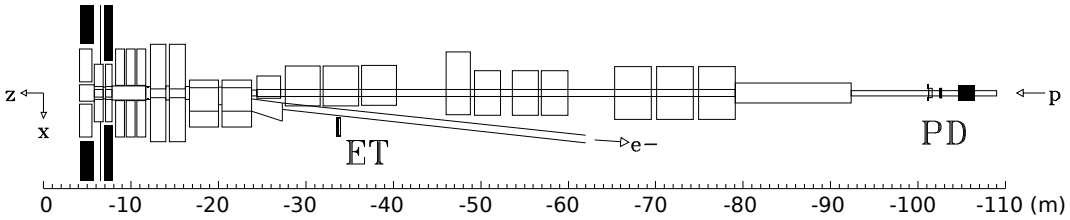

Fig. 3.9: Electron tagger (ET) and photon detector (PD).

of integrated luminosity is better.

For VFPS analysis, the Roman pots station could be moved closer only when the beam circulation is stable. This fact reduces VFPS luminosity by ∼30% and increases uncertainty to 3% [3].

3.2.4 Triggering System

The bunch crossing frequency at HERA is 10.4 MHz, but only small fraction of the bunch crossings results in an interaction and even most of these interactions have low p_T and are therefore hardly measurable by the H1 detector. In addition, there is a speed limitation originating from the maximum data storage speed of 10 Hz.

Four levels trigger system (L1-L4) is employed to select physically interesting events which would be written to the data tapes (Fig. 3.10).

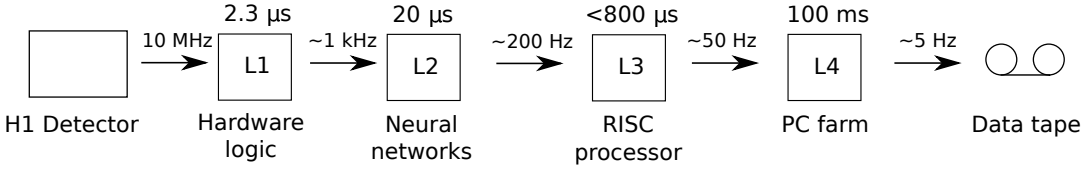

Fig. 3.10: Overview of the data flow within the H1 trigger system. Typical decision latencies and event rates are given for each trigger-level.

The H1 subdetectors provide signals to the L1. These 180 inputs are called trigger elements (TE) and are proceeded using hardware logic to the array of raw subtriggers. Each subtrigger typically corresponds to some sort of physically interesting process. For frequent process i the subtrigger could be pre-scaled by factor N_i^{pr} which means that if raw subtrigger i is true then final subtrigger is also true only with probability $1/N_i^{pr}$ and the event rate for such process is downscaled. Event is kept at this stage if at least one subtrigger has fired. Not every subdetector can provide TE information before next bunch crossing (96 ns). So there is a pipeline where temporal events are stored until all TEs arrive into central trigger logic and the decision is made. Latency between bunch crossing and L1 decision is maximally 2.3 μs and trigger information

from subdetectors must arrive within 2.1 μs which is enough even for remote VFPS. The first level trigger (L1) reduces event rate to $\sim$1 kHz.

The L2 consists of topological (L2TT) and neural network (L2NN) subtrigger. Based on L1 elements and additional information from the detector, including fast track reconstruction by the Fast Track Trigger (FTT), L2 reduces event rate to $\sim$200 Hz.

The trigger level L3 consists a farm of commercial PCs, which reconstructs event properties and decays of particles resonances from L2 tracks [79]. In this way the event rate is downscaled to $\sim$50 Hz.

On the last level (L4) the complete event reconstruction is performed. It allows to filter out remaining background (i.e. with vertex outside acceptance) and downscale "soft" events, for example low p_T photoproduction. To control L4 efficiency also 1% of events is taken regardless of L4 decision

Reconstructed data passing all trigger levels are finally written to Data Summary Tapes (DST).

Chapter 4

Overview or Diffractive Measurements

4.1 Inclusive Diffractive DIS

In the inclusive diffractive deep-inelastic scattering (Fig. 2.12)

$$ep \to eXY \tag{4.1}$$

the exchanged virtual photon dissociates into the hadronic system X and the beam proton dissociates into system Y. Both systems are typically separated by a large gap in pseudorapidity which is utilized in the large rapidity gap (LRG) selection method (section 2.3.8). Experimentally, the reduced diffractive cross sections $\sigma_r^D \simeq F_2^D$ (2.46) are measured as a function of β, Q^2 and x_{IP}[1] and can be used later on to extract diffractive parton distribution function by means of QCD DGLAP fits.

For measurements based on LRG diffractive selection the baryonic system Y can contain not only the scattered proton, but also low mass resonances, fraction of these states is highly model dependent and counts for additional systematic uncertainty of the measurement. The H1 collaboration published their LRG data in range $M_Y < 1.6\,\mathrm{GeV}$ which corresponds to fraction of $\sim 20\%$ of the proton excitation as it will be explained in the following section. On the contrary, the diffractive cross sections measured by a forward proton detector are free of proton dissociation ($M_Y = M_p$) and allow for direct extraction of proton kinematics. Unfortunately, data statistics as compared to the LRG selection method is usually smaller due to limited geometrical acceptance of proton spectrometers.

[1] The t-dependence can be extracted only by the leading proton measurement. Up to now (2015) no measurement of $\sigma_r^{D(4)}(\beta, Q^2, x_{IP}, t)$ was published. In the LRG analyses t is usually integrated up to $|t| < 1\,\mathrm{GeV}^2$.

Presently mostly used H1 2006 Fit B DPDF [4] was determined by fitting the reduced cross sections extracted from H1 1997-2000 HERA-I data of integrated luminosity $74\,\mathrm{pb}^{-1}$. The diffractive events were selected using the large rapidity gap method which restricts the diffractive kinematic range to $M_Y < 1.6\,\mathrm{GeV}$ and $|t| < 1\,\mathrm{GeV}^2$. Two alternative parametrizations of the NLO QCD DGLAP fits were tested to demonstrate low sensitivity of inclusive data to the gluonic part of the pomeron PDF (Tab. 4.1). This is a consequence of the quark-induced dominating subprocess $\gamma^* q \to q'$. Subsequently, the parametrization used in Fit B was found to be a better choice as it will be explained in the next section 4.3.

	Fit A	Fit B
Q_0^2	$1.75\,\mathrm{GeV}^2$	$2.5\,\mathrm{GeV}^2$
$zg_{IP}(z, Q_0^2)$	$A_g(1-z)^{C_g}$	A_g
χ^2/N_{df}	153/183	164/184

Tab. 4.1: Differences between parametrisations used in H1 2006 DPDF Fit A and H1 2006 DPDF Fit B [4]. Gluon contribution of the pomeron at the starting scale of the DGLAP evolution Q_0^2 is denoted as g_{IP}. The quark contribution is parametrized in the same way for both fits.

Inclusive H1 and ZEUS diffractive reduced cross sections measured at HERA-II are shown in Fig. 4.1.

For the lower values of x_{IP} (top left and top right plot) the LRG measurement is favoured, because the scattered proton is too close to the nominal beam position and is therefore hardly detectable. These plots show that the H1 2006 Fit B DPDF predictions agree satisfactorily with the H1 and ZEUS reduced cross sections across several orders of β.

The bottom left plot in Fig. 4.1 compares the reduced cross sections of H1 collaboration measured by the LRG method of selection of diffractive events to reduced cross sections measured by the Forward Proton Spectrometer (FPS). To correct for LRG phase space definition ($M_Y < 1.6\,\mathrm{GeV}$), the FPS cross sections are multiplied by a factor of 1.2, because the proton dissociative contribution is missing in the leading proton measurement.

The bottom right plot presents leading proton cross sections of H1 and ZEUS collaborations for $x_{IP} = 0.05$. The LRG cross sections are not presented due to large non-diffractive background at higher x_{IP}. Reasonable agreement between H1 and ZEUS leading proton reduced cross sections allowed to combine these measurements into one common HERA data set [81].

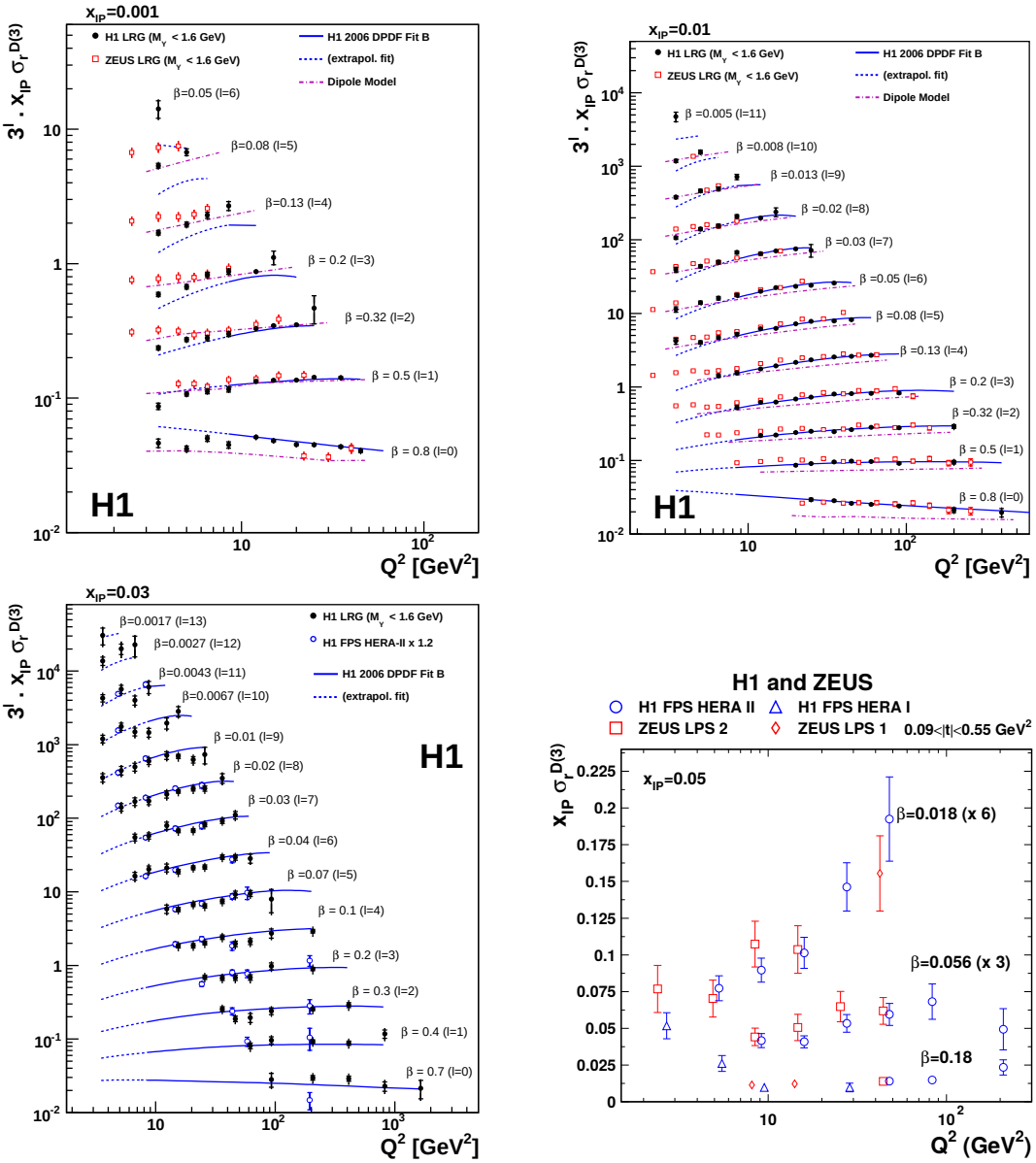

Fig. 4.1: Reduced inclusive diffractive cross section as a function of Q^2 for several x_{IP} and β values. Figures on the top show H1 and ZEUS LRG data, bottom left H1 LRG and H1 FPS [80], bottom right plot compares H1 FPS and ZEUS LPS data [81]. Data are compared to the H1 2006 Fit B DPDF [4] and the dipole model [82].

4.2 Proton Vertex Factorization

The validity of the proton vertex factorization ansatz (2.48) was tested using the Forward Proton Spectrometer [83]. For this purpose the phase space of inclusive DDIS was divided into three Q^2 intervals:

$$4 < Q^2 < 12 \quad 12 < Q^2 < 36 \quad 36 < Q^2 < 110, \quad \text{where } Q^2 \text{ is in GeV}^2 \tag{4.2}$$

and the parameters of the pomeron flux $f_{IP}(x_{IP}, t)$ (2.45) were fitted to the data in each Q^2 region independently. The results (Fig. 4.2) show no significant kinematic dependence of the pomeron flux parameters which confirms proton vertex factorization within uncertainties of the measurement. The β-dependence of pomeron flux parameters was studied as well with the same conclusion.

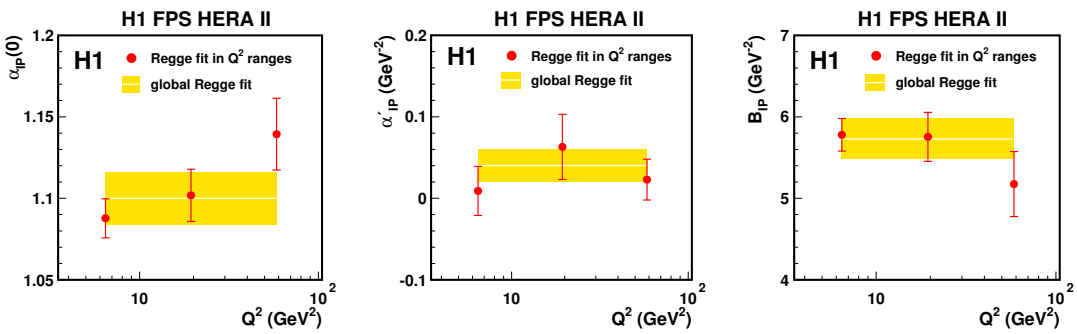

Fig. 4.2: The pomeron flux parameters $\alpha_{IP}(0)$, α'_{IP}, B_{IP} as obtained from the Regge fits as a function of Q^2 [83]. The white lines enclosed by yellow error bands denote results of the global Regge fits over full Q^2 range.

To compare the HERA cross sections measured by LRG and leading proton tagging method the fraction of proton dissociation must be known. This fraction was studied in [83] by measuring the cross sections ratio of LRG and leading proton data as a function of Q^2, β and x_{IP} (Fig. 4.3).

Within the data uncertainties, there is no significant dependence of this ratio on any variable and the ratio is compatible with constant:

$$\frac{\sigma(M_Y < 1.6\,\text{GeV})}{\sigma(M_Y = M_p)} = 1.20 \pm 0.11. \tag{4.3}$$

The lack of any kinematic dependence of this ratio of two cross sections shows that i.e. the H1 2006 Fit B DPDF can be directly used to predict cross sections of the leading proton measurements, if it is scaled down by factor of 1.2 to subtract the proton dissociation. It also evinces a remarkable consistency of the LRG and leading proton cross sections despite their very different systematics.

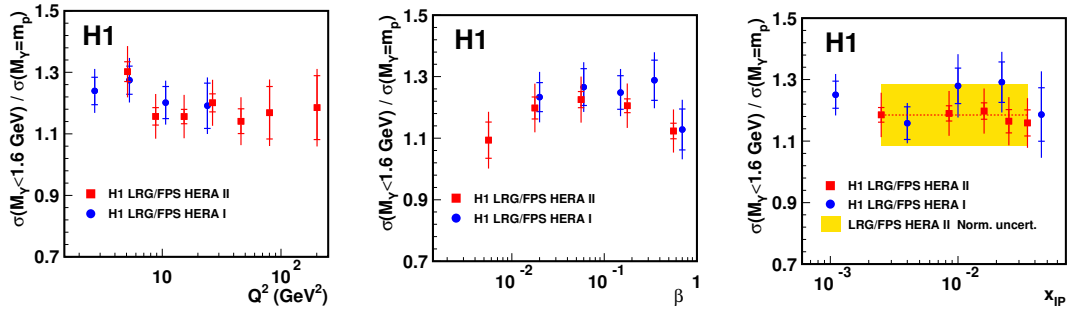

Fig. 4.3: The ratio of the inclusive diffractive cross sections measured in region $M_Y < 1.6\,\mathrm{GeV}$ obtained by the LRG method to that for $M_Y = M_p$ obtained by means of Forward Proton Spectrometer as a function of Q^2, β and x_{IP}. Both cross sections are measured in $|t| < 1\,\mathrm{GeV}^2$ range. In the most right plot the normalization uncertainty of the HERA-II global measurement is given [83].

In conclusion, the H1 collaboration measures the LRG cross sections up to $M_Y < 1.6\,\mathrm{GeV}$ which is related to the forward acceptance of H1 detector as explained in section 2.3.8. Naturally there is no "geometrical" acceptance edge of the detector at value $M_Y = 1.6\,\mathrm{GeV}$ instead the probability of detecting proton dissociative system Y increases gradually with rising masses M_Y (and values of $|t|$). Therefore the theoretical model[2] describing proton dissociation spectrum $\mathrm{d}\sigma/\mathrm{d}M_Y$ must be used to correct the measured cross sections to the exact $M_Y < 1.6\,\mathrm{GeV}$ region at the hadron level. The model uncertainty originating from badly known M_Y spectra was found to be 7% in [80] and would be larger if the cross sections were unfolded to the $M_Y = M_p$ phase space.

In publications of ZEUS collaboration are LRG cross sections presented without any proton dissociation ($M_Y = M_p$). Their results can be therefore compared directly to the leading proton cross sections but they suffer from larger model uncertainties than in the H1 approach[3].

4.3 Dijet production in diffractive DIS

The diffractive dijet production (Fig. 2.13) is dominated by the boson-gluon fusion $\gamma^* g \to q\bar{q}$ subprocess and is therefore directly sensitive to the gluonic content of the pomeron. This fact was used to test the quality of H1 2006 Fit A and Fit B DPDFs described in previous section 4.1. As can be seen in Fig. 4.4, the Fit B used

[2] At HERA, the DIFFVM Monte Carlo generator [84] is commonly used to calculate amount of proton dissociation. For example this model predicts the ratio (4.3) to be equal to $1.15^{+0.15}_{-0.08}$.

[3] At ZEUS, the amount of the proton dissociative events in diffractive data sample selected by the LRG method was estimated to be 33% [85] compared to 20% observed by H1 collaboration.

in NLO QCD predictions is favoured by the dijet measurement, both in shape and normalization.

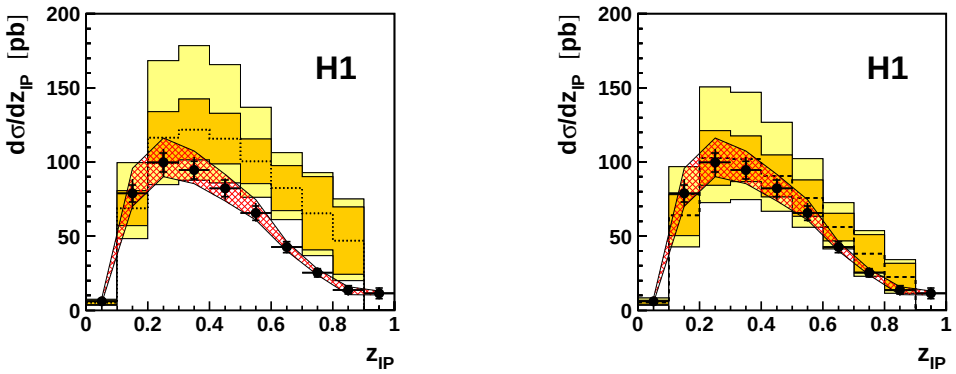

Fig. 4.4: The diffractive dijet DIS cross sections differential in z_{IP} as measured by the H1 collaboration [6]. The inner error bars on the data points represent the statistical uncertainties, while the outer error bars include the systematic uncertainties added in quadrature. The NLO QCD predictions based on H1 2006 DPDF Fit A (left) and Fit B (right) are compared to the measured cross sections (the data points on the left and right plots are identical). The inner band represents the DPDF and hadronization uncertainty, the outer band shows full theory uncertainty including the QCD scale uncertainty added in quadrature.

Even more recent measurement from 2014 with much larger statistics (Fig. 4.5) shows satisfactory agreement between data and NLO QCD predictions, so that the validity of QCD collinear factorization is confirmed in this process.

In DIS there are two comparable hard scales, Q^2 and $(p_T^{*\mathrm{jet}})^2$, i.e. jet's transverse momentum squared in the $\gamma^* p$ frame, which can by used in QCD calculations. Specific form of the QCD hard scale is a matter of convention, but of course it influences the predicted cross section. Lower scale means higher α_s and therefore higher theoretical cross section. For that reason the overview of all existing DDIS measurements (Tab. 4.2) contains in addition to the data and NLO QCD cross sections also the QCD scale used. Note that within theoretical and data uncertainties the cross sections of all measurements agree with the corresponding theoretical predictions. Different phase space regions of the measurements (e.g. in the measured x_{IP} range) causes that the values of the measured cross sections vary up to one order of magnitude.

To better restrict gluon fraction of the DPDF, both HERA collaborations made combined QCD DGLAP fits to inclusive and dijets DDIS data. Resulting DPDFs are called H1 2007 Fit Jets [6] and ZEUS SJ [88]. Unfortunately, the theoretical errors of the NLO QCD calculations originating from scale variation (sec. 2.5) are quite large and make the use of these data for QCD fits less attractive.

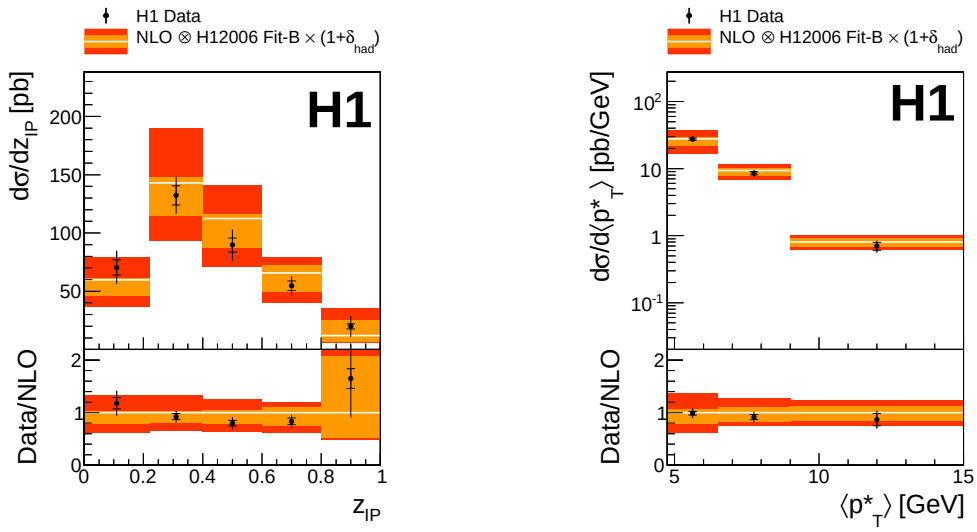

Fig. 4.5: The diffractive dijet DIS cross sections differential in z_{IP} and the average p_T^* of the dijet system $\langle p_T^* \rangle$ as measured by the H1 collaboration [86]. The inner error bars on the data points represent the statistical uncertainties, while the outer error bars include the systematic uncertainties added in quadrature. The NLO QCD predictions based on H1 2006 Fit B DPDF are compared to the measured cross sections. The inner band band represents the DPDF and hadronization uncertainty, the outer band shows full theory uncertainty including the QCD scale uncertainty added in quadrature.

4.4 Diffractive Dijet Production in Hadron-Hadron Collisions

Measurement of hard diffractive interactions in pp or $p\bar{p}$ has long history, starting in 1988 [89] by discovery of jets in the diffractive events at UA8. The existence of these events was theoretically predicted already in 1984 by Ingelman and Schlein [68]. Later on, DPDFs were extracted from inclusive ep DDIS reduced cross sections at HERA and have been there extensively studied. These DPDFs, allow for p-QCD calculations, assuming validity of QCD collinear factorization for considered diffractive process. Hard scale, essential for p-QCD applicability, is in hadron-hadron collision typically provided by high-p_T dijet or vector boson system. However already in 1992, there was a suggestion [46] of factorization breaking in diffractive hadron-hadron interactions[4], caused by spectator interactions which may fill rapidity gap and destroy leading proton.

This predicted phenomenon was really discovered at Tevatron in diffractive W [90]

[4]Suppression of data with respect to perturbative QCD calculation based on collinear factorization by an order of magnitude

DESY	07-018	07-115	11-166	14-200	07-126
Experiment	H1	H1	H1	H1	ZEUS
Reference	[17]	[6]	[87]	[86]	[8]
σ_{Data} [pb]	30 ± 4	52 ± 6	254 ± 34	73 ± 7	90 ± 8
σ_{NLO} [pb]	31^{+9}_{-6}	57^{+22}_{-15}	270^{+135}_{-55}	77^{+25}_{-25}	102^{+25}_{-16}
μ_r^2	$(E_T^{*\mathrm{jet1}})^2$	$(E_T^{*\mathrm{jet1}})^2 + Q^2$	$\langle E_T^{*\mathrm{jet}}\rangle^2 + Q^2$	$\langle E_T^{*\mathrm{jet}}\rangle^2 + Q^2$	$(E_T^{*\mathrm{jet1}})^2$
$\frac{\sigma_{\mathrm{Data}}}{\sigma_{\mathrm{NLO}}}$	$0.97^{\pm 0.13}_{\pm 0.24}$	$0.91^{\pm 0.11}_{\pm 0.30}$	$0.94^{\pm 0.13}_{\pm 0.36}$	$0.95^{\pm 0.09}_{\pm 0.31}$	$0.88^{\pm 0.08}_{\pm 0.18}$

Tab. 4.2: Data and NLO QCD cross sections of HERA DDIS dijets measurements. In all cases the H1 2006 Fit B DPDF was used for the theoretical predictions. In measurement [87] data were selected by means of Forward Proton Spectrometer, the remaining analyses are based on the LRG method of selecting diffractive events. The data cross sections σ_{Data} are accompanied by the total uncertainty representing the quadratic sum of the statistical and systematic errors. The uncertainty of the theoretical cross sections σ_{NLO} dominantly follows from the QCD scale variation (section 2.5). The ratios of data cross sections to theoretical cross sections are accompanied by the data uncertainties in the superscript and the theoretical uncertainties in the subscript.

and dijet [10] production.

Most recent measurement of this effect is shown at Fig. 4.6. The CMS collaboration [11] measured the differential cross section for events with low $\tilde{\xi} = \min(\xi^+, \xi^-)$, where $\xi^\pm$ are calculated from hadronic final state as:

$$\xi^+ = \frac{\sum_{\eta_i < 4.9}(E_i + P_z^i)}{\sqrt{s}} \qquad \xi^- = \frac{\sum_{\eta_i > -4.9}(E_i - P_z^i)}{\sqrt{s}}. \tag{4.4}$$

Events with low $\tilde{\xi}$ (analog of x_{IP}) are expected to be mostly single diffractive (Fig. 4.6):

$$pp \to XY \qquad (M_X \gg M_Y), \tag{4.5}$$

where system Y is either scattered proton or its low mass excitation, $\tilde{\xi}$ has interpretation as a fractional momentum loss of system Y compared to the beam proton. System X is required to contain at least two jets with transverse momenta above 20 GeV.

The Fig. 4.6 shows that non-diffractive (ND) Pythia 8 prediction [91] fails to describe low $\tilde{\xi}$ events while agrees for higher $\tilde{\xi}$, where lower fraction of diffractive events is expected. Single-diffractive and double-diffractive (SD+DD) Pythia 8 prediction [92] based on Regge-like parameterisation of soft diffractive cross section is systematically lower than the data cross sections. The models which include hard diffractive phenomenon and are based on H1 2006 Fit B DPDF (LO Pompyt [93] and NLO POWHEG) overestimated the measured cross section similarly to the measurements at Tevatron.

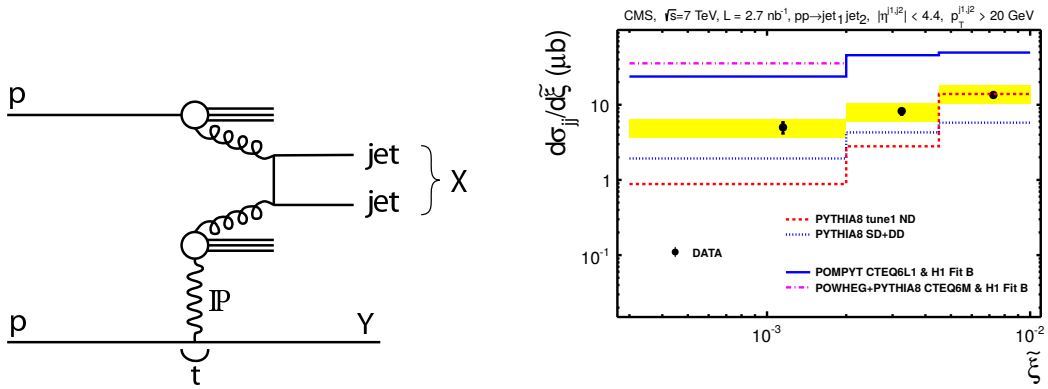

Fig. 4.6: Differential dijet cross section as a function of $\tilde{\xi}$ as was measured by CMS collaboration [11] at centre-of-mass energy of $\sqrt{s} = 7\,\text{GeV}$ (right plot). Data are compared to several theoretical predictions. The Feynman diagram of the single diffractive dijet production which dominates in the first $\tilde{\xi}$ bin is depicted on the left.

Unfortunately the resulting data suppression with respect to NLO prediction suffers from large model uncertainty due to proton dissociation, which is absent in POWHEG calculations. Using CMS estimate for fraction of proton dissociation ($\sim$40%) in their data, the measured rapidity gap survival probability for the first bin of Fig. 4.6 is

$$S^2_{\text{NLO}} = 0.08 \pm 0.04, \tag{4.6}$$

in agreement with theoretical models [54, 55, 94] which were briefly discussed in section 2.3.7.

4.5 Diffractive Dijet Photoproduction

In the diffractive dijet photoproduction, the low virtuality photon exchange may dissociate into non-perturbative hadronic bound state. This process (known as resolved photon interaction) resembles hadron-hadron interaction, therefore can serve as a vital tool to study the validity of QCD collinear factorization theorem. Naturally, photon can also couple directly to the hard subprocess and these processes are called direct (see Fig. 2.13). At leading order, the experimental discriminator between these two regimes of photoproduction is x_γ, defined by the relation (2.50).

Up to now two published [16, 17] and one preliminary [70] measurements made by H1 collaboration and one measurement of the ZEUS collaboration [18] exist. All these analyses are based on LRG method of selecting diffractive events. On the other hand, different methods were used to select low Q^2 events. In the H1 measurements, the electron is directly measured by the electron tagger situated 33 m away from the interaction point. Acceptance of this tagger restricts photon virtuality to $Q^2 < 0.01\,\text{GeV}^2$.

In the ZEUS analysis, events are selected using condition of absence of a scattered electron in the main detector which leads to the interval $Q^2 < 1\,\mathrm{GeV}^2$. Phase spaces of H1 and ZEUS measurements are compared in detail in Tab. 4.3 and the measured cross sections and the NLO QCD predictions are presented in Tab. 4.5.

The x_γ distributions from all mentioned analyses are shown in Fig. 4.7. Note that x_γ distribution agrees well in shape for all measurements and there is no indication of resolved contribution ($x_\gamma < 0.8$) being more suppressed than direct one, as predicted by several models [15, 95, 96].

H1	ZEUS	H1 Preliminary
$Q^2 < 0.01\,\mathrm{GeV}^2$	$Q^2 < 1\,\mathrm{GeV}^2$	$Q^2 < 0.01\,\mathrm{GeV}^2$
$0.3 < y < 0.65$	$0.2 < y < 0.85$	$0.3 < y < 0.65$
$E_T^{\mathrm{jet1}} > 5\,\mathrm{GeV}$	$E_T^{\mathrm{jet1}} > 7.5\,\mathrm{GeV}$	$E_T^{\mathrm{jet1}} > 7.5\,\mathrm{GeV}$
$E_T^{\mathrm{jet2}} > 4\,\mathrm{GeV}$	$E_T^{\mathrm{jet2}} > 6.5\,\mathrm{GeV}$	$E_T^{\mathrm{jet2}} > 6.5\,\mathrm{GeV}$
$-1 < \eta^{\mathrm{jet1,2}} < 2$	$-1.5 < \eta^{\mathrm{jet1,2}} < 1.5$	$-1.5 < \eta^{\mathrm{jet1,2}} < 1.5$
Diffractive cuts		
$x_{IP} < 0.03$	$x_{IP} < 0.025$	$x_{IP} < 0.025$
$z_{IP} < 0.8$		
$\lvert t\rvert < 1\,\mathrm{GeV}^2$	$\lvert t\rvert < 1\,\mathrm{GeV}^2$	$\lvert t\rvert < 1\,\mathrm{GeV}^2$
$M_Y < 1.6\,\mathrm{GeV}$	$M_Y = M_P$	$M_Y < 1.6\,\mathrm{GeV}$

Tab. 4.3: Phase space definitions used in H1 2010 [16] and ZEUS 2007 [8] and H1 Preliminary [70] analyses. Previous H1 measurement from 2007 [17] differs from the newer one only by absence of the z_{IP} restriction.

In the first H1 measurement [17] suppression S^2 of data with respect to NLO QCD calculation using H1 2006 Fit B of 0.5 ± 0.2 was measured. To reduce the data systematic uncertainty and the theoretical uncertainty the double ratio

$$\frac{(\mathrm{DATA/NLO})_{\mathrm{PHP}}}{(\mathrm{DATA/NLO})_{\mathrm{DIS}}} = 0.5 \pm 0.1 \tag{4.7}$$

was determined. This procedure requires to measure also DIS cross section in comparable phase space (section 4.3), differing only by the Q^2 interval. Previous observation of factorization breaking was confirmed by newer H1 publication [16] ($S^2 = 0.6 \pm 0.2$) with 3 times higher luminosity.

On the contrary, the measurement of ZEUS collaboration is compatible with no suppression hypothesis, measured suppression factors are $S^2 = 0.8 \pm 0.2$ for H1 2006 Fit B DPDF and $S^2 = 1.0 \pm 0.2$ for ZEUS SJ DPDF [88].

The difference between kinematic regions of both experiments leads in [97] to a hypothesis that the suppression may depend on the E_T range of the jets (see Tab. 4.3). In H1 analysis [70] where the phase space was changed to a phase space as close

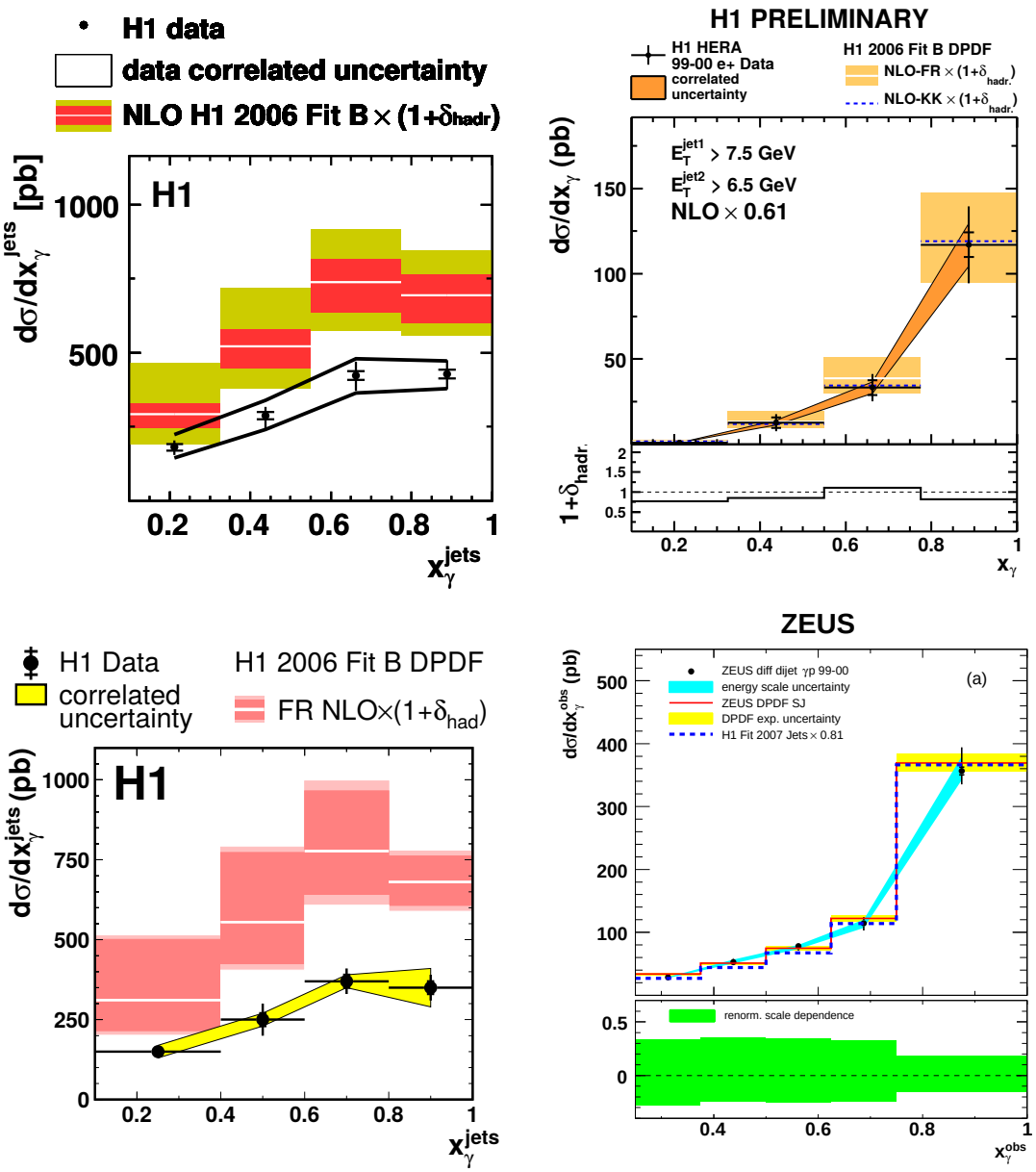

Fig. 4.7: Differential cross sections as a function of x_γ as measured in [16] (top left), [70] (top right), [17] (bottom left), [88] (bottom right). The NLO QCD calculation in H1 preliminary analysis (top right) were multiplied by factor of 0.61.

as possible to ZEUS one (Tab. 4.3) the suppression 0.6 was measured. Thus the inconsistency between collaborations remained unexplained.

Theoretical calculations of both collaborations[5] [16, 18] were crosschecked in [98, 99], the only inconsistency was found in the hadronization corrections calculated by both collaborations. On the other side, the hadronization corrections recalculated for ZEUS differ in such a way that their application to NLO calculations will make the difference in suppressions of both experiments even larger, as is shown in Tab. 4.4.

	H1		ZEUS	
	recalculated	original	recalculated	original
H1 Fit B	0.57	0.58	0.88	0.77
H1 Fit Jets	0.63	0.64	1.08	1.01
ZEUS SJ	0.72	0.70	1.11	0.98

Tab. 4.4: Suppression factors $S^2 = \sigma_{\mathrm{DATA}}/\sigma_{\mathrm{NLO}}$ measured by the H1 [16] and ZEUS [18] collaborations. On the right are original values published by each collaboration, on the left are the recalculated values [99], where exactly the same method was used for both analyses phase spaces defined in Tab. 4.3. Uncertainties of S^2 originating from the data and QCD scale variation are about 20% and 25%, respectively.

In [99], there was made an attempt to transfer ZEUS [18] and H1 preliminary High-Pt data [70] into the same phase space and compare the data sets directly. Since the only difference between measurement's phase spaces is broader y and Q^2 in ZEUS analysis, the ZEUS data were transformed to H1 High-Pt phase space by method based on MC Rapgap (Fig. 4.8). Model dependence of such procedure was studying using several DPDF fits and two photon distributions functions (GRV and AFG) and it was found to be negligible due to high resemblance of both phase spaces. This study concluded that the observed discrepancy between H1 and ZEUS results concerning factorization breaking is not caused by different phase space of both analyses.

The puzzle of factorization breaking in diffractive dijet photoproduction could be resolved by new experimental analyses. Among them the most promising one is the identification of diffractive events based on leading proton detection; such analysis is presented in this thesis. This method has both an advantage of providing a data sample free of proton dissociation and of reducing the uncertainties of the diffractive selection if compared with large rapidity gap method.

[5] The H1 collaboration use program of Frixione at all. [66] for the theoretical predictions while the ZEUS collaboration employs an alternative NLO QCD program of Klasen and Kramer [69].

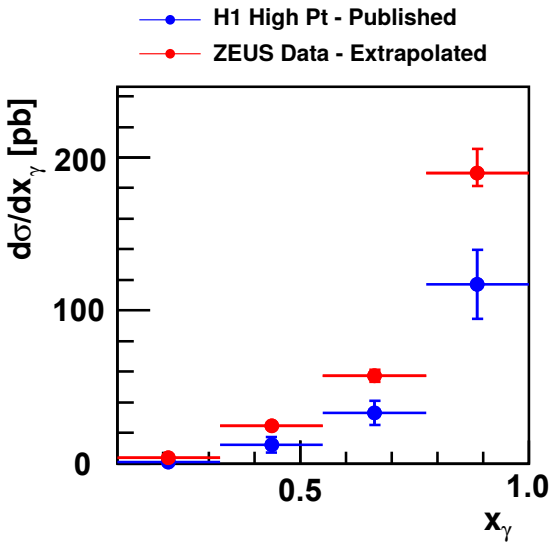

Fig. 4.8: H1 High-Pt preliminary data cross section differential in x_γ [70] compared to ZEUS cross sections [18] transformed to the same phase space. This plot was presented in [99].

DESY	07-018	10-043	prelim.	07-161
Experiment	H1	H1	H1	ZEUS
Reference	[17]	[16]	[70]	[18]
σ_{Data} [pb]	243 ± 33	295 ± 58	37 ± 8	124 ± 9
σ_{NLO} [pb]	500^{+170}_{-120}	510^{+150}_{-150}	61^{+10}_{-8}	161^{+40}_{-32}
$\frac{\sigma_{\text{Data}}}{\sigma_{\text{NLO}}}$	$0.49^{\pm 0.07}_{\pm 0.14}$	$0.58^{\pm 0.12}_{\pm 0.17}$	$0.61^{\pm 0.13}_{\pm 0.15}$	$0.77^{\pm 0.06}_{\pm 0.19}$

Tab. 4.5: Data and NLO QCD cross sections of HERA PHP dijets measurements. In all cases, the H1 2006 Fit B DPDF was used for the theoretical predictions and the diffractive events were selected using the LRG method. The data cross sections σ_{Data} are accompanied by the total uncertainty representing the quadratic sum of the statistical and systematic errors. The uncertainty of the theoretical cross sections σ_{NLO} dominantly follows from the QCD scale variation (section 2.5). The ratios of data cross sections to theoretical cross sections are accompanied by the data uncertainties in the superscript and the theoretical uncertainties in the subscript.

Chapter 5

Data Selection and Reconstruction

5.1 Analysed Data Sample

The analysed data sample consists of e^+ neutral current H1 data with forward proton, detected by VFPS, collected during HERA-II operation phase. The events were split into several VFPS Periods corresponding to different beam optics configuration which results in alternating beam position (Fig. 5.1). The VFPS operation was stable from VFPS Period 6, but the analysis subtrigger S103 started to operate smoothly later on, therefore only events from VFPS Periods 11-16 are used in the presented measurement (Tab. 5.1). The data sample corresponds to the run range 487289-500611 (November 17, 2006 - March 20, 2007).

Not all runs in the mentioned interval were usable, the operation of the detector components important for current analysis (LAr and SpaCal calorimeters, CJC, CIP, FTT, LAr triggering system and the luminosity system) must be required and only runs classified either as good or medium quality according to the detector performance and background conditions were chosen. Other runs were rejected due to unstable beam conditions inappropriate for the VFPS measurement.

The subtrigger S103 is pre-scaled by different factors varying from run to run, the average pre-scale of ~ 1.7 leads to effective integrated luminosity in photoproduction of $30\,\mathrm{pb}^{-1}$ compared to original $50\,\mathrm{pb}^{-1}$. For the DIS data triggered by S103 in many cases also another non-pre-scaled subtrigger requiring scattered electron in SpaCal was fired. This is used to increase the effective integrated luminosity of the DIS data sample up to $50\,\mathrm{pb}^{-1}$.

The event properties are stored in the Object Data Store (ODS) format which incorporates parameters of reconstructed tracks and clusters as well as important detector informations. Average data size of event in this format is around $\sim 13\,\mathrm{kB}$

VFPS Period	Run range	VFPS Luminosity [pb^{-1}]	Beam Pos. x[mm]	Year
9	482627 - 487166	10.6	-3.0	06e^+
11	487216 - 489641	10.3	-3.0	06e^+
12	488610 - 492231	7.9	-4.5	06e^+
14	492252 - 495284	13.0	-4.5	07e^+
15	495380 - 498987	12.3	-4.5	07e^+
16	499007 - 500611	7.2	-4.0	07e^+

Tab. 5.1: The overview of the VFPS Periods and the corresponding VFPS luminosities. Note the seeming overlap of periods 11 and 12, in reality runs in the range 487216 – 492231 were sort out according to Beam Position into two categories which are not completely separated in time.

depending on the event complexity. The μODS formats contains four-vectors of the physical particles and pointers to the ODS tracks and clusters that it was built from ($\sim 3\,$kB/event) and is, therefore, suitable for most physical analyses. For fast selection of appropriate events even smaller data format ($\sim 0.4\,$kB/event) named HAT which contains summary about event kinematics and particle multiplicities can be used. The H1 Object Oriented (H1OO) physics analysis framework [100] written in C++ is then employed to process the data files as well as MC files.

The variables describing the leading proton kinematics as measured by VFPS were missing in these standard data storage formats and only raw information about the tracks in VFPS was present. I incorporate the reconstruction of the diffractive variables into standard H1OO analysis framework moreover several improvements on the reconstruction precision and reliability were made. The standard storage format of the VFPS variables allows for easier and faster access to the measured diffractive kinematics which is utilized not only in this analysis but also in measurement of D* in diffractive photoproduction performed by diploma student Markéta Jansová [101].

5.2 MC Samples

The signal event sample was generated by the Rapgap 3.1 MC generator [59] which relays on the QCD factorization theorem and is based on $\alpha_{em}\alpha_s^0$ and $\alpha_{em}\alpha_s^1$ matrix elements for direct-photon subprocesses and α_s^2 for the resolved ones (more detailed information about MC Rapgap was given in section 2.4). The direct-photon subprocesses implemented in Rapgap are shown in Fig. 5.2, where the process (b) is known as boson-gluon fusion. The QCD Compton process (not shown in Fig. 5.2) represents about 17% of the direct photon cross section and was also taken into account.

To generate the diffractive events, the H1 2006 DPDF fit B was used as a proton

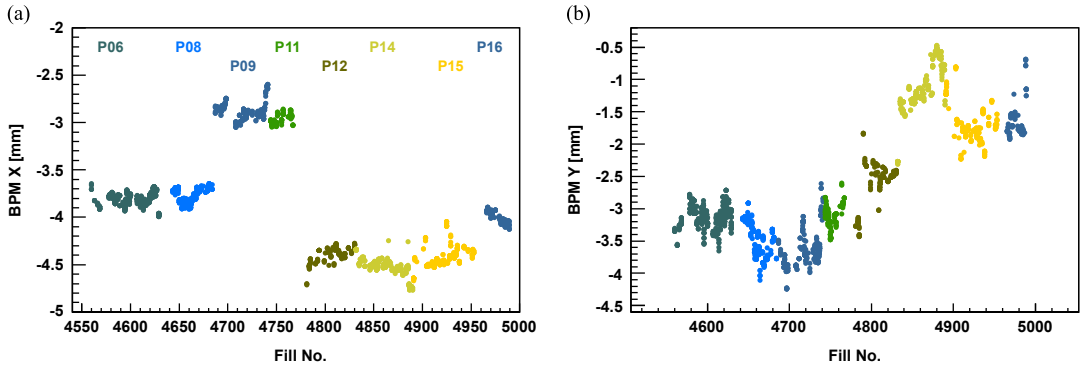

Fig. 5.1: Beam position, measured by Beam Position Monitor (BPM) as a function of the Fill number in x-direction (a) and y-direction (b) [3]. VFPS Periods, which split the data set into several subsets with stable x and y beam positions, are labeled by different colors.

DPDF [4]. In the photoproduction regime, the resolved photon is described using GRV LO γ-PDF [49]. Events are generated in the broader phase space than the phase space of the measurement which allows to study of phase space migrations; in particular, there is no restriction on inelasticity y and x_{IP} is simulated up to $x_{IP} = 0.1$. Soft events are cut off by requiring $\hat{p}_T$ of outgoing partons in the hard subprocess being larger than 1.7 GeV. To study possible migrations between the PHP and DIS phase spaces, the corresponding MC samples overlap as it is shown in Tab. 5.2.

PHP	DIS
$Q^2 < 6\,\mathrm{GeV}^2$	$2 < Q^2 < 1000\,\mathrm{GeV}^2$

Tab. 5.2: Ranges of the exchanged photon virtuality for the PHP and DIS MC samples.

The parameters of the generated MC samples are summarised in Tab. 5.3. It is worth to note that the event weights were applied to suppress rate of non-interesting low-p_T events. In addition to the pomeron contribution the subleading reggeon contribution, which represents around 2% of the total cross section in the measured region, was included as well.

All the MC samples in Tab. 5.3 are passed through a detailed H1 detector and VFPS simulation program H1SIMREC based on the GEANT [65] and are subjected to the same analysis chain as it is used for data. Since the input H1SIMREC parameters of the beam optics and VFPS stations positions differ within the VFPS Periods, each MC sample is split into several VFPS Periods according to their integrated data luminosities and the simulation is run separately for each VFPS Period with proper settings of the parameters.

Process	PHP		DIS	
	Pomeron	Reggeon	Pomeron	Reggeon
$q\gamma^* \to q'$ $\bar{q}\gamma^* \to \bar{q}'$	-	-	$12 \cdot 10^6$ $727\,\mathrm{pb}^{-1}$	$1.1 \cdot 10^6$ $1008\,\mathrm{pb}^{-1}$
$g\gamma^* \to q\bar{q}$	$6 \cdot 10^6$ $716\,\mathrm{pb}^{-1}$	$0.4 \cdot 10^6$ $650\,\mathrm{pb}^{-1}$		
$q\gamma^* \to q'g$ $\bar{q}\gamma^* \to \bar{q}'g$	$2 \cdot 10^6$ $833\,\mathrm{pb}^{-1}$	-		
$g\gamma^* \to c\bar{c}$	$3 \cdot 10^6$ $631\,\mathrm{pb}^{-1}$	-	$5 \cdot 10^6$ $2325\,\mathrm{pb}^{-1}$	-
Resolved	$11 \cdot 10^6$ $194\,\mathrm{pb}^{-1}$	$0.8 \cdot 10^6$ $121\,\mathrm{pb}^{-1}$	-	-

Tab. 5.3: Overview of generated MC processes. Six PHP and three DIS MC samples are presented in this table together with the MC statistics of events and the integrated luminosity.

To determine QED radiative and hadronization corrections the MC samples without QED radiation and QED virtual corrections were generated at the level of stable hadrons (i.e. without the detector simulation) as well.

5.3 Reconstruction of the Kinematics

The method of reconstruction the kinematic variables describing diffractive dijet production depends on the considered region of the photon virtuality Q^2. In the DIS, the scattered positron is measured using SpaCal which allows for a precise reconstruction of the kinematic invariants Q^2 and y related to the scattered positron angle and energy. In the PHP region, the scattered positron leaves H1 undetected[1], therefore, the kinematics of the scattered positron has to be determined indirectly by means of the hadronic final state objects measured in the main H1 detector.

Other variables are mostly reconstructed in the same way in photoproduction and DIS.

5.3.1 Leading Proton Kinematics

The reconstruction of the leading proton kinematics within VFPS is based on the global hit coordinates x, y and angles x', y'. These quantities are calculated by means of the local hit coordinates x_1, y_1 and x_2, y_2 measured in corresponding VFPS1 and

[1]The Electron Tagger used in previous H1 measurements [16, 17] was not operating during the HERA-II phase.

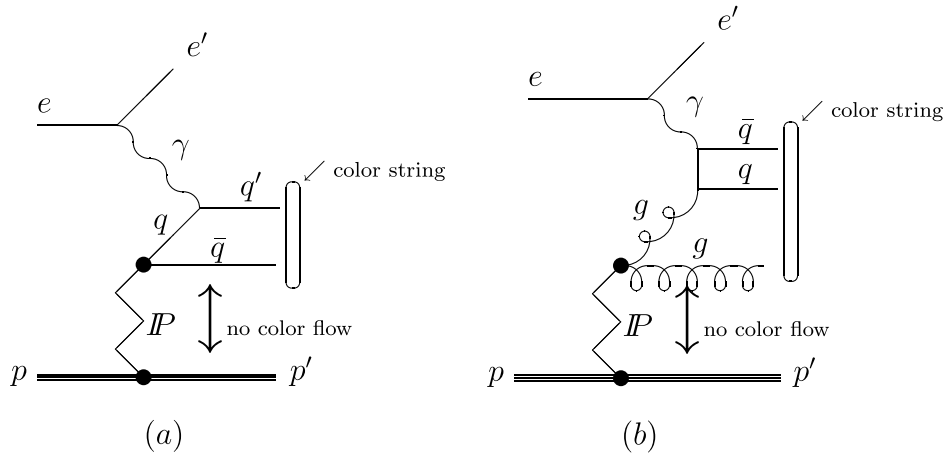

Fig. 5.2: Feynman diagrams of the direct-photon diffractive processes implemented in RAPGAP [59]. (a) shows lowest order process $\gamma q \to q'$, (b) represents $\gamma g \to q\bar{q}$. Note the missing color flow between the outgoing proton and the $\gamma^* I\!P$ system which causes the presence of the large rapidity gap in the diffractive events.

VFPS2 stations as:

$$x = \frac{x_1 + x_2}{2} \qquad y = \frac{y_1 + y_2}{2}, \tag{5.1}$$

$$x' = \frac{x_1 - x_2}{d} \qquad y' = \frac{y_1 - y_2}{d}, \tag{5.2}$$

where the $d \simeq 4\,\mathrm{m}$ is the distance between VFPS stations. Furthermore, the coordinates have to be corrected for the beam position measured by BPM and the position of the Roman Pots.

The beam optics and the VFPS simulation implemented in H1SIMREC links the kinematic parameters of the leading proton with the global VFPS coordinates:

$$\begin{pmatrix} x_{I\!P} \\ \theta_x \\ \theta_y \end{pmatrix} \xrightarrow{\text{H1SIMREC}} \begin{pmatrix} x \\ y \\ x' \\ y' \end{pmatrix}, \tag{5.3}$$

where the angles θ_x and θ_y represent the proton scattered angles as calculated in xz- and yz-planes, respectively. Naturally holds, that $\theta = \sqrt{\theta_x^2 + \theta_y^2}$. The correlation between VFPS variables x, x', y, y' and $x_{I\!P}$, θ_x, θ_y is demonstrated in Fig. 5.3. Such plots do not contain the whole information about the proton propagation through the beam optics because the problem cannot be fully separated between x and y directions. Therefore, the positions of contours shown on the left plot also depend on angle θ_y and

analogously contours on the right plot depend on angle θ_x, although the dependence on the orthogonal angle is always weaker.

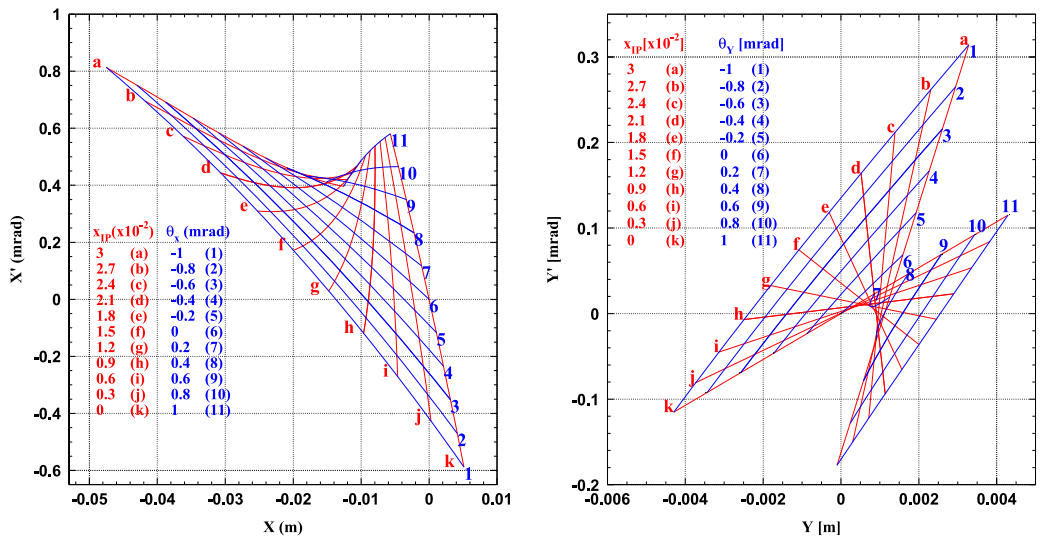

Fig. 5.3: Correlation of track position and track angle at a location halfway between the VFPS stations in the (x, x')-plane (left) and (y, y') (right) for diffractive protons with given x_{IP}, θ_x and θ_y at the primary vertex [3]. Note that θ_y on the left plot and θ_x on the right plot are set to be equal to 0.

The neural network method was employed to invert relation (5.3) and extract the proton kinematic quantities from known hit coordinates:

$$\begin{pmatrix} x \\ y \\ x' \\ y' \end{pmatrix} \xrightarrow{\text{Neural net}} \begin{pmatrix} x_{IP} \\ \theta_x \\ \theta_y \end{pmatrix}. \tag{5.4}$$

Note, that the beam optics configuration varies between the VFPS Periods and consequently also the weights describing the neural network are not constant.

The knowledge of x_{IP}, θ_x and θ_y allows for reconstruction of the leading proton azimuthal angle ϕ and the four-momentum transfer at the proton vertex t by formulas:

$$t = -E_p^2(1 - x_{IP})(\theta_x^2 + \theta_y^2) \qquad \phi = \arctan\frac{\theta_y}{\theta_x}, \tag{5.5}$$

where $E_p = 920\,\text{GeV}$ is the nominal proton beam energy[2].

[2]The expression for angle ϕ of vector (θ_x, θ_y) holds only if $\theta_x > 0$. The general solution for arbitrary θ_x and θ_y provides C++ function `atan2` as $\phi = \texttt{atan2}(\theta_y, \theta_x)$.

The quality of the x_{IP} reconstruction was checked by the data sample of the diffractive ρ mesons in the DIS [3]:

$$ep \to e\rho p \to e\pi^+\pi^- p. \tag{5.6}$$

In this process, the scattered electron and two tracks of the opposite charge originating from the ρ decay are required in the main H1 detector. Data were selected using S115 subtrigger which requires trigger signal in at least one VFPS station and scattered lepton in SpaCal. The variable x_{IP} can be then reconstructed using momenta of pion tracks and the electron by formula (2.36) which can be rewritten as:

$$x_{IP}^{\rho} = x\left(1 + \frac{M_X^2}{Q^2}\right), \tag{5.7}$$

where x denotes the Bjorken scaling variable determined from the angle and energy of the scattered electron. The $M_X^2 \sim 0.6\,\mathrm{GeV}^2$ corresponds to the square of the ρ mass and thus the term M_X^2/Q^2 represents only small[3] correction in equation (5.7). Consequently the x_{IP}^{ρ} resolution is mostly given by the resolution of x. The measured absolute difference between x_{IP}^{VFPS} and x_{IP}^{ρ} is shown in Fig. 5.4 and is compared with the MC prediction based on DIFFVM model [84] of vector meson production. The both x_{IP} variables measured by the independent methods coincide well, albeit the MC predicts a little bit better "resolution".

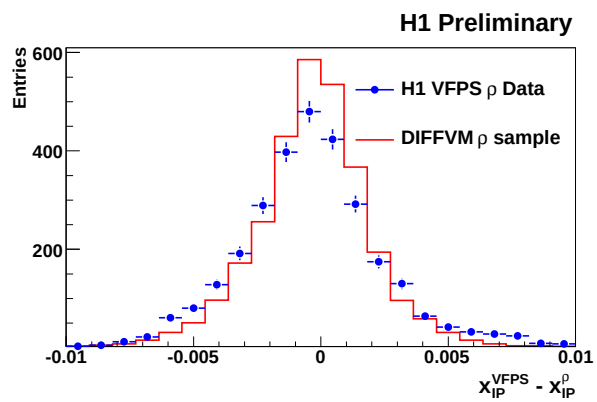

Fig. 5.4: The plot of the absolute difference between x_{IP}^{VFPS} measured by means of VFPS and x_{IP}^{ρ} reconstructed from scattered electron and pion tracks in $\rho \to \pi^+\pi^-$ decay. The measured data are compared with the MC simulation (red line) of the diffractive vector meson production DIFFVM [84].

The ρ meson data sample has been also used to check the track efficiency of the VFPS stations by comparing the total event rate in particular x_{IP}^{ρ} bin to the event

[3]Due to the acceptance of SpaCal, the Q^2 was required to be $Q^2 > 4\,\mathrm{GeV}^2$.

rate, where, in addition, the track is reconstructed in `VFPS1`, `VFPS2`, `VFPS1||VFPS2` and `VFPS1&&VFPS2`. The resulting fractions shown in Fig. 5.5 indicate good description of the track efficiency obtained from data by the simulation within the data statistical uncertainties and the plotted 5% uncertainty band. Due to low statistics of the ρ data sample, the resulting track and triggering efficiency of VFPS have been also studied by using single VFPS station as a reference to measure the efficiency of the other one. The obtained efficiencies are within 2.5% described by the simulation [3] which is considered later on as a systematic uncertainty of the VFPS track reconstruction and VFPS trigger element efficiency.

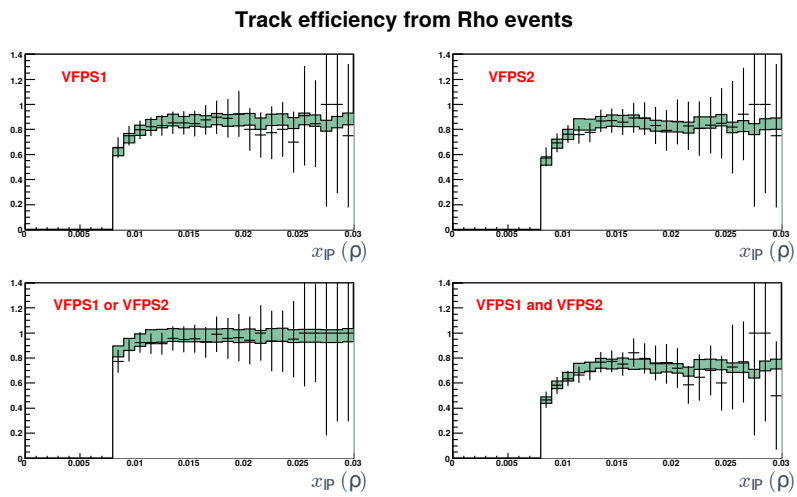

Fig. 5.5: The efficiency of the VFPS reconstruction, as estimated from the ρ mesons data sample. The data (black points) are compared to the MC simulation, plotted with $\pm 5\%$ uncertainty band. [102]

In previous paragraphs the quality of the x_{IP} VFPS measurement was discussed by studying its efficiency and resolution. The precise reconstruction of the remaining diffractive variables t and ϕ is, however, a challenge compared to the reconstruction of x_{IP}, which is roughly proportional to the distance of the hit position to the beam. At the moment, the quality of the t reconstruction is still not sufficient to measure cross section differentially in this variable. Not sufficient performance of the t reconstruction led to freezing of the $F_2^{D(4)}$ inclusive DIS analysis with the leading proton detected in VFPS in the preliminary status [103]. In this preliminary analysis the structure function was measured in x_{IP}, β and Q^2 variables only. On the other hand, the resolution of the x_{IP}^{VFPS} has been crosschecked by several methods.

5.3.2 Reconstruction of the HFS Objects

The hadronic final state (HFS) is reconstructed using the energy flow algorithm Hadroo2 [104] which combines information from tracks and calorimeter clusters.

If the relative energy resolution of the track measurement is smaller than the estimate of the calorimeter resolution (section 3.2.2) calculated from this track[4]:

$$\frac{\sigma_{E_{track}}}{E_{track}} < \frac{0.5}{\sqrt{E_{track}}}, \tag{5.8}$$

then the track energy measurement is used. In this case, the measured energy obtained from charged track has to be subtracted from the energy in the calorimeter to avoid double counting. Otherwise, if the inequality (5.8) is false, the track is removed and the cluster energy is taken as the energy of the final state object. The relative resolutions of tracker and calorimeter as a function of the energy of the track are shown in Fig. 5.6 and, as excepted, the track measurement is more precise at smaller energies. For more detailed information see [104].

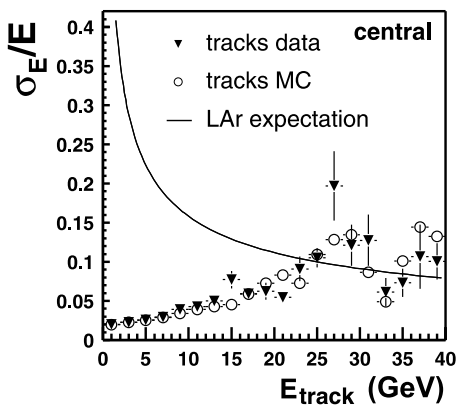

Fig. 5.6: The relative energy resolution for the central tracks ($20° < \theta < 160°$) as obtained from data and MC events compared to the LAr expectation [104].

The invariant mass M_X of the system X is reconstructed from all hadronic objects in the main H1 detector:

$$M_X^2 = \left(\sum_{i \in X} E_i\right)^2 - \left(\sum_{i \in X} \vec{P}_i\right)^2. \tag{5.9}$$

The HFS objects four-momenta boosted into $\gamma^* p$ frame represent inputs to the inclusive k_T jet algorithm (section 2.6) implemented in the FastJet package [105]. A

[4]Each track is assumed to have the pion mass within the Hadroo2 algorithm.

jet distance parameter is set to $R = 1$ and the massless p_T recombination scheme is employed. In the PHP measurement, where no scattered positron is measured, the outgoing positron is assumed to be parallel to the z-axis, which makes the laboratory and $\gamma^* p$ frames identical up to the boost in z-direction.

The found jets are sorted by the transverse jet energies in the $\gamma^* p$ frame, the superscript "1" labels the leading (hardest) and "2" the subleading jet in the transverse energy. The jet properties are studied in terms of the transverse energies $E_T^{*\mathrm{jet1}}$, $E_T^{*\mathrm{jet2}}$, invariant dijet mass M_{12} and the pseudorapidity variables $|\Delta\eta^{\mathrm{jets}}|$ and $\langle\eta^{\mathrm{jets}}\rangle$.

The invariant dijet mass M_{12} is defined as

$$M_{12}^2 = \left(J^{(1)} + J^{(2)}\right)^2, \tag{5.10}$$

where $J^{(1)}$ and $J^{(2)}$ are four-momenta of the two leading jets transformed back to the laboratory frame. The pseudorapidities η^{jet1} and η^{jet2} are calculated by formula $\eta = -\ln\tan\frac{\theta}{2}$ using corresponding vectors $J^{(1)}$ and $J^{(2)}$. The mean jets pseudorapidity $\langle\eta^{\mathrm{jets}}\rangle$ and the absolute value of the jets pseudorapidity difference $|\Delta\eta^{\mathrm{jets}}|$ are defined in the standard way:

$$|\Delta\eta^{\mathrm{jets}}| = \left|\eta^{\mathrm{jet1}} - \eta^{\mathrm{jet2}}\right| \qquad \langle\eta^{\mathrm{jets}}\rangle = \frac{1}{2}\left(\eta^{\mathrm{jet1}} + \eta^{\mathrm{jet2}}\right). \tag{5.11}$$

5.3.3 DIS Selection

For the DIS event selection, the polar angle θ'_e and the energy E'_e of the scattered positron are measured using the SpaCal calorimeter and position of the primary interaction vertex. To estimate the invariants Q^2 and y a reconstruction method introduced in [106] is employed. It makes use of the good precision of the "electron method" at high y and the "double-angle method" at low y:

$$y = y_{DA}(1 - y_{DA}) + y_e^2, \tag{5.12}$$

where the y_e is reconstructed only from the scattered positron energy and its angle[5] ("electron method")

$$y_e = 1 - \frac{E'_e}{E_e}\sin^2\frac{\theta'_e}{2} \tag{5.13}$$

and y_{DA} is calculated from the angle of the hadronic system γ_h

$$\cos\gamma_h = \frac{p_{x,h}^2 + p_{y,h}^2 - (E_h - p_{z,h})^2}{p_{x,h}^2 + p_{y,h}^2 + (E_h - p_{z,h})^2}, \tag{5.14}$$

[5] Note that zero deflection of positron corresponds within H1 coordinate system to $\theta'_e = 180°$, in particular, for small angular deviation holds $y = 1 - \frac{E'_e}{E_e}$.

where four-vector $p_h = (E_h, p_{x,h}, p_{y,h}, p_{z,h})$ represents the sum of four-momenta of all hadronic final state objects, and the angle of the scattered positron θ'_e:

$$y_{DA} = \frac{E_e}{E_p} \frac{\sin\gamma_h + \sin\theta'_e + \sin(\theta_e + \gamma_h)}{\sin\gamma_h + \sin\theta'_e - \sin(\theta_e + \gamma_h)}. \tag{5.15}$$

The photon virtuality Q^2 is then reconstructed using the y calculated above (5.12):

$$Q^2 = \frac{4E_e^2(1-y)}{\tan^2\frac{\theta'_e}{2}}. \tag{5.16}$$

The momentum fraction z_{IP} of parton entering to the hard subprocess with respect to the pomeron is reconstructed by formula:

$$z_{IP}^{obs} = \frac{Q^2 + M_{12}^2}{Q^2 + M_X^2}, \tag{5.17}$$

where the dijet invariant mass M_{12}^2 depends on the parameters of the jet algorithm and, therefore, z_{IP}^{obs} may not exactly be equal to the z_{IP} defined by the relation (2.50).

5.3.4 Photoproduction Selection

In photoproduction, the positron candidate is required to be absent in the H1 detector (typically in SpaCal), therefore the variable y must be reconstructed only from the hadronic final state employing the Jaquet-Blondel method [107]:

$$y = \frac{E_h - p_{z,h}}{2E_e}. \tag{5.18}$$

Note, that in photoproduction, y has clear physical interpretation as a fractional energy loss of the scatted positron ($y = 1 - \frac{E'_e}{E_e}$). In principle, the photon virtuality Q^2 could be also expressed by means of the hadronic final state and leading proton four-momenta, however, in reality, due to the poor resolution, this Q^2 reconstruction method cannot provide any useful information about the value of Q^2 in the photoproduction regime, where these photon virtualities are very low (see Fig. 5.11).

The observables z_{IP}^{obs} and x_γ^{obs} are reconstructed only from the hadronic final state X:

$$z_{IP}^{obs} = \frac{\sum_{i\in jets}(E_i + p_{z,i})}{E_h + p_{z,h}} \qquad x_\gamma^{obs} = \frac{\sum_{i\in jets}(E_i - p_{z,i})}{E_h - p_{z,h}}, \tag{5.19}$$

where the sums in numerators runs over two leading jets in the transverse energy reconstructed by the inclusive k_T-algorithm as described in sec. 5.3.2. Note, that denominator in relation (5.19) for observable z_{IP}^{obs} could be also calculated using the information from VFPS, as $2x_{IP}E_p$, but the final resolution of the z_{IP}^{obs} is in this approach worse, because possible uncertainties in numerators and denominators of (5.19) are partially correlated and therefore are partially cancelled in ratio.

5.4 Events Selection

5.4.1 Phase Space Definition

The hadron-level phase space of the photoproduction and DIS analyses is presented in Tab. 5.4. It was inspired by the phase space of the preceding H1 measurement of diffractive photoproduction of dijets [16], but it was adjusted to a VFPS selection of diffractive events and the different photoproduction selection method. The DIS region then differs only in photon virtuality Q^2.

Kinematic Quantities

$0.2 < y < 0.7$	
Photoproduction $Q^2 < 2\,\mathrm{GeV}^2$	Deep-inelastic scattering $4\,\mathrm{GeV}^2 < Q^2 < 80\,\mathrm{GeV}^2$

Diffractive selection

$0.010 < x_{IP} < 0.024$
$\lvert t\rvert < 0.6\,\mathrm{GeV}^2$
$z_{IP}^{obs} < 0.8$

Jet Definition

$E_T^{*\mathrm{jet1}} > 5.5\,\mathrm{GeV}$
$E_T^{*\mathrm{jet2}} > 4.0\,\mathrm{GeV}$
$-1 < \eta^{\mathrm{jet1,2}} < 2.5$

Tab. 5.4: Phase space of the diffractive dijet VFPS measurement for photoproduction and deep-inelastic scattering.

The condition on the positron inelasticity y ensures that the energy deposit of hadronic final state is located within the tracker and calorimeter acceptance, which is especially important in photoproduction, where y is calculated only from HFS. The upper bound of the y cut also reduces possible DIS background in photoproduction, because low energy positrons in SpaCal can be more likely misidentified.

The selection intervals in photon virtuality Q^2 relate to the SpaCal acceptance. Especially for events with Q^2 above $80\,\mathrm{GeV}^2$ the highly deflected positron typically scatters to LAr calorimeter which has worse resolution of the electromagnetic part than SpaCal. The "dead" interval between 2 and $4\,\mathrm{GeV}^2$ corresponds to the region where the SpaCal starts to detect the scattered leptons, but is not able to reconstruct reliably their kinematics. Note that in the previous analysis [16] the electron tagger was employed to measure the scattered electrons. This detection method allows for precise electron kinematic reconstruction, in particular without any DIS background,

but has lower acceptance compared to the untagged photoproduction.

The x_{IP} and t cuts reflect the acceptance of the Very Forward Proton Spectrometer.

The highest z_{IP}^{obs} region is removed for the theoretical reasons. The H1 2006 Fit B DPDF [4] used for the theoretical predictions in this analysis was fitted only in interval $z_{IP} < 0.8$ and for the higher z_{IP} values the DPDF was only extrapolated.

The $E_T^{*\text{jets}}$ cuts are comparable to the previous analysis, only the cut on the leading jet is made to be a little bit higher (5.5 instead of 5 GeV) to ensure a good performance of the NLO QCD calculations. The measurement of jets can be extended here to more forward region than in analyses using LRG method of selecting diffractive events. This is due to the fact that the LRG selection method requires the forward part of the calorimeter to be without energy deposit. For this reason, the upper limit on jet pseudorapidity η is set to be 2.5, compared to 2 in LRG analyses.

5.4.2 Trigger selection

In the presented analysis the same subtrigger S103 is used both for photoproduction and DIS regime. The main conditions required by this trigger are the presence of two hard tracks in the tracker, small energy deposit in the forward part of the LAr calorimeter and triggering signal from both VFPS stations. The subtrigger definition does not contain any condition on the positron candidate, neither positive nor negative, which makes this subtrigger applicable for both phase space regions of the presented analysis. The precise definition of subtrigger S103 varies within its operating time and can be split into three time periods D1, D2 and D3. The number of triggered events as a function of integrated luminosity is shown in Fig. 5.7. The data obtained during the D1 subtrigger running interval are not considered, especially due to strict condition on small energy deposit in forward part of LAr calorimeter.

The subtrigger definition during phase D2 and D3 is presented in Tab. 5.5. These phases differ only by L2 trigger element `FTT_Td_gt_1_zvtx` which is included in D3, but missing in D2 time period. All remaining trigger elements belong to category L1 (see sec. 3.2.4) and are the same for both operating periods. Note, that Fig. 5.7 shows smaller event rate per $1\,\text{pb}^{-1}$ for period D3 than for D2, which is caused by extra trigger element condition in the definition of period D3. However, this dissimilarity almost vanishes when only events fulfilling the jet requirements are considered.

The H1 detector simulation H1SIMREC includes simulation of all trigger elements presented in Tab. 5.5. To check the quality of this simulation, an alternative subtrigger S115 is used as a reference which requires triggering signal in VFPS1 or VFPS2 and signal from the scattered lepton in SpaCal. This subtrigger can be used to select diffractive DIS data sample with leading proton, either inclusive or dijet.

The inefficiencies defined as:

$$\text{InEff}(\texttt{TE}) = 1 - \frac{\sigma(\text{S115}\&\texttt{TE})}{\sigma(\text{S115})} \tag{5.20}$$

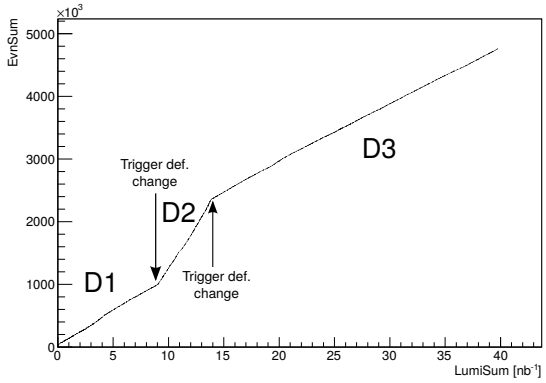

Fig. 5.7: The event yield of the S103 subtrigger as a function of the integrated luminosity from the start of S103 operation. The definition of the S103 subtrigger was changing over the time, which leads to the change of the yield curve slope.

were estimated for each trigger element using the dijet data sample and compared to the simulation. The results are presented in Tab. 5.6. It is assumed that the topology of the hadronic final state for events in the photoproduction and DIS region is similar and thus also the S103 subtrigger simulation performance in these two regimes is comparable and, therefore, the same corrections of the trigger simulation can be applied in both discussed kinematic regimes. According to the Tab. 5.6, the most inefficient trigger element is the `CIP_sig` > 2 of which inefficiency is underestimated by the simulation. The inefficiencies of other trigger elements are much smaller and are within data errors described by the trigger simulation (only the measured `LAr_IF` inefficiency is a little bit smaller than simulated).

The inefficiency of the most ineffective trigger element `CIP_sig` > 2 was found to be nearly kinematically independent in the inclusive data sample and was described by the simulation if the overall efficiency normalization is corrected by the factor of 5%[6]. This factor is comparable with factor $(3.0 \pm 1.5)\%$ obtained from Tab. 5.6. As a compromise based on these observations, it is assumed that these correction factors are identical, therefore the correction factor of 5% is used in the presented measurement. The overall uncertainty of this factor is taken to be 5% which ensures that efficiencies of all data points of the dijet reference sample lie within this band, as shown in Fig. 5.8.

Uncertainties of the other trigger elements were found to be negligible, compared to the uncertainty of the `CIP_sig` > 2. The error of the `VFPS1` && `VFPS2` part of the S103 was determined to be 2.5% [3] including the track reconstruction efficiency.

As was already mentioned in section 5.1, the subtrigger S103 had been for many

[6]The uncertainty of the integrated inefficiency, determined from the statistics of the inclusive VFPS sample, is 0.5%.

VFPS1 && VFPS2	Trigger signal in both VFPS stations
LAr_IF < 2	Small energy deposit in the forward part of LAr
FTT_mul_Tc > 1	At least two tracks with p_T above 400 MeV
!FTT_topo_6	Avoid single hemisphere track topology
CIP_sig > 2	Two times more central tracks compared to the forward and bakcward in CIP
CIP_cosmic	Signal coincidence in 2 quadrants of azimuthal angle in CIP
CIP_T0	At least one central track in CIP
FTT_Td_gt_1_zvtx	At least two tracks with p_T above 900 MeV and well reconstructed z-vertex position

Tab. 5.5: The definition of subtrigger S103 for time period D3. During the foregoing phase D2, the trigger element FTT_Td_gt_1_zvtx was absent which led to higher event rate during this time period.

Trigger Element	Inefficiency from DDIS dijet analysis	
	Data [%]	Simulation [%]
LAr_IF < 2	0.4 ± 0.2	1.3 ± 0.1
FTT_mul_Tc > 1	0.0 ± 0.1	0.2 ± 0.0
!FTT_topo_6	0.9 ± 0.4	0.9 ± 0.1
CIP_sig > 2	11.5 ± 1.2	8.5 ± 0.3
CIP_cosmic	0.0 ± 0.1	0.1 ± 0.0
CIP_T0	2.5 ± 0.6	2.1 ± 0.2
FTT_Td_gt_1_zvtx	2.3 ± 0.6	1.9 ± 0.1

Tab. 5.6: The inefficiencies of individual trigger elements of S103 as obtained from the analysis using the reference subtrigger S115.

runs prescaled and it lowers the real integrated luminosity from 50 to 30 pb^{-1}. Actually, if event fulfils all conditions summarised in Tab. 5.5, it only guaranties that the raw S103 subtrigger is set to be true. The value of subtrigger S103 is then set to be true only with probability 1/RunPrescale, otherwise it is false. The event is stored if at least one subtrigger is true. For the DIS events, the positron hits SpaCal and therefore the DIS subtriggers S115 which is without any prescale is fired. Then the majority of the DIS events for which is raw S103 subtrigger true are stored no matter if the S103 subtrigger was set to zero due to the prescale.

This fact was utilized using an algorithm described in [108], which determines the actual event weight by the following code:

```
if( S103Raw && (S103 || S115) ) {
```

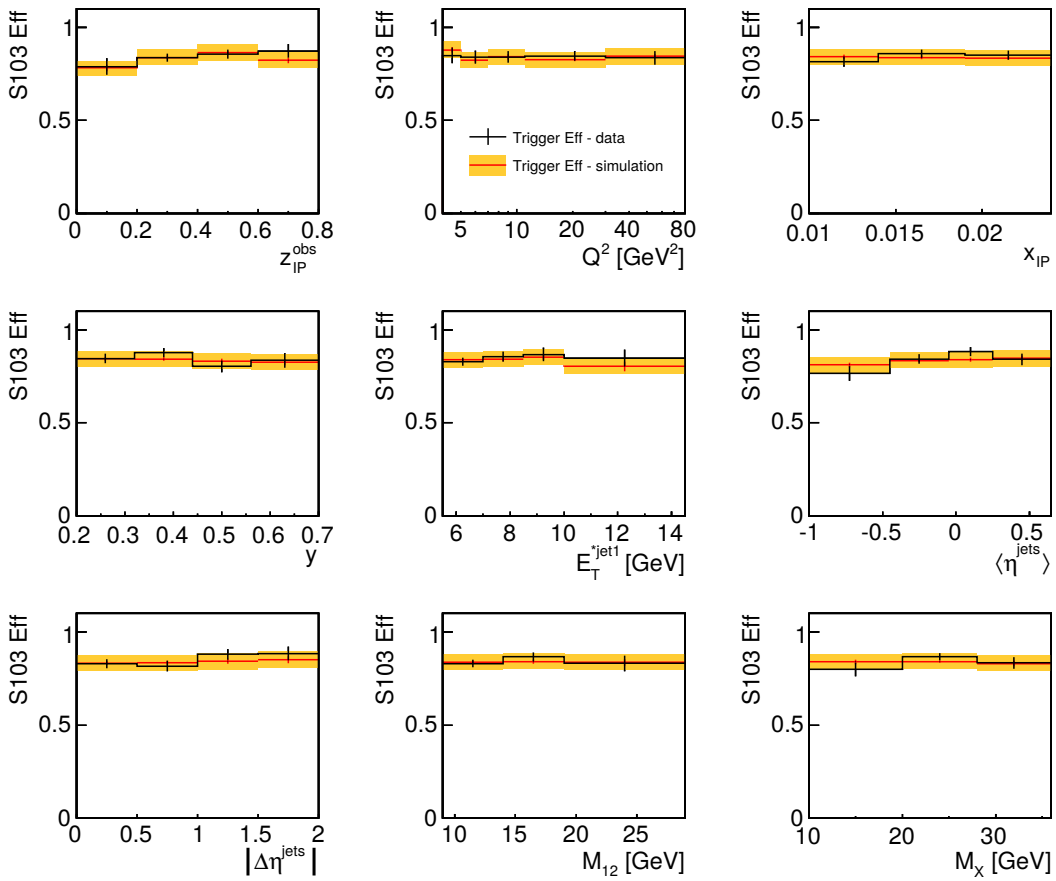

Fig. 5.8: The S103 trigger efficiency as estimated from the S115 reference dijet data sample. The efficiency obtained from the corrected simulation is accompanied by 5% uncertainty band.

```
    if(S115)
        Weight = 1;
    else
        Weight = 1.7
}
```

The value $1.7 \simeq 50/30$ is the average S103 prescale and S103Raw, S103 and S115 denote the logical values of raw S103 subtrigger, S103 subtrigger and S115 subtrigger. Note, that if the S115 had never fired, the code above would every time result in Weight of 1.7. In reality the S115 fired in 99% of DIS events fulfilling raw S103 condition which effectively increases the integrated luminosity from 30 to $50\,\mathrm{pb}^{-1}$.

5.4.3 Vertex Reconstruction

The precise measurement of the vertex position is essential for the reconstruction of the whole event kinematics. Specially the directions of the leading proton and the scattered positron are determined with respect to the actual interaction point. The position of the primary vertex is determined using the fit to the CJC and CST hits [109], in case of DIS, the compatibility of the vertex position and the scattered positron track is checked.

The vertex z-position is Gaussian-like distributed (Fig. 5.9) with mean around the origin of the coordinate system and $\sigma_z \sim 9\,\mathrm{cm}$, where the z-coordinate varies due to large longitudinal beam size. The imposed cut $-30\,\mathrm{cm} < z_{vtx} < 30\,\mathrm{cm}$ ensures good reconstruction of the event kinematic quantities and reduces the possible beam-gas interaction background significantly, which is, after applying all selection cuts below 1%.

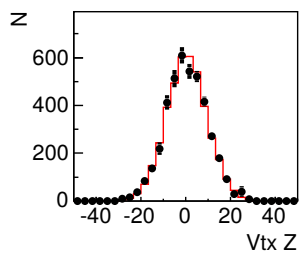

Fig. 5.9: The distribution of the z_{vtx} coordinate in the photoproduction kinematic phase space as seen in data (black points) and in the simulation (red line).

5.4.4 The VFPS Selection Criteria

The selection of the diffractive event is based on the detection of the leading proton in the Very Forward Proton Spectrometer. The analysis subtrigger S103 requires triggering signal from both VFPS stations, which means the presence of a signal in at least 3 of 4 scintillating trigger tiles in each station. However, the positive triggering signal does not guarantee the presence of reconstructed proton track. Therefore, the successfully reconstructed local tracks in both stations are required. These local tracks are in the next step combined into single global track described by coordinates x, y and angles x' and y'. Furthermore, the upper limit on the coordinate x is imposed to avoid a problematic region where the absorption of protons by the beam aperture plays significant role[7]. This cut is defined using `Fidu` variable:

$$\texttt{Fidu} = x_{limit}^{Period} - x, \tag{5.21}$$

[7]See the beam pipe edge at $\sim$200 m depicted by the cyan line in Fig. 3.8.

where the constant x_{limit}^{Period} varies between VFPS Periods because the beam optic configuration differs as well and its values are between 25 mm and 29 mm.

The random overlap of ep events with beam-halo protons detected in the VFPS can constitute a possible background to the VFPS diffractive data sample. In such background events, the detected proton typically has a small energy loss, not compatible with the energy loss expected from the energy deposited in the main H1 detector. The relative energy loss of the proton detected in VFPS, x_{IP}^{VFPS}, is thus required to be at least 60% of x_{IP}^{H1} measured in the H1 detector and reconstructed by relation (2.36).

Variable x_{IP}^{H1} is required to be smaller than 0.04. The VFPS acceptance drops to zero already for $x_{IP} > 0.03$, therefore there is a high probability, considering the resolution of the x_{IP}^{H1}, that the proton measured in VFPS in event where $x_{IP}^{H1} > 0.04$ originates from another interaction. The remaining background contamination after applying the above cuts is estimated from data by overlaying events without VFPS activity with VFPS signals recorded independently of any detector activity and it is found to be less than 1% [3] (see Fig. 5.10).

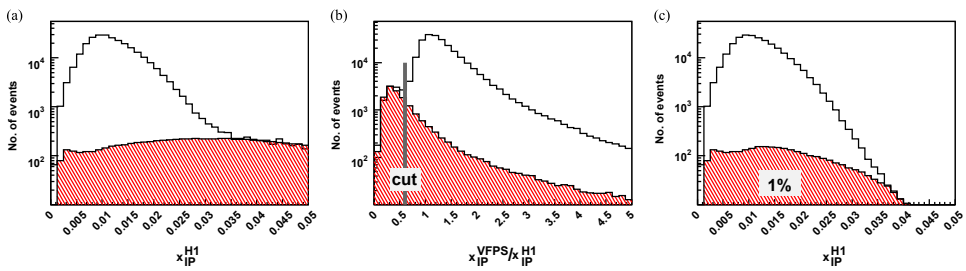

Fig. 5.10: The figures shows the amount of the background events (red area) in the data sample with signal in VFPS. The area $x_{IP}^{H1} > 0.04$ in the plot (a) is used to fix the normalization of the background. The plot (b) justifies the cut $\frac{x_{IP}^{VFPS}}{x_{IP}^{HFS}} > 0.6$ and the plot (c) includes this cut and in addition the condition $x_{IP}^{HFS} < 0.04$ which leads to a background fraction of 1%.

The phase space region in x_{IP}, where the cross section is measured is chosen in accordance to the VFPS acceptance, $0.010 < x_{IP} < 0.024$[8]. No restrictions on the reconstructed four-momentum transfer at the proton vertex t and proton azimuthal angle ϕ are introduced, but the resulting hadron level cross section is corrected to $|t| < 0.6\,\mathrm{GeV}^2$ which roughly corresponds to the VFPS acceptance in variable t. All selections conditions are summarised in Tab. 5.7.

[8]Note that restriction on x_{IP}^{VFPS}, $0.010 < x_{IP}^{VFPS} < 0.024$, together with $\frac{x_{IP}^{VFPS}}{x_{IP}^{HFS}} > 0.6$ automatically ensures that $x_{IP}^{HFS} < 0.04$.

`JTSTc_VFPS1_nr` $= 1$	Track reconstructed in VFPS1
`JTSTc_VFPS2_nr` $= 1$	Track reconstructed in VFPS2
`JTGTc_nr` $= 1$	Presence of global track
`Fidu` $> 0.6\,\mathrm{mm}$	Fiducial cut on x-coordinate
$0.010 < x_{IP}^{VFPS} < 0.024$	Determines the diffractive phase space
$\frac{x_{IP}^{VFPS}}{x_{IP}^{HFS}} > 0.6$ $x_{IP}^{HFS} < 0.04$	Cuts to suppress beam halo interactions

Tab. 5.7: The diffractive selection criteria at the detector level

5.4.5 Jet Selection

The jets were identified in the $\gamma^* p$ frame by the inclusive k_T jet algorithm as described in section 5.3.2. The transverse energies of the leading and subleading jet are required to be $E_T^{*\mathrm{jet1}} > 5.5\,\mathrm{GeV}$ and $E_T^{*\mathrm{jet2}} > 4.0\,\mathrm{GeV}$, respectively. These cuts ensure the existence of the QCD hard scale in the selected events required by perturbative calculations and moreover the asymmetric conditions remove problematic part of the phase space where the negative virtual NLO QCD contributions cannot be compensated by the real emissions [110]. These conditions guarantee that NLO QCD calculations are reliable and can be compared to the measured data. The transverse jet criteria are also motivated experimentally because the energy resolution deteriorates with decreasing E_T and also the jet energy scale calibrations starts to be not well justified for lower E_T.

The pseudorapidities of both jets in the laboratory frame are dictated by the geometrical acceptance of the LAr calorimeter. The conditions $-1 < \eta^{\mathrm{jet1,2}} < 2.5$ ensure that not only the jet center but the majority of the jet energy is always deposited within the calorimeter[9].

5.4.6 Selection of the Photoproduction Events

During the HERA-II operation phase the electron tagger did not operate, therefore, the only possibility is to measure untagged photoproduction, similarly to the ZEUS analysis of the diffractive dijet photoproduction [18]. In this case, the photoproduction event is accepted if no positron candidate is present in the final state, usually in SpaCal. Criteria imposed on the positron candidate are discussed in detail in section 5.4.7. The most important topic for current discussion is the energy of associated cluster in SpaCal. When the energy of the cluster is lower than 8 GeV, the cluster is not identified as originating from scattered positron and this can fake the photoproduction

[9] The geometrical acceptance of LAr calorimeter is $-1.5 < \eta < 3.4$.

signal. To remove possible DIS background, the upper bound of inelasticity y is introduced, in particular little deflected positron with energy 8 GeV corresponds to $y = 1 - 8/27.6 = 0.71$. In addition, also events with $y < 0.2$ are removed from the analysis. These events have energy deposit in the very forward region, as is seen from relation (5.18), and, consequently, the HFS may not be well detected within calorimeter and tracker acceptance.

The effect of the SpaCal geometry on the photoproduction phase space is illustrated by extracting the deflection angle $\vartheta'_e = 180° - \theta'_e$ of the scattered positron from formula (5.16) which results in simple expression:

$$\vartheta'^2_e = \frac{Q^2}{E_e^2(1-y)}, \tag{5.22}$$

where $E_e = 27.6\,\mathrm{GeV}$ is the nominal beam energy of the positron. This formula is analogous to relation (5.5) for diffractive proton, where Q^2 is analogue of $-t$ and y of x_{IP}. It was derived assuming small angle ϑ'_e, however, even for $\vartheta'_e = 20°$ is the relative error of used approximation only 1%. The deflection angle is, therefore, proportional to Q and inversely proportional to $\sqrt{1-y}$. As a result of this formula, events with $Q^2 = 2\,\mathrm{GeV}^2$ and $0.2 < y < 0.7$, which still belong to the analysis phase space (Tab. 5.4), have scattered positron deflected to angles between 3° and 5°. When the condition on no scattered positron is applied, about around 70% of these events are vetoed, as it is shown in Fig. 5.11. The actual limit on Q^2 in untagged

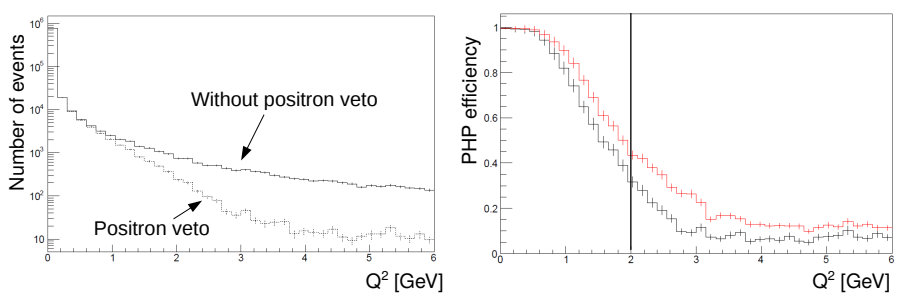

Fig. 5.11: The left plot shows the MC hadron-level spectrum of photon virtuality Q^2 without (solid line) and with (dashed line) positron veto. The fraction of non-vetoed Q^2 events (red curve in the right plot) is calculated as a ratio of the two Q^2 spectra showed on the left. If the cut on y is applied (black curve in the right plot), the fraction of removed high Q^2 events is around two times higher.

photoproduction is a matter of convention, the same phase space limit of $2\,\mathrm{GeV}^2$ was used e.g. in non-diffractive open charm photoproduction [111], whereas a little bit higher limit ($2.5\,\mathrm{GeV}^2$) was employed in [112].

The possible amount of DIS events admixture in the PHP selection is very low, also due to the fact of ten times lower DIS cross section than the PHP ones. If we

consider the fraction of non-vetoed ($\sim$10%) events presented in Fig. 5.11 we obtained DIS background $\sim$ 1%. Moreover, the additional requirement for the presence of jets improves y reconstruction and makes the fraction of this background even lower. Nevertheless, the migration from Q^2 up to 6 GeV^2 is taken into account in the unfolding procedure.

5.4.7 Selection of the DIS Events

For the selection of DIS events in this analysis, the positron candidate is required to be detected in the SpaCal. The energy E'_e and polar angle θ'_e of the scattered positron are determined from the SpaCal cluster and the interaction vertex reconstructed in the Central Tracking Detector, as described in section 5.4.3.

The DIS phase space described by quantities Q^2 and y is adjusted to cover the acceptance of SpaCal. The photon virtuality Q^2 between 4 GeV^2 and 80 GeV^2 roughly corresponds to the angular acceptance of this calorimeter. For example, the Fig. 5.11 indicates, that the SpaCal acceptance stabilizes just for Q^2 between 3 and 4 GeV^2, the upper limit of Q^2 is connected with the edge of LAr calorimeter. The inelasticity y is approximately proportional to the fraction of positron energy loss, thus the maximum allowed value of y determines the minimal allowed positron energy. Clusters with lower energy have worse energetic resolution and are more often misidentified as pion or photon. The minimal allowed inelasticity of 0.2 is fixed to be same as in the PHP analysis.

To be sure, that the whole cluster of the scattered positron is inside the SpaCal volume, the orthogonal distance of the cluster center to the beam is required to be within 14.5 cm and 74 cm[10] (see Tab. 5.8). Additionally the cluster radius r_{clus} is set to be less than 4 cm which reduces the background events where hadron is mistaken as positron, because the electromagnetic shower is typically narrower than the hadronic one. To select only clusters of good quality the cluster energy must be above $E'_e >$ 9.5 GeV. More detailed information about particle showers in SpaCal and definitions of cluster center and cluster radius is given in [113].

The quantity $\sum_i (E_i - P_{z,i})$ summed over all HFS particles and the scattered positron, is required to be in the range $35 - 75$ GeV. For fully reconstructed neutral current DIS events this quantity is expected to be twice the positron beam energy (55.2 GeV)[11] but is expected to be lower for photoproduction background where the scattered positron, which has sizable $E - P_z$ momentum, escapes undetected. Radiative events where a photon is emitted along the direction of the incident positron

[10] This distances are evaluated in plane $z = -160$ cm

[11] As a consequence of four-momentum conservation that implies conservation of so called light-cone variables [114] $E - P_z$ and $E + P_z$ before and after interaction. In diffraction $E - P_z$ of the incoming and scattered proton equals to 0. In photoproduction $E + P_z$ is equal to 0 for incoming and scattered positron.

$4 < Q^2 < 80\,\mathrm{GeV}^2$	Virtuality of photon exchange
$0.2 < y < 0.7$	Inelasticity
$r_{clus} < 4\,\mathrm{cm}$	Cluster radius
$E'_e > 9.5\,\mathrm{GeV}$	Cluster energy
$14.5 < R_{SpaCal} < 74\,\mathrm{cm}$	Cluster position
$35 < \sum_i (E_i - P_{z,i}) < 75\,\mathrm{GeV}$	Cut suppressing PHP background

Tab. 5.8: The DIS selection criteria at the detector level

beam, have also a reduced $\sum_i (E_i - P_{z,i})$. Applying all mentioned DIS selection criteria, the amount of the PHP background events fulfilling these cuts was found to be negligible.

5.5 Quality of the Detector Simulation and Variables Reconstruction

After applying all selection criteria, there were 3768 events in the PHP kinematic phase space and 550 events in the DIS phase space regime.

The detector level distributions of the measured variables are presented in Fig. 5.12 and Fig. 5.13 and are compared with the reweighted MC Rapgap simulation. A good description of the measured quantities by the simulation is the important prerequisite for the unfolding procedure, explained in next chapter.

To achieve the displayed agreement between the measured data and MC simulation, the simulated events were reweighted in variable z_{IP}^{HFS}, which was calculated for both PHP and DIS using formula (5.19). This reweighting increases the rate of jets in forward direction, which is apparently underestimated in unreweighted simulation. Worse description in high z_{IP}^{HFS} region can be partially caused by missing higher orders in Rapgap. Similar behaviour was observed in [70]. In addition, also the variable x_{IP}^{VFPS} was reweighted. Such a procedure, together with changing of the MC t-slope from $6\,\mathrm{GeV}^2$ to $5\,\mathrm{GeV}^2$, improved description of the VFPS variables.

The correlations plots which show the quality of the variables reconstruction by H1 detector and VFPS can be seen in Fig. 5.14 and Fig. 5.15. As an alternative also the differences between the reconstructed values and the true (=hadron level) values are presented in Fig. 5.16 and Fig. 5.17. In photoproduction the best resolution is observed for variables connected with jets pseudorapidities $\langle \eta^{jets} \rangle$ and $|\Delta\eta^{jets}|$. The resolution of the x_{IP} variable measured by means of VFPS, $\sigma_{x_{IP}} = 0.0022$, is the same as published in [3]. Low resolution is observed for $E_T^{*\mathrm{jet1}}$, moreover this resolution shown in Fig. 5.16 is asymmetric which is typical for steeply falling distributions. In DIS, the resolution of variable y is better than in photoproduction, because the scattered positron is directly measured.

We can conclude that the good agreement between data and reweighted MC RapGap distributions allows to advance to the unfolding procedure.

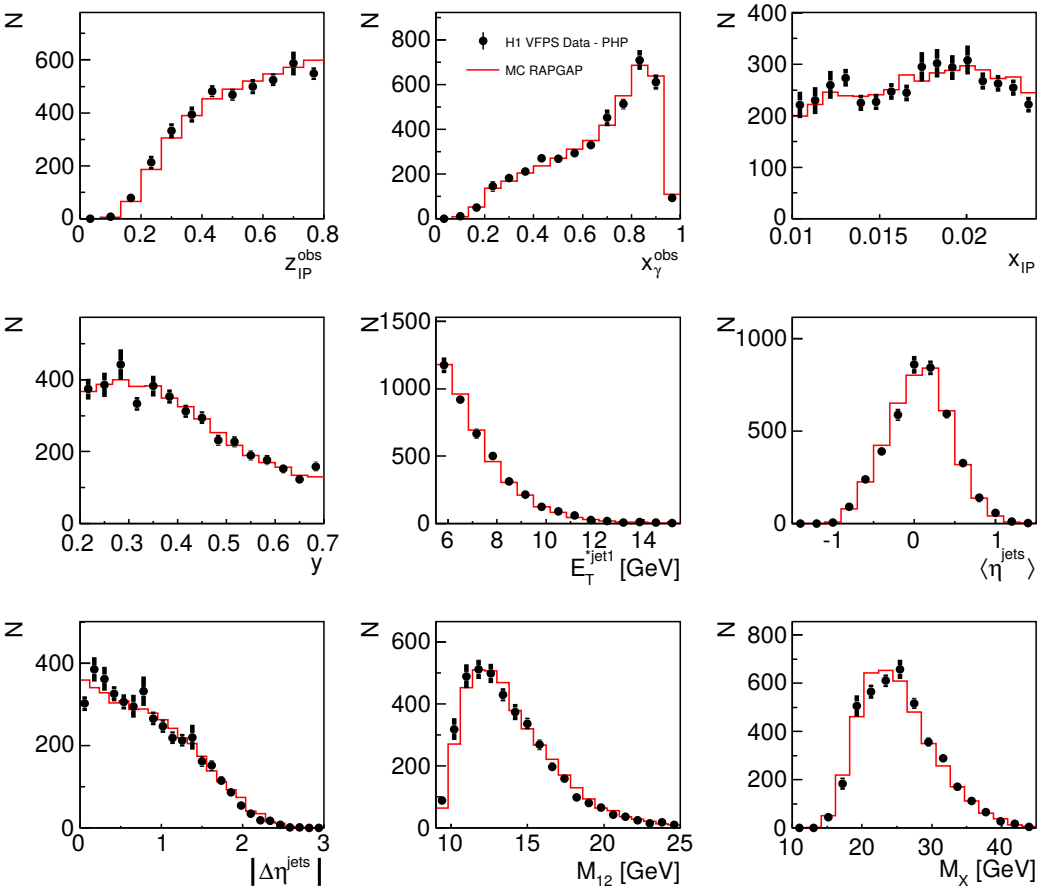

Fig. 5.12: Comparison of the MC simulation (red) to data (black) in the PHP regime for variables z_{IP}^{obs}, x_γ^{obs}, x_{IP}, y, $E_T^{*\mathrm{jet1}}$, $\langle\eta^{\mathrm{jets}}\rangle$, $|\Delta\eta^{\mathrm{jets}}|$, M_{12} and M_X.

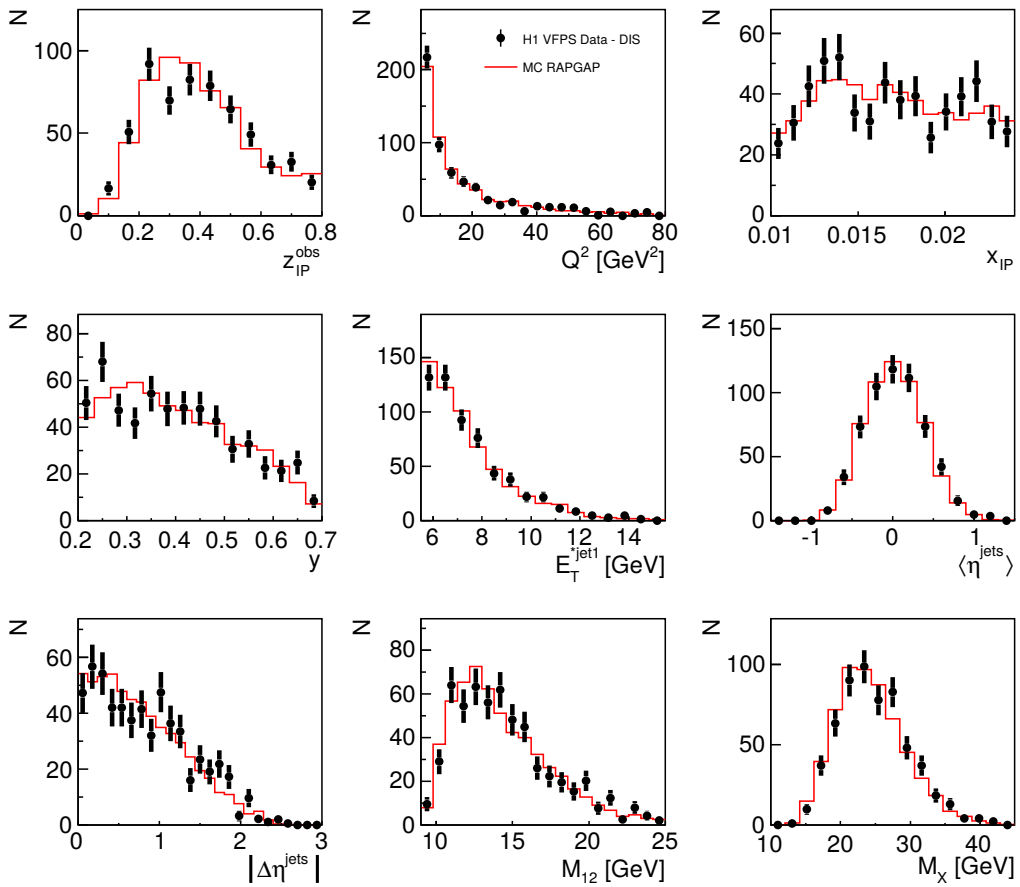

Fig. 5.13: Comparison of the MC simulation (red) to data (black) in the DIS regime for variables z_{IP}^{obs}, Q^2, x_{IP}, y, $E_T^{*\mathrm{jet1}}$, $\langle\eta^{\mathrm{jets}}\rangle$, $|\Delta\eta^{\mathrm{jets}}|$, M_{12} and M_X.

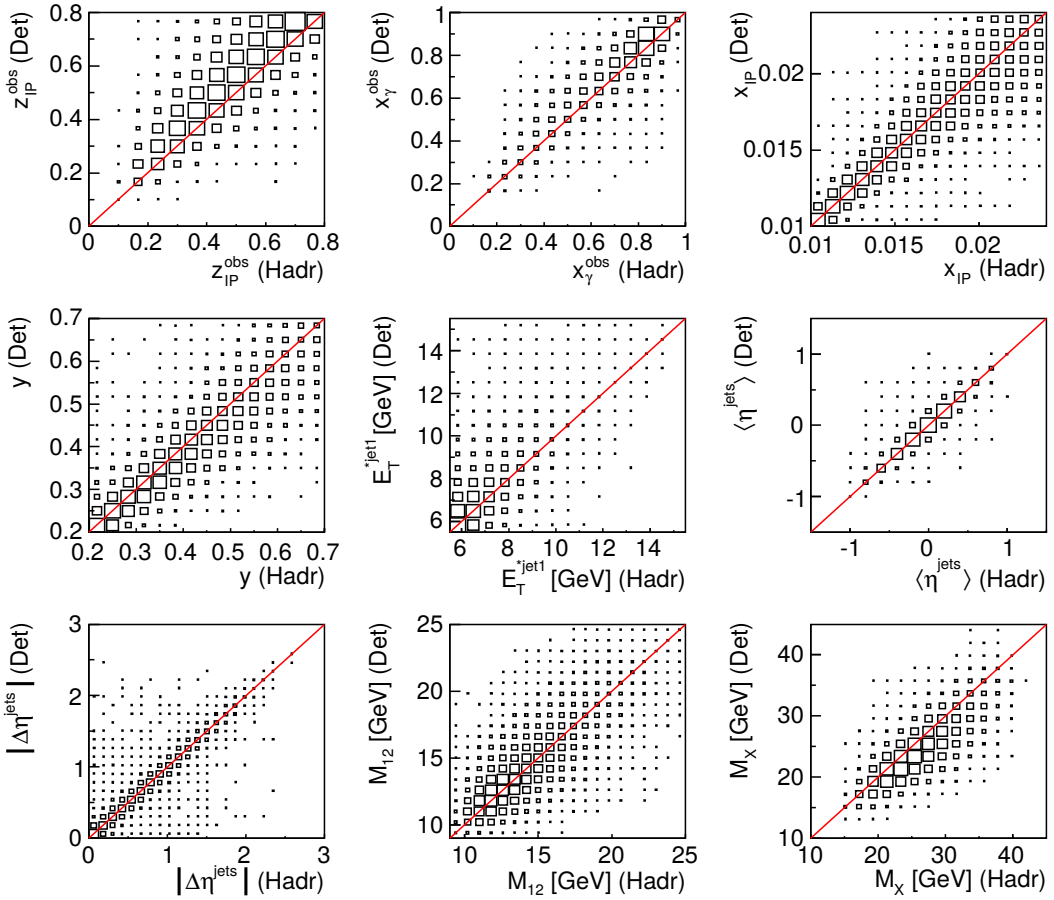

Fig. 5.14: The correlations between the hadron level and detector level variables in the PHP regime as estimated from the MC model. The event rate is proportional to the area of corresponding rectangle.

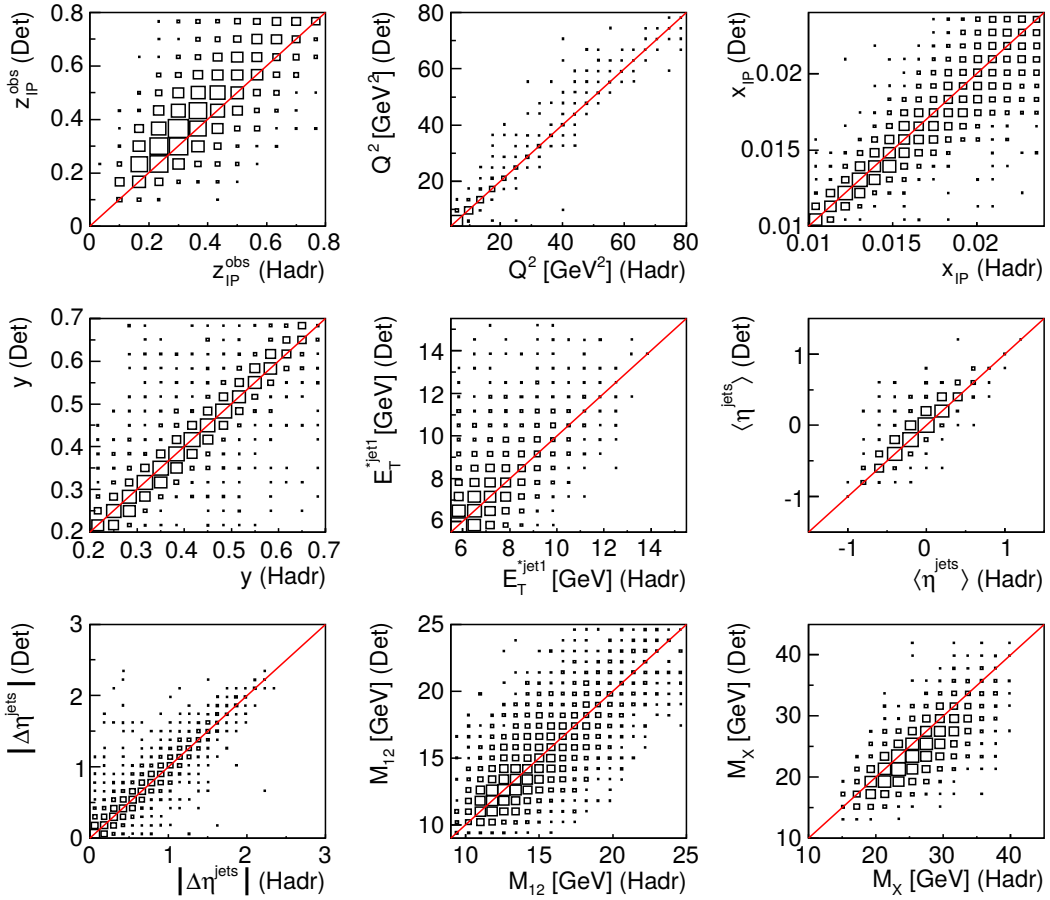

Fig. 5.15: The correlations between the hadron level and detector level variables in the DIS regime as estimated from the MC model. The event rate is proportional to the area of corresponding rectangle.

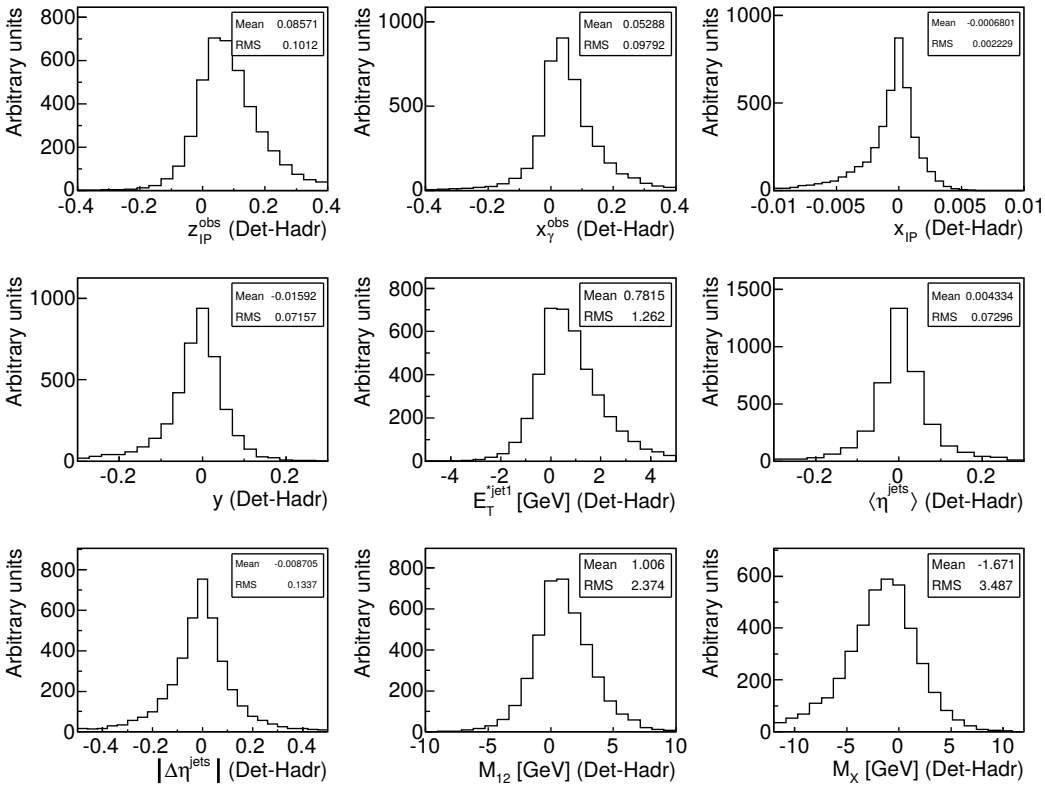

Fig. 5.16: The detection resolution in the PHP regime.

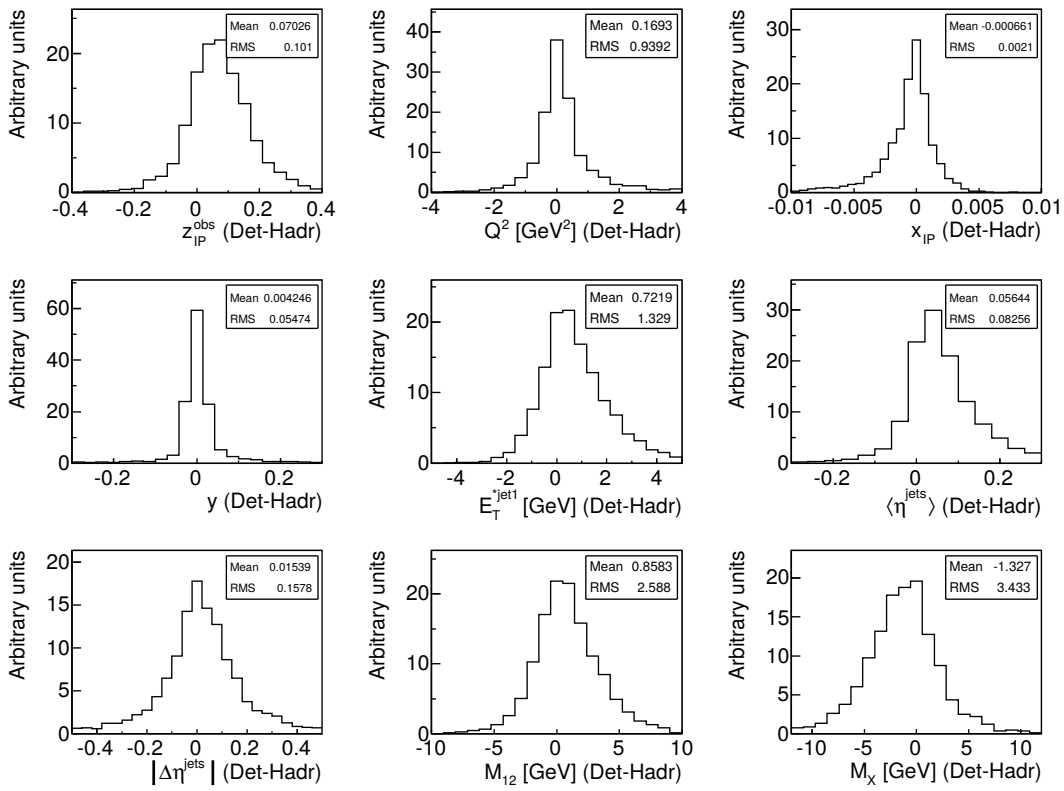

Fig. 5.17: The detection resolution in the DIS regime.

Chapter 6

Cross Section Measurement

6.1 Correction for the Detection Uncertainties

The measured event counts and consequently cross sections at the detector-level are affected by the detector acceptance, resolution and the data statistics. These effects smear the measured distributions and, therefore, can cause migrations into and out of the measured phase space. To study the cross section dependence on a given variable, the total cross section can be split into several pieces, called bins according to the value of this studied variable. The size of these bins depends not only on the data statistics but also on the detector resolution for the considered variable. The procedure which estimates the hadron-level cross sections, free of the detector effects, is known as unfolding.

6.1.1 Bin-By-Bin Unfolding Method

The simplest approach to estimate the hadron-level cross sections is so-called bin-by-bin method defined by formula:

$$\left(\frac{\mathrm{d}\sigma}{\mathrm{d}X}\right)_i = \frac{N_i^{data} - N_i^{bgr}}{\mathcal{L} A_i \Delta_{X_i}}(1 + \delta^i_{\mathrm{rad}}), \tag{6.1}$$

where N_i^{data} is the measured event count in bin i when the detector-level cuts are applied, N_i^{bgr} is excepted number of the background events in bin i which is typically estimated by the MC model, $\mathcal{L}$ stands for the integrated data luminosity and Δ_{X_i} for the bin width. The radiative corrections δ^i_{rad} which correct for the QED radiative effects will be explained in dedicated section 6.5.

The acceptance A_i is determined using the Monte Carlo generator by relation:

$$A_i = \frac{N^D(det\ i)}{N^H(had\ i)}, \tag{6.2}$$

where $N^H(had\ i)$ and $N^D(det\ i)$ are the event rates in bin i of the signal MC at the hadron-level and detector-level satisfying hadron-level phase space conditions (H) and the detector-level selection criteria (D), respectively. The binning is normally set to be equal on both detector- and hadron-level.

The trigger efficiency is assumed to be simulated by the MC model and therefore taken into account in the $N^D(det\ i)$ event rate. In principle, the acceptances A_i are allowed to be larger than one if the migrations into the detector-level bins are substantial.

The bin-by-bin method requires satisfactory description of the data control plots by MC model[1], not only in the measured phase space, but also in the neighboring regions to get hold on the migrations from outside. Even in this case, the obtained hadron-level data cross sections tend to be biased towards the used MC model if the events migrations between bins are considerable. The second condition is quantified by so-called purity P_i (sec. 6.1.2) which is recommended to be higher than 0.8 in each cross section bin to justify the applicability of the bin-by-bin method [115]. Otherwise, more sophisticated unfolding method needs to be utilized.

6.1.2 Purities and Stabilities

In order to describe the migrations between the bins, the purities P_i and stabilities S_i are introduced. They are calculated using the MC events rates as:

$$P_i = \frac{N^B(det\ i = had\ i)}{N^D(det\ i)} \qquad S_i = \frac{N^B(det\ i = had\ i)}{N^H(had\ i)}, \tag{6.3}$$

where $N^B(det\ i = had\ i)$ denotes the number of events complying simultaneously hadron- and detector-level selection cuts and are measured on both analysis levels in the same bin i of the inspected variable.

The purity is interpreted as the fraction of the detector-level events in bin i which passes hadron-level cuts and originates from the same bin i in the hadron-level. The stability stands for fraction of the hadron-level events in bin i which is reconstructed (passes detector-level cuts) and stays in the same bin i at the detector-level. Evidently, the acceptances (6.2) are related to purities and stabilities by the following formula:

$$A_i = \frac{S_i}{P_i}. \tag{6.4}$$

The purities, stabilities and acceptances for the PHP and DIS phase spaces are shown in Fig 6.1 and Fig 6.2. They are on average equal to 30 % for the PHP variables and 40 % for the DIS ones. Quite low purities are observed for E_T^{*jet1} and z_{IP}^{obs} variables which have poor resolution. In photoproduction also the x_γ^{obs} variable exhibits lower

[1] The control plots description usually has to be improved by the MC reweighting.

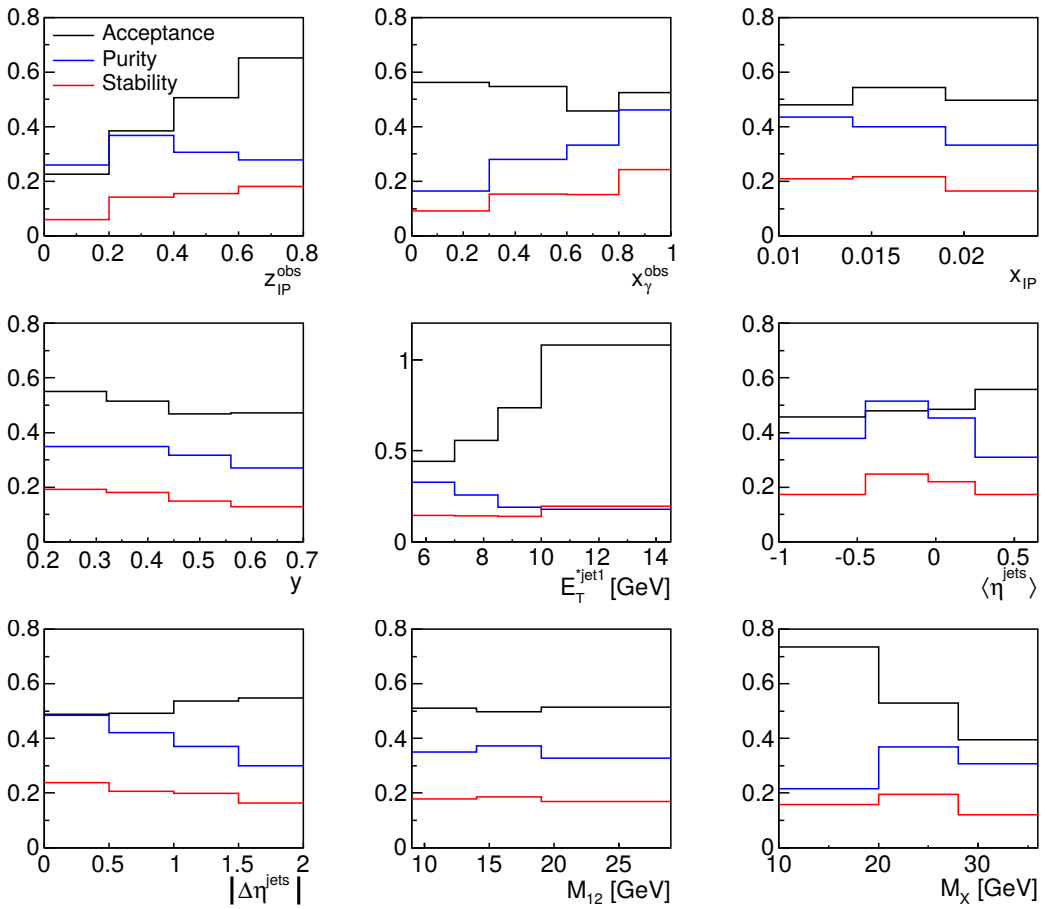

Fig. 6.1: The purities, stabilities and acceptances for variables z_{IP}^{obs}, x_{γ}^{obs}, y, $E_T^{*\mathrm{jet1}}$, $\langle\eta^{\mathrm{jet}}\rangle$, $|\Delta\eta^{\mathrm{jets}}|$, M_{12} and M_X as obtained by MC model RAPGAP for the photoproduction phase space.

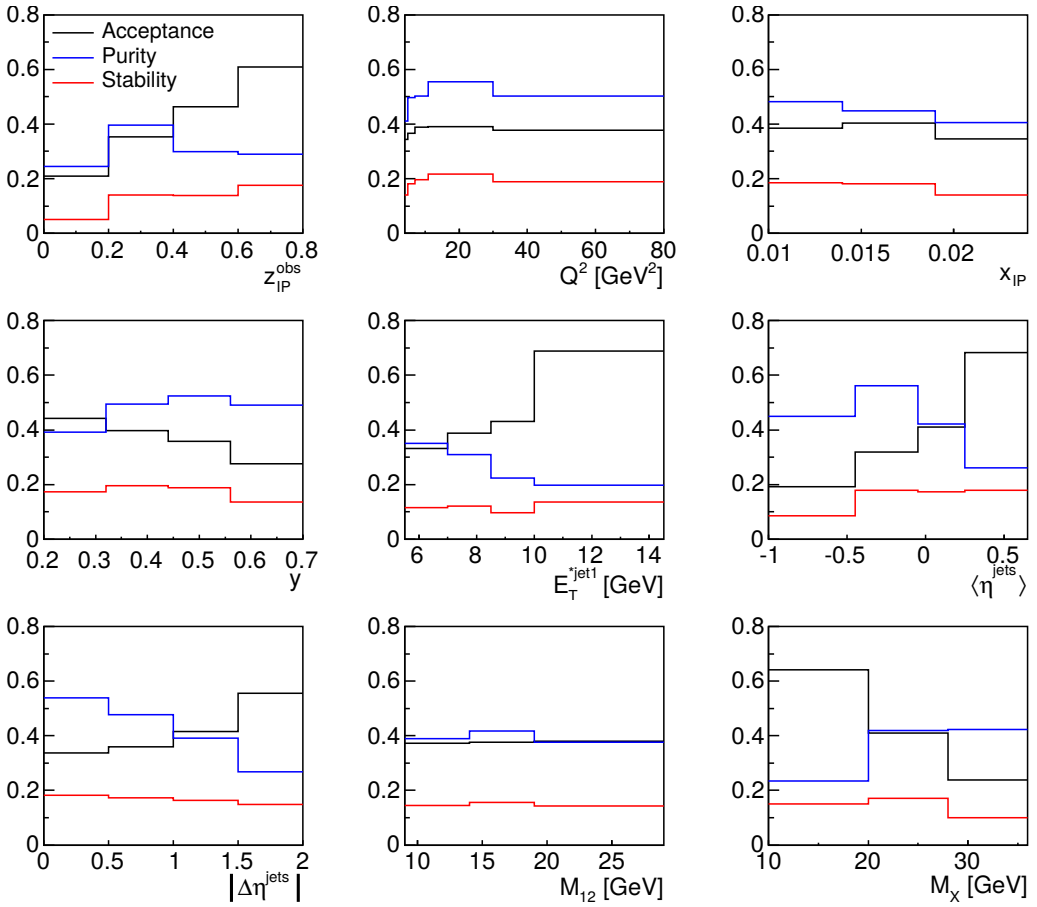

Fig. 6.2: The purities, stabilities and acceptances for variables z_{IP}^{obs}, Q^2, y, $E_T^{*\mathrm{jet1}}$, $\langle\eta^{\mathrm{jet}}\rangle$, $|\Delta\eta^{\mathrm{jets}}|$, M_{12} and M_X as obtained by MC model RAPGAP for the DIS phase space.

purities as a consequence of migrations from the direct photon interactions ($x_\gamma \sim 1$) towards lower values at the detector-level. On the contrary, higher purities are observed for $\langle\eta^{\text{jet}}\rangle$, $|\Delta\eta^{\text{jets}}|$ and x_{IP} distributions for PHP and DIS and for y and Q^2 for DIS which are measured with good resolution.

The total[2] purity for the PHP and DIS analysis is 47% and 55%, respectively. The better purity of the DIS measurement is a consequence of direct measurement of the positron kinematics in SPACAL, which results in better resolution in y and z_{IP}^{obs} and hence lowers migrations.

The purities for both kinematic regions are lower than 80% which makes usage of simple bin-by-bin method described in the previous section questionable.

6.1.3 Regularized Unfolding

Due to the considerable migration of events which was demonstrated in the previous section, the unfolding algorithm based on the Tikhonov regularisation [116] is employed. Similar procedure was used also in recent H1 papers [86, 87] about the diffractive production of dijets in the DIS region. All previous diffractive dijets analyses reviewed in Tab. 4.2 and Tab 4.5, namely all measurements of the diffractive photoproduction of dijets, use classical bin-by-bin unfolding method.

The smearing and acceptance effects of the detection can be described in more detailed way by the matrix A_{ij} which contains probabilities, that event in bin j at the hadron-level will be reconstructed in bin i at the detector-level. Using this definition of the matrix of probabilities, the vector of the measured cross sections $\tilde{y}_i$ takes the form:

$$\tilde{y}_i = \sum_{j=1}^{M} A_{ij}\tilde{x}_j \qquad i = 1 \ldots N, \tag{6.5}$$

where $\tilde{x}_j$ denotes the vector of the hadron-level ("true") cross sections. The A_{ij} is usually estimated by the MC model, in this analysis by the Rapgap MC generator interfaced to the H1 and VFPS detector simulation. In reality, the measured cross sections are affected also by the statistical fluctuations, so the data vector $\mathbf{y}$ is a random variable as is illustrated in Fig. 6.3.

Note that in contrast to the bin-by-bin method the numbers of the hadron-level and detector-level bins M and N are not necessary equal, in reality the choice which shows to be most stable for unfolding based on the Tikhonov regularisation is to have twice more detector-level bins N compared to the hadron-level bins M [117]. In this case, the system of equations (6.5) is overdetermined and almost always has no exact solution $\tilde{x}_j$ in the mathematical sense.

[2] Calculated for a single bin incorporating whole measured phase space

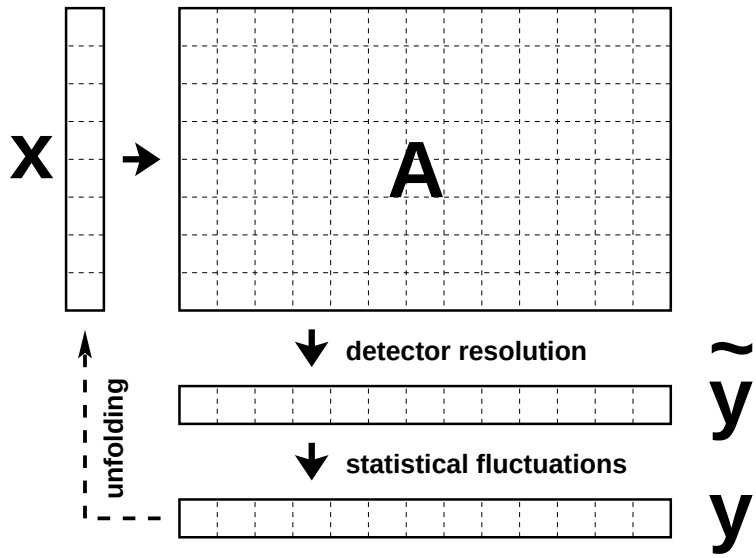

Fig. 6.3: The schematic explanation of the relation between the true cross sections given in vector x and the measured cross sections y [117].

The χ^2 variable which is the measure of agreement between the measured data and the excepted values $\mathbf{Ax}$ can be expressed by relation:

$$\chi^2_{data} = (\mathbf{y} - \mathbf{Ax})^T \mathbf{V}_{yy}^{-1} (\mathbf{y} - \mathbf{Ax}), \tag{6.6}$$

where the data covariance matrix is denoted as $\mathbf{V}_{yy}$ and contains the squares of the data statistical errors at the diagonal if the measured data are supposed to be uncorrelated between bins at the detector-level. It is natural, to find the unknown vector of the true cross sections $\mathbf{x}$ by minimising this χ^2_{data} function with respect to this vector[3]

$$\frac{\mathrm{d}\chi^2_{data}}{\mathrm{d}x_j} = 0, \qquad j = 1 \ldots M. \tag{6.7}$$

However the vector x obtained in this way may exhibit large unphysical oscillations as was shown in [118, 119]. To solve this issue an additional regularisation term χ^2_r of form [116]:

$$\chi^2_r = \tau^2 (\mathbf{x} - \mathbf{x_0})^T \mathbf{L}^T \mathbf{L} (\mathbf{x} - \mathbf{x_0}), \tag{6.8}$$

is added to the χ^2_{data}, where $\mathbf{L}$ is the regularisation matrix, $\mathbf{x_0}$ denotes the data bias and the strength of the regularisation is determined by parameter τ. The resulting

[3] Method of least squares

data cross sections x_j at the hadron-level are then given by the set of linear equations:

$$\frac{\mathrm{d}\chi^2}{\mathrm{d}x_j} = \frac{\mathrm{d}}{\mathrm{d}x_j}(\chi^2_{data} + \chi^2_r) = 0 \qquad j = 1 \dots M. \tag{6.9}$$

Solving these equations leads to result:

$$\mathbf{x} = \mathbf{E}\left(\mathbf{A}^T\mathbf{V}^{-1}_{\mathbf{yy}}\mathbf{y} + \tau^2\mathbf{L}^T\mathbf{L}\,\mathbf{x_0}\right) \qquad \mathbf{V_{xx}} = \mathbf{D^{xy}}\mathbf{V_{yy}}(\mathbf{D^{xy}})^T, \tag{6.10}$$

where the standard rule of error propagation was applied to estimate the hadron-level covariance matrix $\mathbf{V_{xx}}$ and the auxiliary matrices $\mathbf{E}$ and $\mathbf{D^{xy}}$ take form:

$$\mathbf{E} = (\mathbf{A}^T\mathbf{V}^{-1}_{yy}\mathbf{A} + \tau^2\mathbf{L}^T\mathbf{L})^{-1} \qquad \mathbf{D^{xy}} = \mathbf{E}\mathbf{A}^T\mathbf{V}^{-1}_{\mathbf{yy}}. \tag{6.11}$$

If the input detector-level data vector $\mathbf{y}$ represents the events counts then the final differential cross sections are obtained as:

$$\left(\frac{\mathrm{d}\sigma}{\mathrm{d}X}\right)_i = \frac{x_i}{\mathcal{L}\Delta_{X_i}}(1 + \delta^i_{\mathrm{rad}}). \tag{6.12}$$

The regularisation matrix $\mathbf{L}$ can be chosen in several ways as discussed in [117]. The simplest possibility is to set $\mathbf{L}$ to be equal to the unity matrix which is referred as a regularisation on the size, because the χ^2_r is reduced to $\tau^2|\mathbf{x}-\mathbf{x_0}|^2$ in this case. Another possibility is to regularise on the first or second derivatives of $\mathbf{x}$ which corresponds to the $\mathbf{L}$ matrix of the form of discrete differential operator. In this thesis, due to the quite small number of bins of the measured distributions, the regularisation on the size is applied.

The crucial aspect of any regularisation technique is the right choice of the regularisation strength which is determined by the regularisation parameter τ. When the parameter τ is too small, the result of unfolding tends to have large unphysical fluctuations between the measured bins. On the contrary, if τ is too large, the resulting cross sections $\mathbf{x}$ are biased toward $\mathbf{x_0}$.

The L-curve method [120] used in this thesis assumes that the best value of τ corresponds to the point in the parametric plot of (L_x, L_y) with the highest curvature. The coordinates of such plot are calculated by equations

$$L_x(\tau) = \log \chi^2_{data}[\mathbf{x} = \mathbf{x}^{min}(\tau)] \qquad L_y(\tau) = \log \frac{\chi^2_r[\mathbf{x} = \mathbf{x}^{min}(\tau)]}{\tau^2}, \tag{6.13}$$

where the vector $\mathbf{x}$ in equations (6.6) and (6.8) is set to the value (6.10) which is a function of the regularisation parameter τ.

6.2 Structure of the migration matrix

The migration matrix **A** introduced in the previous section is used not only to describe migration within the analysis phase space, but also to quantify migrations from the neighboring parts. For this purpose several phase spaces surrounding the analysis phase space were introduced (Tab. 6.1).

The kinematic restriction of these spaces was selected to control event migration into the measured analysis phase space from the neighboring regions. These migrations are typically large for steeply falling distributions with poor resolution, like transverse jet energy. In this case, the frequent events with transverse energy below the analysis threshold often migrate towards higher values, i.e. into the analysis phase space. The effort to control as much of these off phase space migrations as possible typically collides with the detector and simulation performance in these regions. For example, the ability to measure low transverse energy jet is limited as well as detection of high x_{IP} events by the VFPS detector. The definitions of phase spaces in Tab. 6.1 represent a trade-off between these two effects.

The Fig. 6.4 shows that about 80% of PHP events and 83% of DIS events originate from phase spaces defined in Tab. 6.1.

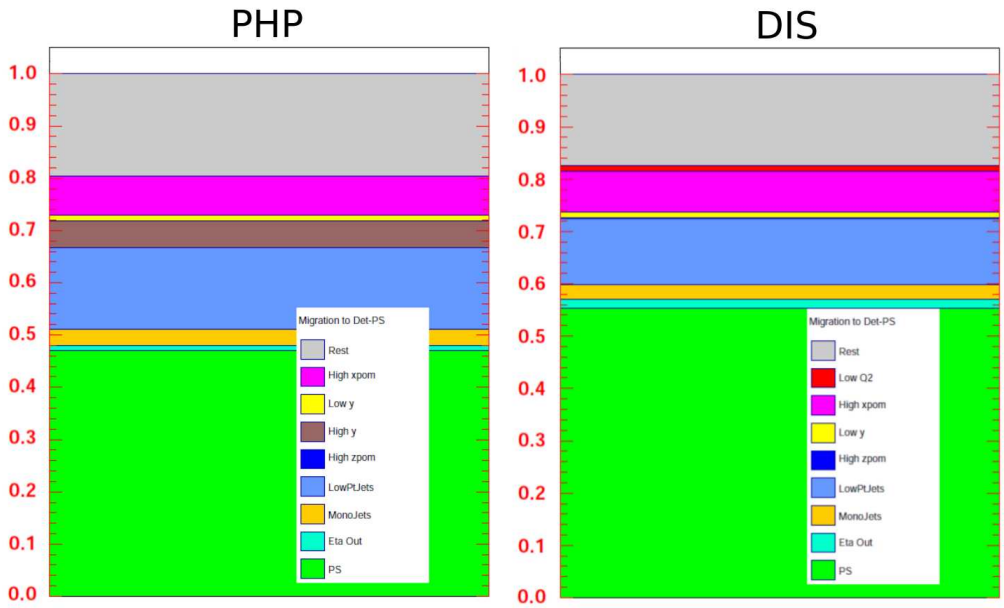

Fig. 6.4: The impurity sources for the PHP (left) and the DIS (right) analysis. These plots show from where the events fulfilling the detector-level cuts come from, especially the green area represents classical purity defined by (6.3). The vertical axis denotes the fraction of the total event count.

Phase space name	PHP	DIS
Analysis PS	$E_T^{*\mathrm{jet1}} > 5.5$ $E_T^{*\mathrm{jet2}} > 4.0$ $-1 < \eta^{\mathrm{jet1,2}} < 2.5$ $0.2 < y < 0.7$ $Q^2 < 2$ $z_{IP}^{obs} < 0.8$ $0.10 < x_{IP} < 0.24$ $\lvert t \rvert < 0.6$	$E_T^{*\mathrm{jet1}} > 5.5$ $E_T^{*\mathrm{jet2}} < 4.0$ $-1 < \eta^{\mathrm{jet1,2}} < 2.5$ $0.2 < y < 0.7$ $4 < Q^2 < 80$ $z_{IP}^{obs} < 0.8$ $0.10 < x_{IP} < 0.24$ $\lvert t \rvert < 0.6$
LowPt Jets	$3.2 < E_T^{*\mathrm{jet1}} < 5.5$ $3.2 < E_T^{*\mathrm{jet2}}$	$3.2 < E_T^{*\mathrm{jet1}} < 5.5$ $3.2 < E_T^{*\mathrm{jet2}}$
Mono Jets	$3.2 < E_T^{*\mathrm{jet2}} < 4$	$3.2 < E_T^{*\mathrm{jet2}} < 4$
EtaOut Jets	$\eta^{\mathrm{jet1}} < -1 \,\lvert\lvert\, \eta^{\mathrm{jet2}} < -1$	$\eta^{\mathrm{jet1}} < -1 \,\lvert\lvert\, \eta^{\mathrm{jet2}} < -1$
Low y	$5.0 < E_T^{*\mathrm{jet1}}$ $3.8 < E_T^{*\mathrm{jet2}}$ $y < 0.2$	$5.0 < E_T^{*\mathrm{jet1}}$ $3.8 < E_T^{*\mathrm{jet2}}$ $y < 0.2$
High y	$4.0 < E_T^{*\mathrm{jet1}}$ $3.2 < E_T^{*\mathrm{jet2}}$ $0.7 < y$	-
Low Q2	-	$4.0 < E_T^{*\mathrm{jet1}}$ $3.2 < E_T^{*\mathrm{jet2}}$ $3 < Q^2 < 4$
High zpom	$4.0 < E_T^{*\mathrm{jet1}}$ $3.2 < E_T^{*\mathrm{jet2}}$ $0.8 < z_{IP}^{obs}$	$4.0 < E_T^{*\mathrm{jet1}}$ $3.2 < E_T^{*\mathrm{jet2}}$ $0.8 < z_{IP}^{obs}$
High xpom	$4.0 < E_T^{*\mathrm{jet1}}$ $3.2 < E_T^{*\mathrm{jet2}}$ $0.24 < x_{IP} < 0.28$	$4.0 < E_T^{*\mathrm{jet1}}$ $3.2 < E_T^{*\mathrm{jet2}}$ $0.24 < x_{IP} < 0.28$

Tab. 6.1: The overview of the phase spaces definitions used in the unfolding procedure to control off analysis phase space (PS) migrations. For the analysis PS the complete definition of cuts is given whereas for the extended phase spaces only the unequal conditions are presented. For simplicity the units of GeV or GeV^2 are omitted.

In addition to the binning of the measured variable in the analysis phase space, also the binning of auxiliary phase spaces (Tab. 6.1) has to be specified. For the measured variable, the bins widths have to be sufficiently large to suppress statistical fluctuations and migrations from the adjacent bins due to the detector smearing, on the other hand their size must be small enough to provide valuable physical information about the shape of studied differential distributions. The number of bins in the neighboring phase-spaces is chosen in correspondence with the data statistics, because the TUnfold unfolding package [117] which implements the regularised unfolding described in section 6.1.3 performs best if the event counts in the detector-level bins are comparable.

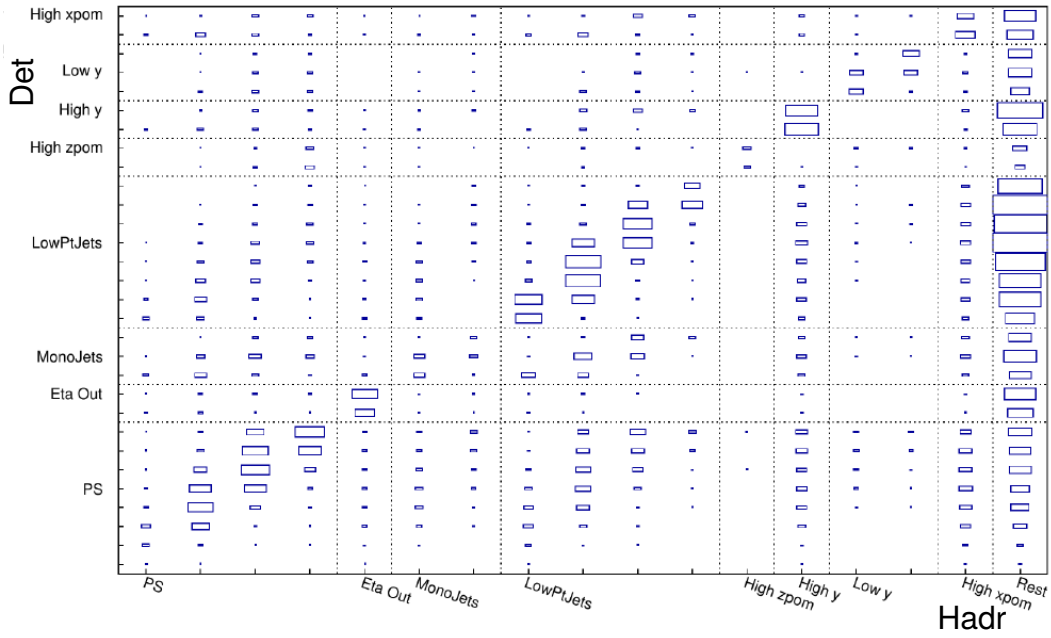

Fig. 6.5: The migration matrix for variable z_{IP}^{obs} in the PHP region. The area of rectangles inside the plot is proportional to the rate of events which fulfil corresponding hadron-level and detector-level selection. The last column called "Rest" includes events which are off any hadron-level phase spaces quoted in Tab. 6.1.

6.3 Systematic Uncertainties

The systematic uncertainties can be divided into two categories. The first group of uncertainties is a consequence of imperfect knowledge of the detector which means that the detector simulation does not perfectly correspond to the real detector. The

second group originates from imperfect knowledge of the hadron-level[4] spectra which can result in the process of unfolding to some bias of the data toward used MC model. Both uncertainty classes are considered by means of variation of the migration matrix which is affected by both the detector simulation and the hadron-level MC model.

Each systematic source is typically classified by two systematic shifts, which represent variation of the imprecisely known detector simulation or MC-model parameter in both directions from the central value. For every systematic shift a separate migration matrix is filled and the difference $\partial\mathbf{A}$ to the nominal migration matrix $\mathbf{A}$ is propagated through the unfolding procedure which results in the shift $\partial\mathbf{x}$ of the hadron-level cross section vector $\mathbf{x}$ [117]:

$$\partial\mathbf{x} = \mathbf{E}(\partial\mathbf{A})^T\mathbf{V}_{\mathbf{yy}}^{-1}(\mathbf{y} - \mathbf{A}\mathbf{x}) - \mathbf{D}^{\mathbf{xy}}(\partial\mathbf{A})\mathbf{x}, \tag{6.14}$$

where all quantities in this equation were introduced in section 6.1.3. The corresponding contribution to the covariance matrix $\mathbf{V}_{\mathbf{xx}}^{\partial\mathbf{A}}$ is given as:

$$\mathbf{V}_{\mathbf{xx}}^{\partial\mathbf{A}} = \partial\mathbf{x}(\partial\mathbf{x})^T \tag{6.15}$$

In the end all the contributions are added in quadrature for each bin to obtain the total systematic uncertainty.

6.3.1 Detector Systematic Uncertainties

Several sources of the detection uncertainties are considered:

VFPS calibration: The primary source of VFPS systematic uncertainties is related to an uncertainty of the x and y global track coordinates, defined by formulas (5.1), with respect to the beam. The actual beam position is measured with help of a beam position monitor [3, 121] which has a precision of 160 μm in x and 120 μm in y. The horizontal coordinate x has an additional uncertainty stemming from the VFPS calibration procedure, tied to the reconstruction of x_{IP} in the main H1 detector. The resulting x-coordinate uncertainty is 250 μm, where both mentioned x-coordinate systematic errors were added in quadrature. The uncertainty in the y-coordinate is totally determined by the precision of the BPM_y.

The size of the beam x- and y-tilt uncertainties is related to the stability of the beam over time. The obtained uncertainties are 8 μrad for the x-tilt and 6 μrad for the y-tilt.

In the end the VFPS global track properties x, y, x' and y' which represent the input parameters to the neural network (5.4) are shifted up and down for each MC event with the given amplitudes.

[4] Otherwise no measurement is needed.

The beam aperture limitation restricts the VFPS acceptance and introduces an additional uncertainty in the θ_X reconstruction [3].

In total, all sources of VFPS uncertainties affect the integrated cross section by 5.5% for photoproduction and 3.7% for DIS.

Positron reconstruction: In DIS analysis the uncertainties of the measured positron energy E'_e (1%) and angle θ'_e (1 mrad) [122] in the SpaCal calorimeter lead to an uncertainty of the total cross section of 0.4% and 0.7%, respectively.

Energy scale: The HFS energy scale is fixed with the help of the iterative calibration method which uses the transverse momentum balance p_T^{bal} to determine the calibration constant. The balance p_T^{bal} represents the ratio of transverse momenta of the scattered lepton and the hadronic final state:

$$p_T^{bal} = \frac{p_T^{HFS}}{p_T^e}. \tag{6.16}$$

Ideally this ratio should be 1 according to the transverse momenta conservation law. In reality due to the LAr calorimeter resolution of $50\%/\sqrt{E/\mathrm{GeV}} \oplus 2\%$ this ratio is smeared on the event by event basis (see middle row of Fig. 6.6)[5]. The mean values as well as relative standard deviation of the Gaussian fitted to the p_T^{bal} distribution for data and MC are plotted in Fig. 6.6. The p_T^{bal} ratio is described by the MC simulation within 2% in the studied kinematic region of scattered electron transverse energy $P_{T,e}$, virtuality Q_e^2 and inelasticity y_e as is demonstrated in the double ratio plot in the bottom row of Fig. 6.6.

Therefore, the absolute energy calibration of the HFS is known with 2% precision [123]. The same factor was found in [124], where the presence of one jet with transverse momenta above 3 GeV was required. Due to poor data statistic of the DDIS dijet analysis, no attempt was done to check this resolution factor in the DIS analysis phase space.

The variation of the HFS object energies by ±2% leads to the total cross section uncertainty of ±7.6% for photoproduction and ±6.1% for DIS.

Normalisation uncertainties: Several sources of normalisation systematic errors are considered:

- The VFPS track reconstruction efficiency is known to within 2.5% [3].
- The VFPS background originating from interaction of the beam particle with the residual gas, producing a proton signal in the VFPS in an accidental coincidence with a dijet event in the main H1 detector is less than 1% and is treated as a normalisation uncertainty [3].

[5] The resolution of the transverse momentum measurement of the scattered lepton in SpaCal is much better.

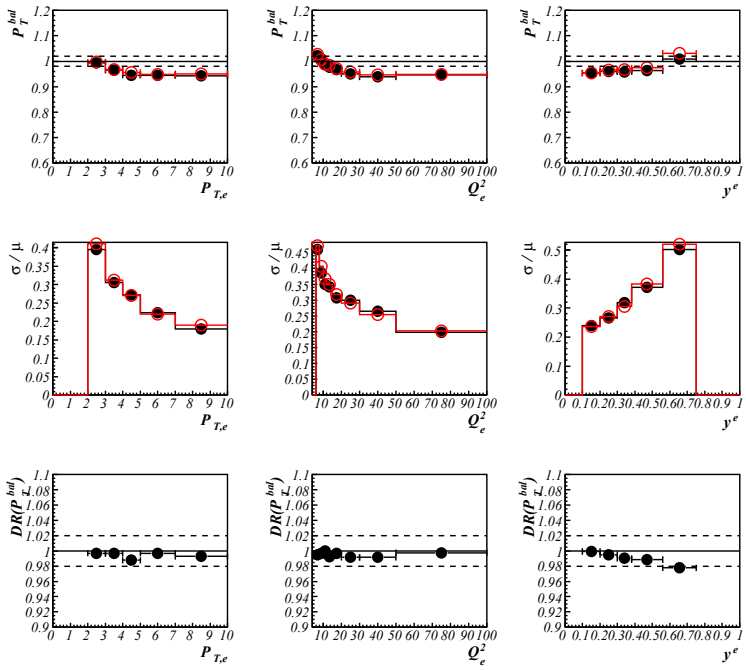

Fig. 6.6: The p_T^{bal}, top, the relative standard deviation $\frac{\sigma}{\mu}$ in data (black) and MC (red), middle, and the double ratio of data to MC of p_T^{bal} [123], bottom. The 2% error band for ratios is depicted by the dashed line.

- The integrated luminosity of the VFPS triggered data is known to 3% [125].
- The trigger efficiency has an uncertainty of 5%.

The resulting total normalisation uncertainty amounts to 6%.

6.3.2 Model Systematic Uncertainties

The measured hadron-level cross sections are also affected by the MC model which was used for the unfolding. These effects could be studied ideally by using several MC generators, differing for example in the hadronization model.

Unfortunately, at the present, the only usable MC generator Rapgap [59] for the measured processes exists. This MC generator uses Lund String Fragmentation model as implemented in Pythia 6 [126]. The possible alternative MC generator Pomwig [63] which is based on Herwig [62] and employs Cluster fragmentation model is currently not interfaced to the H1 detector simulation framework. The hadronization model has particularly substantial influence on the rapidity gap spectra as was shown in [127] and therefore can affect the size of the cross section obtained by the LRG

method. For the leading proton diffractive selection used in this analysis much smaller hadronization model dependency is excepted.

To mimic another MC model, the hadron-level spectra are varied in several variables in such way that the shifted control plots spectra are still consistent with the data within the data statistical uncertainties. Note that the unfolded data cross sections do not depend on the absolute normalisation of the MC model used for the unfolding, what matters is the shape of the distributions. All model systematic shifts together with the resulting uncertainty of the integrated cross section are summarised in Tab. 6.2, for simplicity the same variations were imposed for both the photoproduction and the DIS region.

Variable	Model weight	PHP	DIS
$E_T^{*\mathrm{jet1}}$	$(E_T^{*\mathrm{jet1}})^{\pm 0.4}$	3.5%	3.0%
x_{IP}	$x_{IP}^{\pm 0.2}$	0.7%	0.4%
z_{IP}^{obs}	$z_{IP}^{obs\pm 0.3}$	3.1%	1.7%
x_γ^{obs}	$x_\gamma^{obs\pm 0.3}$	2.7%	1.1%
y	$y^{\pm 0.3}$	0.4%	0.4%
t	$e^{\pm t}$	4.5%	3.3%
Q^2	$(Q^2+0.1)^{\pm 0.2}$	1.0%	0.5%

Tab. 6.2: Overview of the model systematic shifts and their effect to the uncertainty of the PHP and DIS integrated cross section. The variable $E_T^{*\mathrm{jet1}}$ is in GeV and t and Q^2 in GeV^2.

The effect of these variations on the detector-level spectra is demonstrated in Fig. 6.7 and Fig. 6.8. The orange band represents all model systematic shifts deviations added in quadrature. The width of such a band Δ_i for the given bin i takes the form:

$$\Delta_i = \sqrt{\frac{1}{2}\sum_k \left[N_k(det\ i) - N(det\ i)\right]^2}, \tag{6.17}$$

where index k runs over all 14 systematic shifts defined in Tab. 6.2. The nominal and shifted MC event count normalised to the data is denoted as $N(det\ i)$ and $N_k(det\ i)$, respectively. The up and down model systematics shifts are averaged by the factor of $\frac{1}{2}$.

The exponential slope of the t distribution which is not shown is varied by factor ± 1 which is the uncertainty of this parameter used in H1 2006 Fit B DPDF [4, 128].

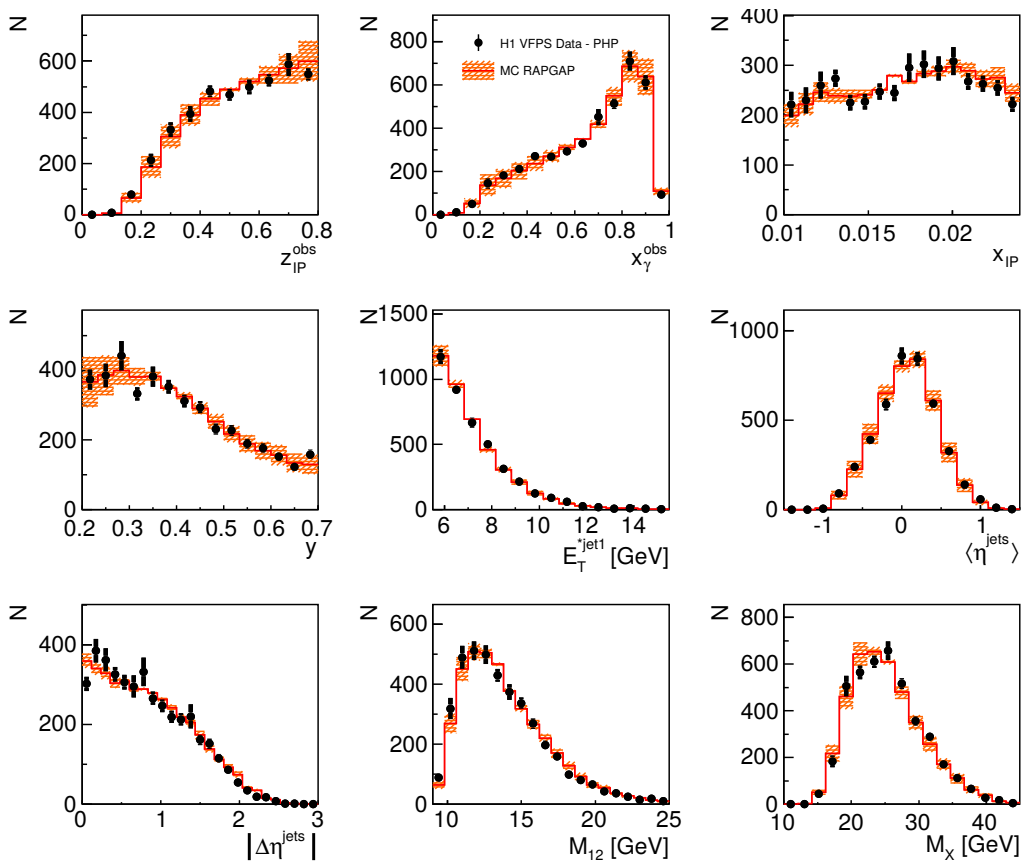

Fig. 6.7: The detector-level control plots in the PHP kinematic region. The black data points are compared to the reweighted MC model RAPGAP which is represented by the red line. The orange band depicts the deviation in quadrature between all model shifts.

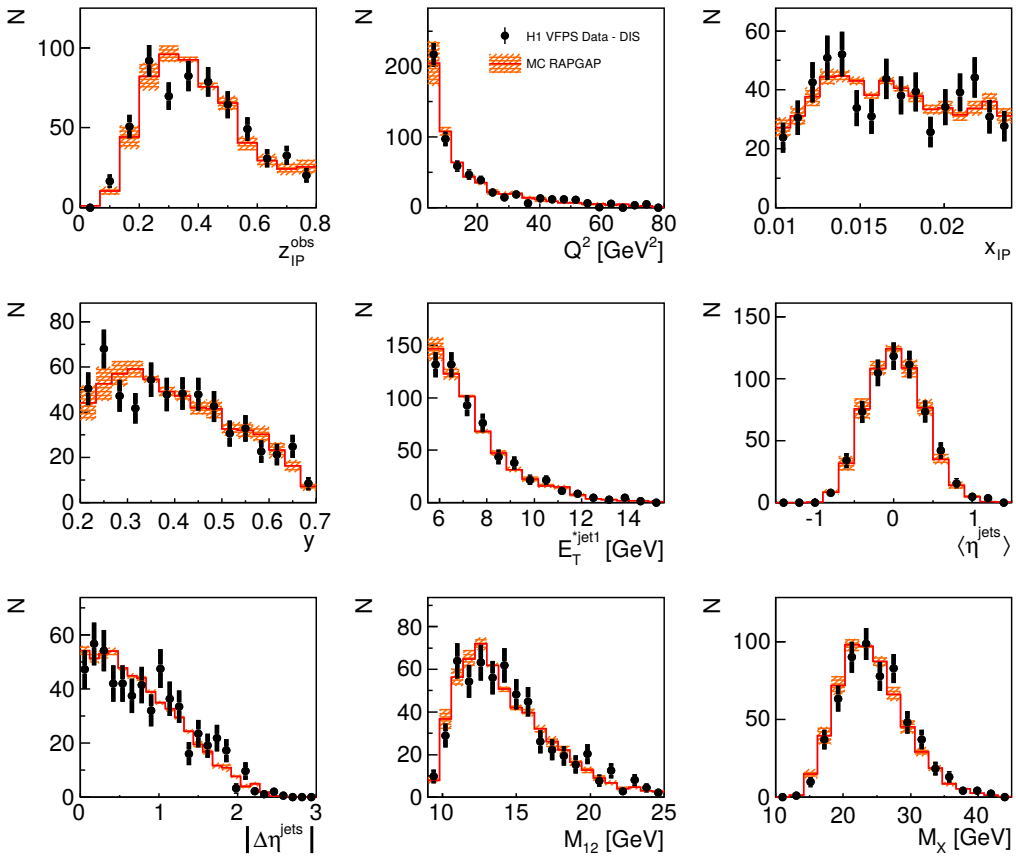

Fig. 6.8: The detector-level control plots in the DIS kinematic region. The black data points are compared to the reweighted MC model Rapgap which is represented by the red line. The orange band depicts the deviation in quadrature between all model shifts.

6.4 Hadronization Corrections

The NLO QCD predictions of DIS and PHP cross sections are calculated at the level of partons. In order to compare them to the measured cross sections, they must be corrected for non-perturbative hadronization effects.

The hadronization corrections factors are estimated by the LO Monte Carlo generator RAPGAP as

$$1 + \delta^i_{\text{hadr}} = \frac{\sigma^{\text{hadr}}_i(nrad)}{\sigma^{\text{part}}_i}, \tag{6.18}$$

where the $\sigma^{\text{hadr}}_i(nrad)$ (σ^{part}_i) are the bin-integrated MC cross sections at hadron level (parton level) in a given bin i. The QED radiation at the hadron level is switched off, therefore the hadronisation corrections correct the NLO cross sections for the hadronization effects only. The parton level RAPGAP differential cross sections resemble the NLO distributions quite satisfactory in shape because the partonic showers mimic to some extent the higher order effects (Fig. 6.9 and 6.10). To make this agreement even better, the MC sample is reweighted in the z^{obs}_{IP} variable. The corrections factors δ^i_{hadr} are then expected to be more realistic.

The hadronization corrections reduce the predicted NLO parton level integrated cross section by $\sim 9\%$ in photoproduction and enhance the integrated cross section by $\sim 2\%$ in the DIS. The negative sign of corrections δ^i_{hadr} in the photoproduction region is caused by a contribution of resolved photon processes.

The hadronisation corrections $1 + \delta^i_{\text{hadr}}$ for the measured variables in photoproduction and DIS are shown in Fig. 6.11 and 6.12. The hadronization correction factor is particularly large at the second highest x^{obs}_γ bin for PHP (Fig. 6.11), where the contributions with $x^{obs}_\gamma \sim 1$ at the parton level migrate towards lower values due to the hadronization effect.

Uncertainties in the hadronization corrections are supposed to be comparable to [17], where an alternative MC generator Pomwig [63] was used. Differences between Lund string model and Cluster model hadronization corrections were in average 3%.

6.5 Radiative Corrections

The initial and final state QED radiation from positron, as well as, virtual corrections rising from the $e\gamma e'$ vertex correction and exchanged photon self-energy are taken into account. All these $O(\alpha_{em})$ corrections are evaluated by means of HERACLES [64] which is interfaced to the RAPGAP MC generator. Since data and the theoretical predictions must be compared at the same physical level, two possibilities exist, either to incorporate the QED radiation effects into the theoretical NLO predictions at the hadron level or to "subtract" the QED radiation from the data. The second possibility is standardly employed by the H1 collaboration, therefore the data and NLO QCD

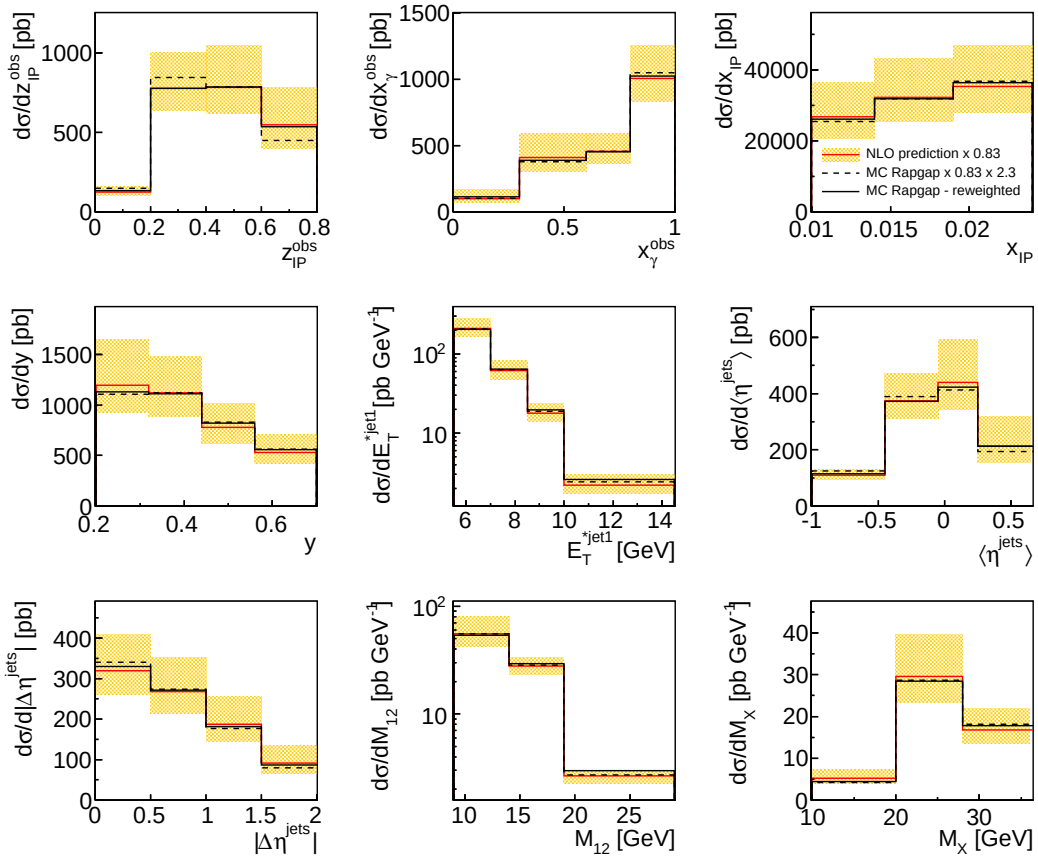

Fig. 6.9: The differential cross section for the PHP kinematic range as obtained by the NLO QCD calculation (red lines) and by the MC model Rapgap (black lines) at the parton-level which is normalized to the NLO calculations by the factor of 2.3. The scale uncertainties of the NLO calculations are represented by the yellow band. The Rapgap calculations are presented before (dashed lines) and after (solid lines) reweighing.

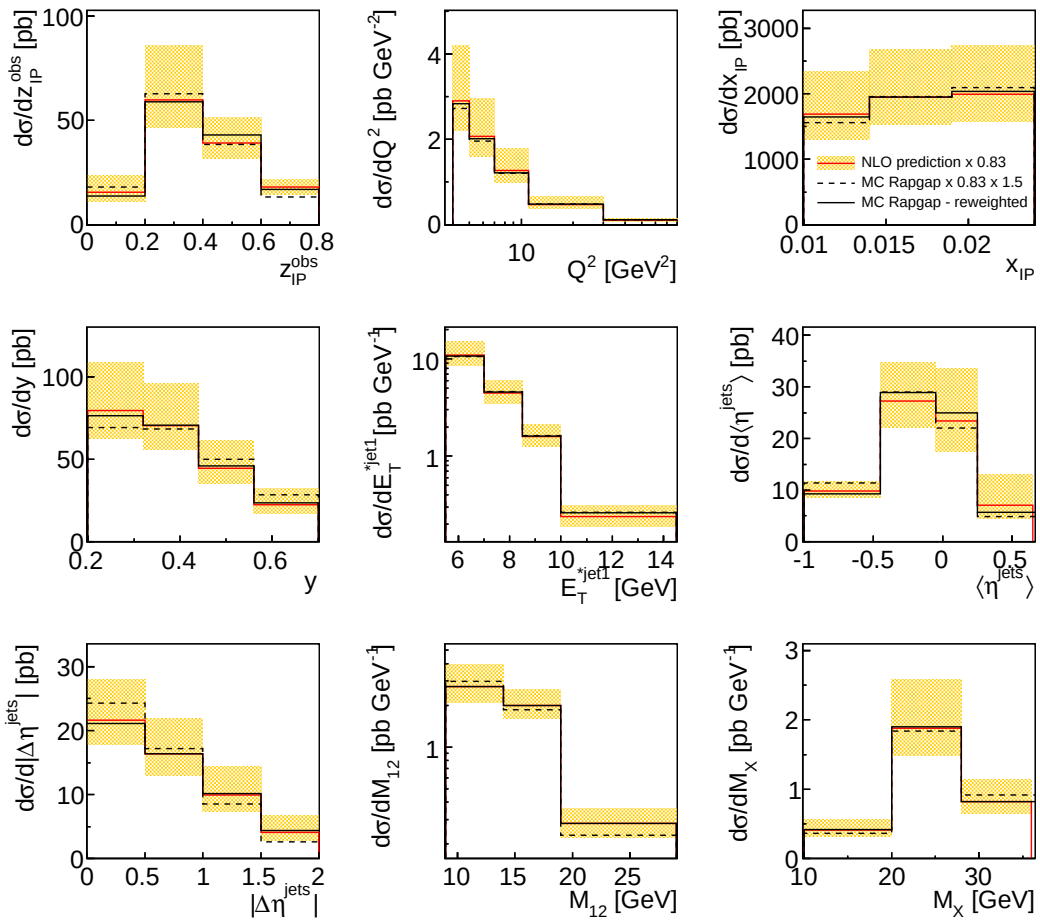

Fig. 6.10: The differential cross section for the DIS kinematic range as obtained by the NLO QCD calculation (red lines) and by the MC model RAPGAP (black lines) at the parton-level which is normalized to the NLO calculations by the factor of 1.5. The scale uncertainties of the NLO calculations are represented by the yellow band. The RAPGAP calculations are presented before (dashed lines) and after (solid lines) reweighing.

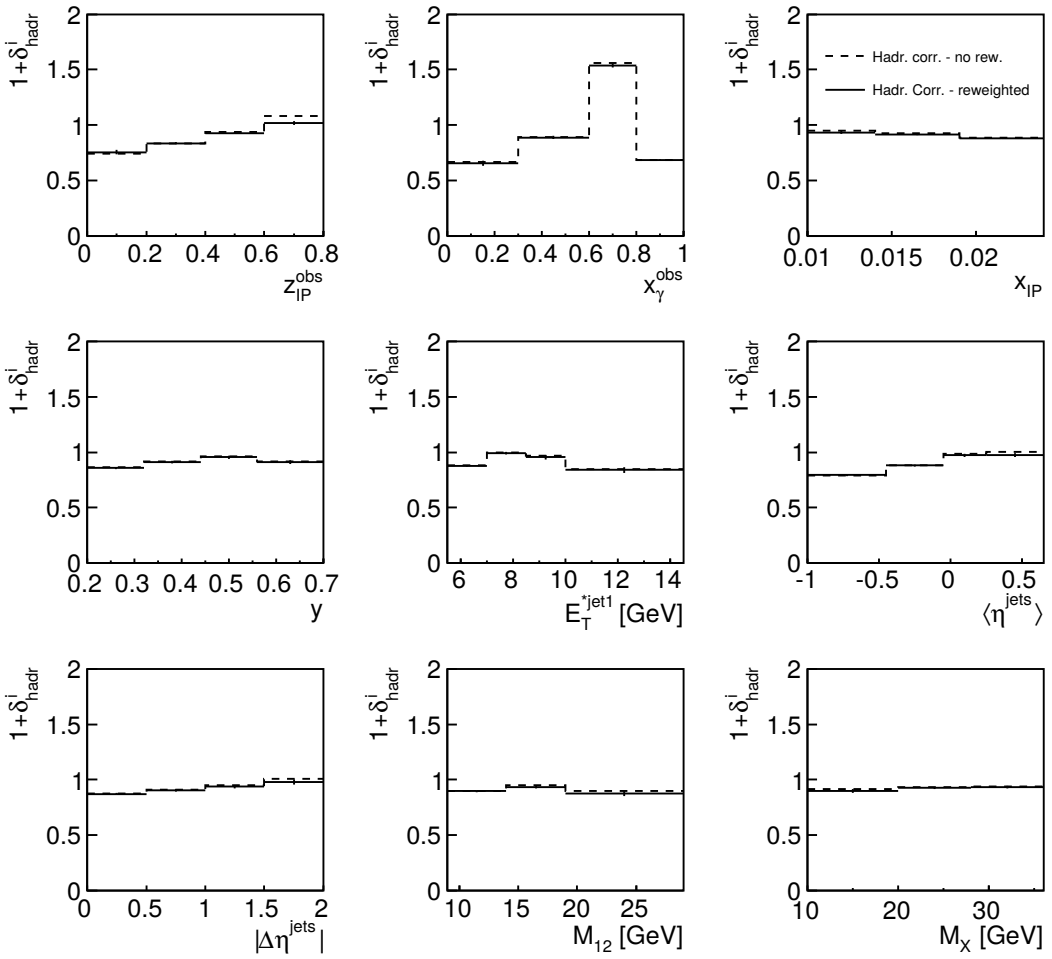

Fig. 6.11: The hadronization corrections $1 + \delta^i_{\mathrm{hadr}}$ in the PHP kinematic phase space. The dashed lines represent corrections obtained by unreweighted MC Rapgap while solid lines denote the final hadronisation corrections obtained by means of reweighted MC.

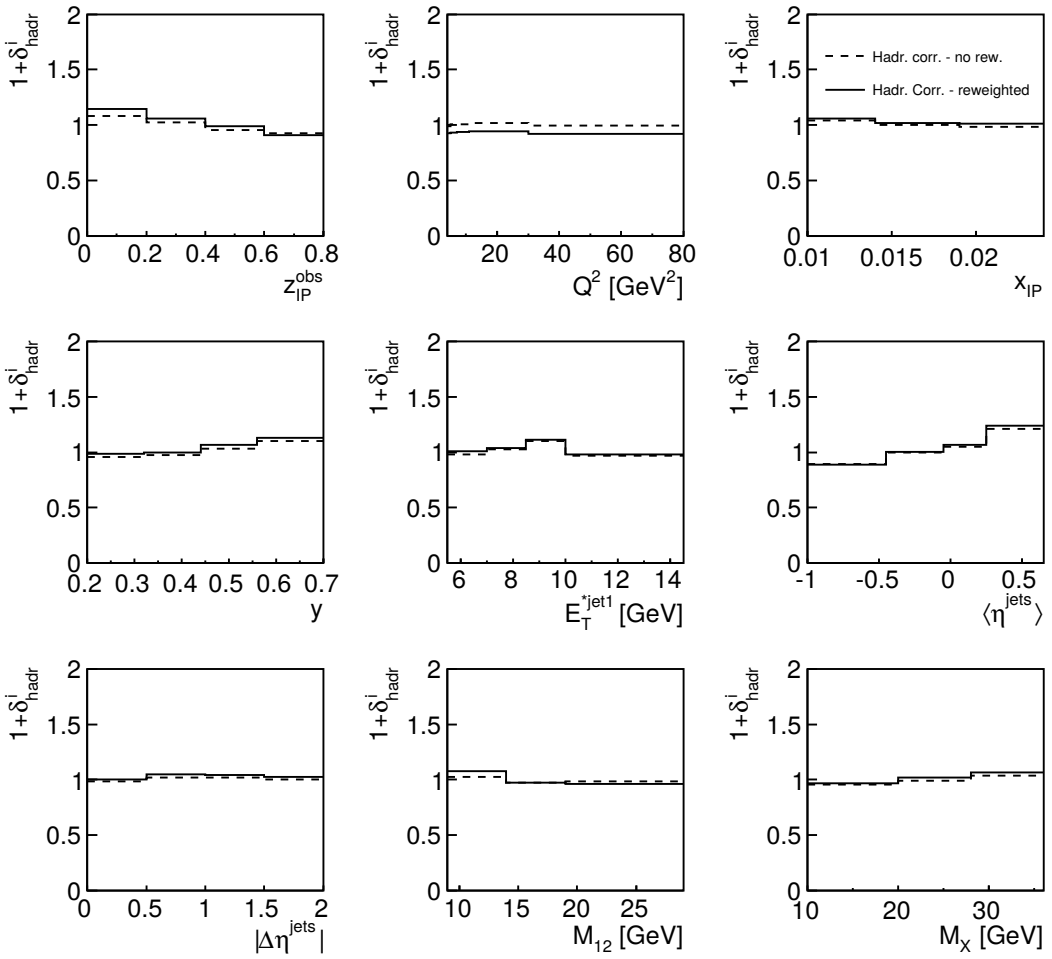

Fig. 6.12: The hadronization corrections $1 + \delta^i_{\text{hadr}}$ in the DIS kinematic phase space. The dashed lines represent corrections obtained by unreweighted MC RAPGAP while solid lines denote the final hadronisation corrections obtained by means of reweighted MC.

predictions are compared at the level of stable hadrons, but without QED radiation effects.

From the experimental point of view the emitted radiative photon is often very close to the scattered positron and both particles set up signal in the same cluster of the SPACAL which makes the determination of true positron energy impossible. On the other hand, the energy of the scattered positron before QED radiation is well correlated to the energy of the SPACAL cluster. This fact makes the data cross sections unfolded to the level without QED radiation more stable.

For this reason the data are corrected for the QED radiation in each bin i using radiative corrections δ^i_{rad} defined as:

$$1 + \delta^i_{\mathrm{rad}} = \frac{\sigma_i^{\mathrm{hadr}}(nrad)}{\sigma_i^{\mathrm{hadr}}(rad)}, \tag{6.19}$$

where both hadron level cross sections were obtained using MC Rapgap, for the non-radiative case the Heracles simulation has been turned off. The resulting correction factors are then applied in formulas (6.1) or (6.12).

The radiative corrections $(1 + \delta^i_{\mathrm{rad}})$ are shown in Fig. 6.13 for the DIS phase space and were found to be negligible for photoproduction. Even in the DIS region the corrections δ^i_{rad} are in average 0.00 ± 0.04, where the standard deviation is evaluated from all bins of all distributions shown in Fig. 6.13.

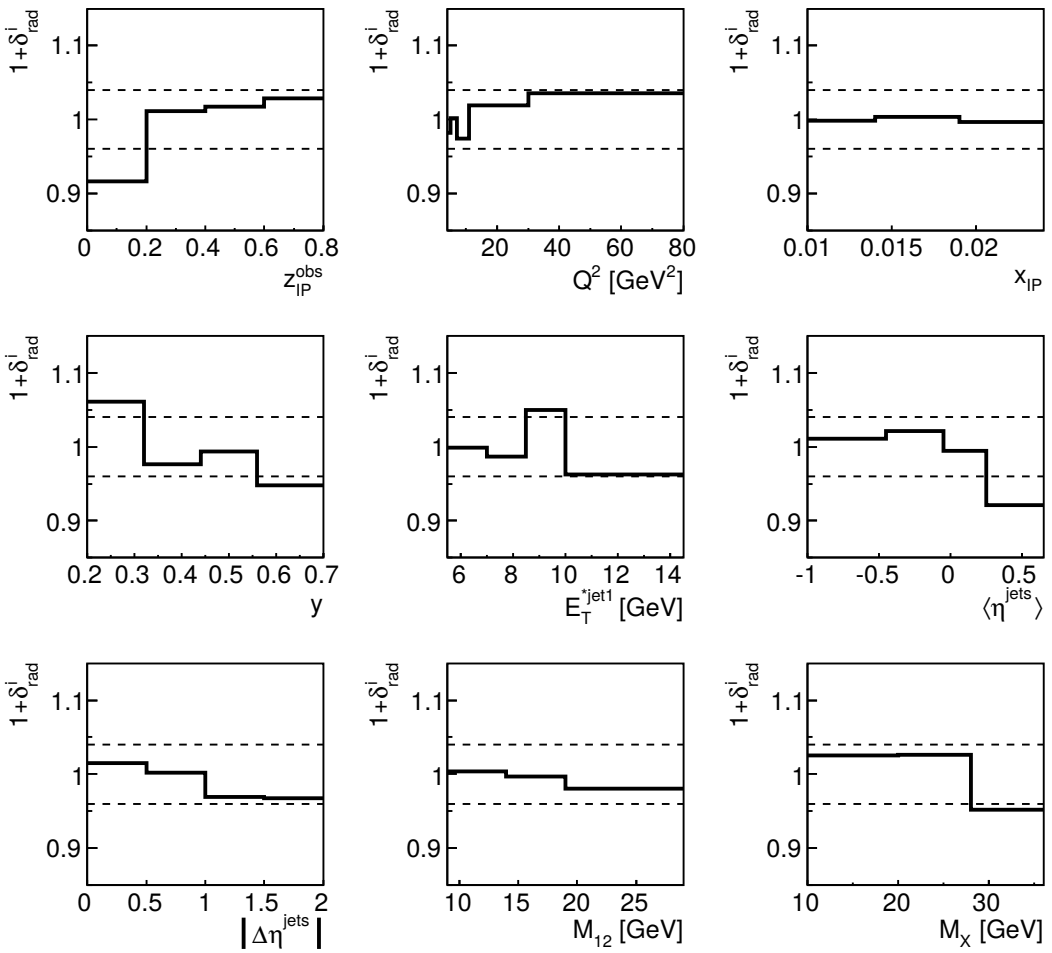

Fig. 6.13: The radiative corrections $1 + \delta^i_{\rm rad}$ in the DIS phase space region as defined by the relation (6.19). The band of 4% variation is represented by the dashed lines.

Chapter 7

Results

The diffractive e^+p dijet cross sections were measured in the kinematic range specified in Tab. 5.4 and were compared to the NLO QCD predictions (section 2.5) relaying on a validity of the collinear factorization theorem.

All NLO QCD predictions are scaled down by a factor of $1/1.2 = 0.83$ [83], presented in expression (4.3), to account for contributions from proton dissociation, which is present in the DPDF, but not in the data. The 9% uncertainty of this scaling factor is omitted.

The dependence of the predicted cross sections on the diffractive parton distribution function was considered by means of the 30 eigenvectors describing the uncertainties[1] of the central H1 2006 Fit B [4]. The cross sections were calculated for each DPDF error shift separately, the resulting error (generally asymmetric) is calculated using the sign improved quadratic sum of all these cross sections deviations with respect to the central value.

The effect of the photon distribution function on the resulting cross section in photoproduction was studied using an alternative AFG distribution function [50] instead of the default GRV γ-PDF [49].

7.1 Integrated Cross Sections

The integrated cross section for the photoproduction and the DIS regime is presented in Tab. 7.1 together with the NLO QCD predictions.

In the DIS regime, the theoretical prediction agrees with the measurement within the uncertainties. The same conclusions were made in the previous publications of both H1 and ZEUS collaborations [6, 8, 17, 86, 87], the results of which are summarised in Tab. 4.2. However, the unique analysis phase space driven for example by the

[1] The error fits are not made public for non-members of H1 collaboration, the responsible persons are Frank-Peter Schilling (frank-peter.schilling@cern.ch) and Paul Newman (newmanpr@mail.desy.de).

	PHP	DIS
Data [pb]	237 ± 14 (stat) ± 31 (syst)	30.5 ± 1.6 (stat) ± 2.8 (syst)
NLO QCD [pb]	430 $^{+172}_{-98}$ (scale) $^{+48}_{-61}$ (DPDF)	28.3 $^{+11.4}_{-6.4}$ (scale) $^{+3.0}_{-4.0}$ (DPDF)
Data/NLO	0.55 ± 0.08 (data) $^{+0.23}_{-0.15}$ (theory)	1.08 ± 0.11 (data) $^{+0.45}_{-0.29}$ (theory)

Tab. 7.1: Integrated e^+p diffractive dijet cross sections in the PHP and DIS regimes compared to NLO QCD calculations using the H12006 Fit-B DPDF set and GRV γ-PDF in resolved photoproduction. The measured cross sections are shown with statistical and systematic uncertainties. For the theoretical predictions, the uncertainties from scale variations and from the H12006 Fit-B DPDFs and hadronization corrections are shown. The ratios data/NLO are also given.

VFPS acceptance prevents from the direct comparison of the data to the previous measurements. Using an alternative QCD scale $(E_T^{*\mathrm{jet1}})^2 + Q^2/4$ which was suggested by Misha Ryskin leads to similar ratio $\sigma_{data}/\sigma_{NLO} = 1.07$.

In contrast, the predicted NLO QCD integrated diffractive dijet cross section in photoproduction overestimates the measured cross section by almost a factor of two. A comparable suppression factor[2] of 0.59 is obtained using an alternative AFG photon distribution function [50]. The observed suppression agrees with the previous H1 publications [16, 17] (Tab. 4.5) based on different data sets, where the diffractive events were selected using large rapidity gap method and the electron was measured by the electron tagger. On the contrary, the photoproduction data measured by the ZEUS collaboration [18] agree with the NLO QCD prediction within the theoretical uncertainty. The ZEUS collaboration observed perfect agreement for H1 Fit Jets [6] and ZEUS SJ DPDFs [88] as presented in Tab. 4.4.

7.2 The Differential Diffractive Dijet Cross Sections in DIS

The measured diffractive DIS cross sections differential in z_{IP}^{obs}, x_{IP}, y and Q^2 together with the NLO QCD predictions are shown in Fig. 7.1. The additional kinematic distributions $E_T^{*\mathrm{jet1}}$, M_X, $|\Delta\eta^{\mathrm{jets}}|$ and $\langle\eta^{\mathrm{jets}}\rangle$ are shown in Fig. 7.2. For all distributions the NLO QCD calculations within the theoretical and data uncertainties agree with the measured distributions.

[2] A suppression factor is defined as a ratio of data to the NLO QCD cross sections.

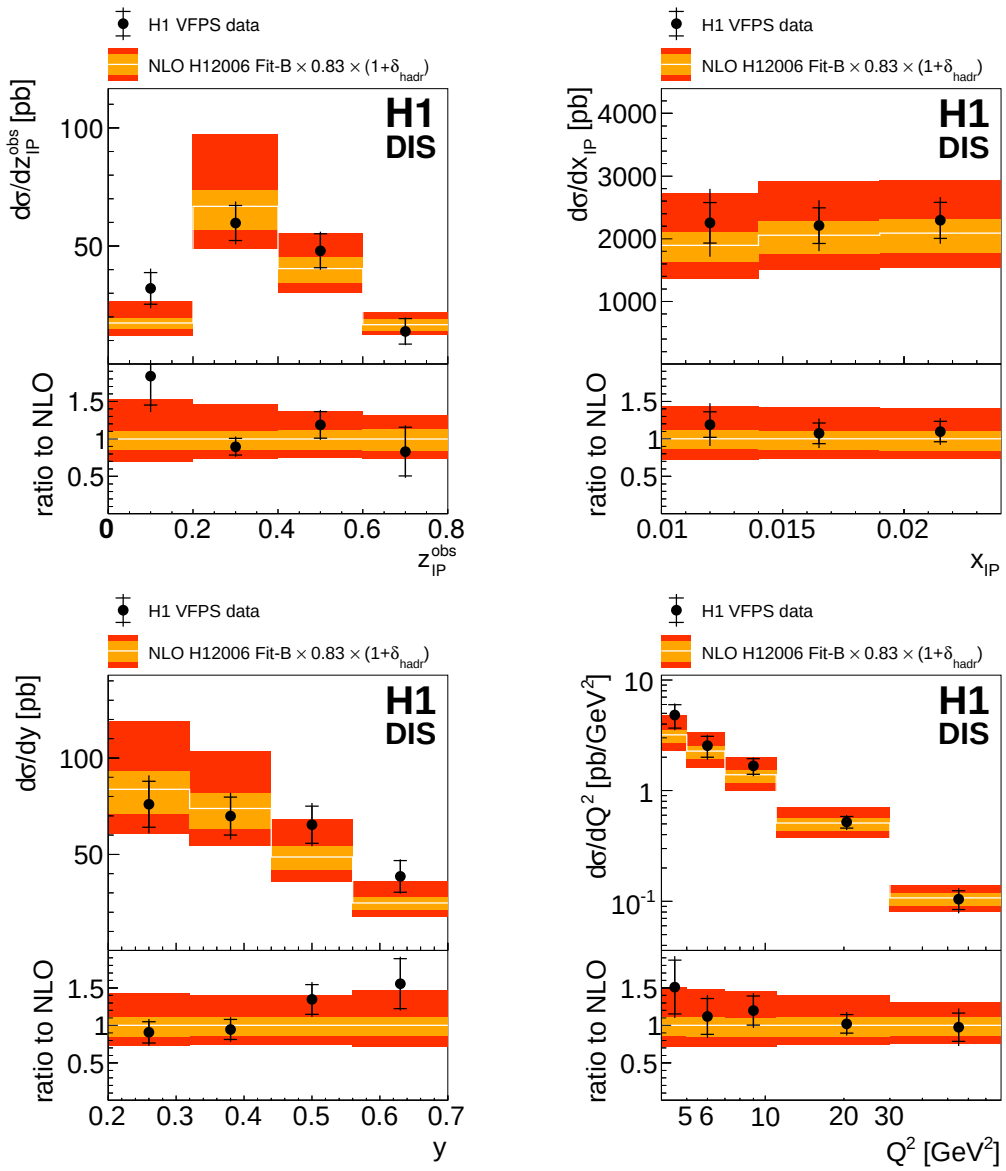

Fig. 7.1: The diffractive DIS cross sections differential in z_{IP}^{obs}, x_{IP}, y and Q^2. The inner error bars represent the statistical uncertainties, the outer error bars show statistical and systematic errors added in quadrature. The overall data normalisation uncertainty of 6% is not shown. The NLO QCD predictions based on H1 2006 Fit B DPDF set, corrected to the level of stable hadrons, are shown as a white line. The inner orange bands indicate the uncertainties of the DPDF fit and hadronization corrections added in quadrature. The outer red bands indicate the total uncertainties of the NLO QCD predictions, also including the QCD scale μ variation by a factor of 0.5 and 2. For each variable also the ratio to the NLO prediction is given in the lower panel.

However, a somewhat different shape is observed for data and theory in the Q^2 distribution, where the data cross section is larger in the lowest Q^2 bin, although this deviation is still covered by the uncertainties. The higher twist [129] or resolved photon [130] contributions, which are missing in presented NLO QCD calculations, are expected to play role in such small Q^2 regime. Especially the inclusive diffractive DIS data for the H1 2006 Fit B [4] were fitted from $Q^2_{\mathrm{min}} = 8.5\,\mathrm{GeV}^2$ because for lower Q^2 the data were systematically above the fit and the χ^2 was deteriorating. The predicted y differential cross sections also slightly differ from the measurement, such that the for higher y the smaller cross section is predicted than observed. Similar shape deviations in Q^2 and y were observed in the latest H1 measurement of the diffractive dijet production in DIS based on large rapidity gap selection [86] with much higher statistical significance[3]. The cross section as a function of $E_T^{*\mathrm{jet1}}$ is observed to be slightly harder than predicted, although still in agreement within uncertainties.

7.3 The Differential Diffractive Dijet Cross Sections in Photoproduction

For the photoproduction regime, the measured diffractive cross sections differential in z_{IP}^{obs}, x_{IP}, y and x_γ^{obs} together with the NLO QCD predictions are shown in Fig. 7.3. The additional kinematic distributions $E_T^{*\mathrm{jet1}}$, M_X, $|\Delta\eta^{\mathrm{jets}}|$ and $\langle\eta^{\mathrm{jets}}\rangle$ are shown in Fig. 7.4.

[3]The integrated luminosity of that analysis is $290\,\mathrm{pb}^{-1}$.

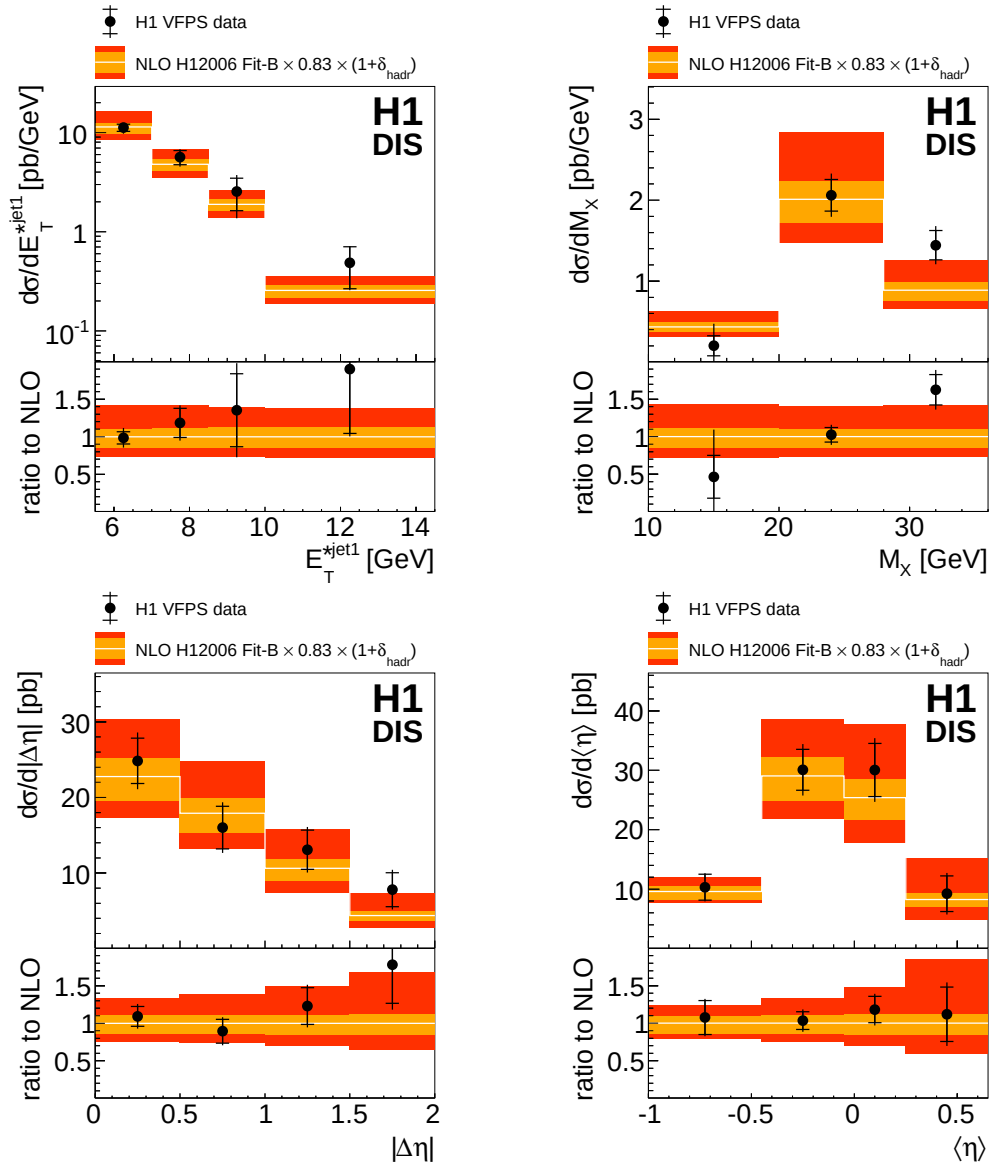

Fig. 7.2: The diffractive DIS cross sections differential in $E_T^{*\mathrm{jet1}}$, M_X, $|\Delta\eta^{\mathrm{jets}}|$ and $\langle\eta^{\mathrm{jets}}\rangle$. The detailed description is given in caption of Fig. 7.1.

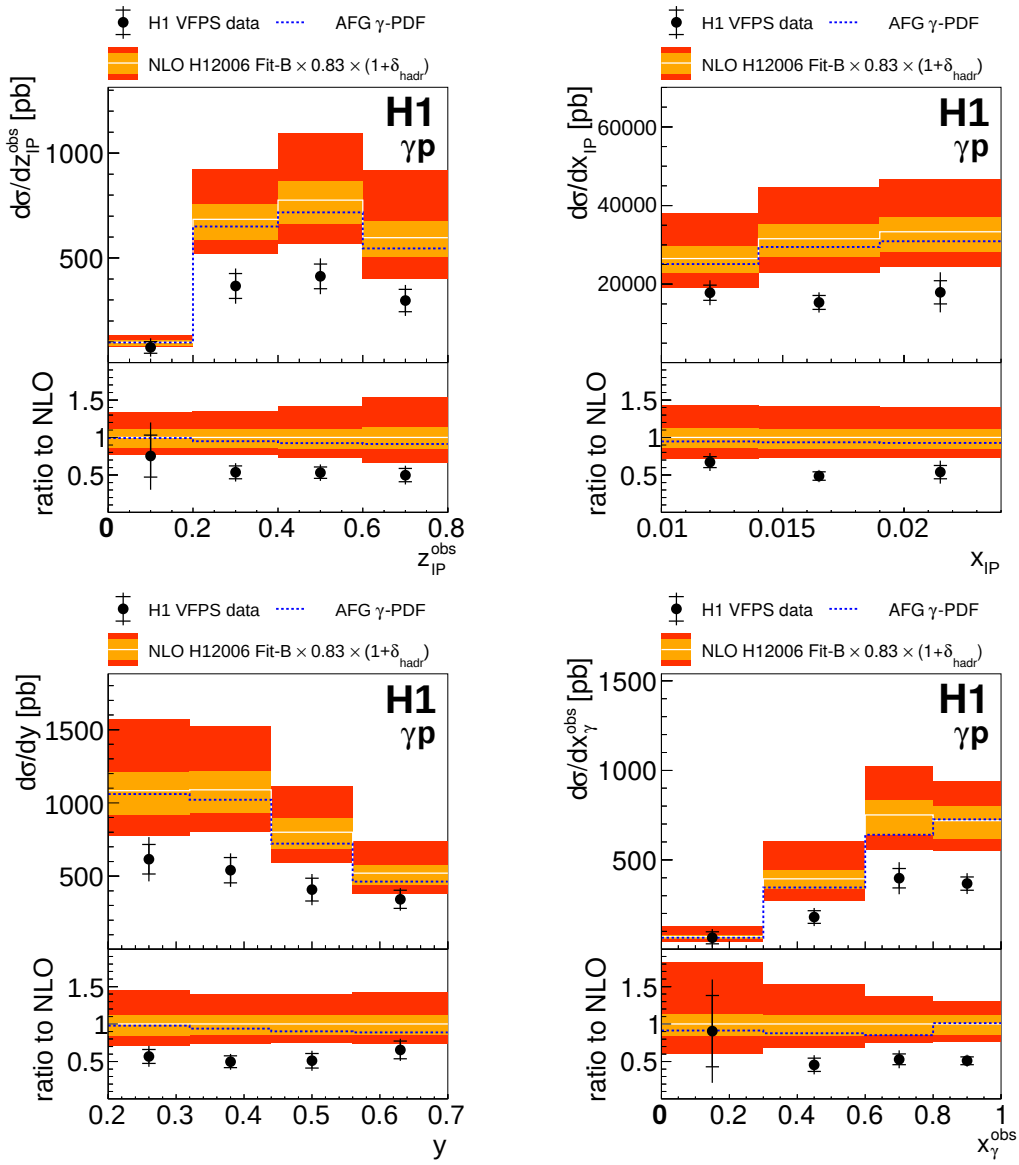

Fig. 7.3: The diffractive PHP cross sections differential in z_{IP}^{obs}, x_{IP}, y and x_γ. The inner error bars represent the statistical uncertainties, the outer error bars show statistical and systematic errors added in quadrature. The overall data normalisation uncertainty of 6% is not shown. The NLO QCD predictions based on H1 2006 Fit B DPDF set and GRV γ-PDF, corrected to the level of stable hadrons, are shown as a white line. The inner orange bands indicate the uncertainties of the DPDF fit and hadronization corrections added in quadrature. The outer red bands indicate the total uncertainties of the NLO QCD predictions, also including the QCD scale μ variation by a factor of 0.5 and 2. The alternative NLO QCD calculations based on AFG γ-PDF are shown by a dashed blue line. For each variable also the ratio to the NLO prediction is given in the lower panel.

The NLO QCD calculations agree well with the measured distributions in shape but overestimate the measured cross section in normalization as discussed in section 7.1. In particular, there is no indication of the resolved contribution ($x_\gamma \lesssim 0.8$) being more suppressed compared to the direct one. This statement is even stronger when an alternative AFG photon distribution function is used, since the predicted resolved photon ($x_\gamma \lesssim 0.8$) cross sections are then smaller. One should however take into account that the migration of the direct events ($x_\gamma = 1$) at the parton level towards lower values due to the hadronization can lower the significance of this effect. This suppression difference in x_γ was predicted in [15, 96], but within uncertainties not observed in any previous measurements (Fig. 4.7). There is also no significant shape variation between the data and the NLO QCD calculations for z_{IP}^{obs} and $E_T^{*\mathrm{jet1}}$ distributions which are sensitive to the diffractive parton densities and the hard scale which is in accordance with previous H1 large rapidity gap measurements [16, 17].

7.4 The Double Ratio of the PHP and DIS Cross Sections

The conclusion made in section 7.1 about the possible factorization breaking in the diffractive dijet photoproduction suffers from large theoretical uncertainties. This situation is summarised in Fig. 7.5, where the differential cross section is shown as a function of the photon virtuality Q^2 for both the photoproduction ($0 < Q^2 < 2\,\mathrm{GeV}^2$) and DIS ($4 < Q^2 < 80\,\mathrm{GeV}^2$) regime. Such a plot is relevant because the PHP and DIS phase space definitions were chosen to differ only in Q^2 whereas all remaining kinematic restrictions are identical (Tab. 5.4). The photon virtuality region ($2 < Q^2 < 4\,\mathrm{GeV}^2$) lies just on the edge of the SpaCal acceptance and is therefore hardly experimentally accessible. The figure 7.5 demonstrates that in the DIS region, there is no significant deviation of the suppression factor from unity whereas in photoproduction the NLO QCD calculations based on QCD collinear factorization theorem fail to describe the measured cross section.

A sophisticated method to test QCD factorization, firstly applied at HERA in [17] is to examine the deviations of the ratio of PHP and DIS cross sections for data and NLO QCD calculations (Tab. 7.2). In such a ratio for data, the systematic uncertainties are reduced with exception of the model uncertainties which are taken to be uncorrelated between the PHP and DIS regime. Furthermore, in the ratio of corresponding NLO QCD predictions the DPDFs uncertainties and uncertainties from the QCD scale variation cancel to large extent if the scale is varied simultaneously in both phase space regimes. In contrast, the hadronisation corrections, estimated to be 3% for both photoproduction and DIS (section 6.4), are considered being uncorrelated between PHP and DIS.

The double ratio of photoproduction to DIS for data to NLO QCD predictions is given in the bottom part of Tab. 7.2 and is shown together with PHP and DIS

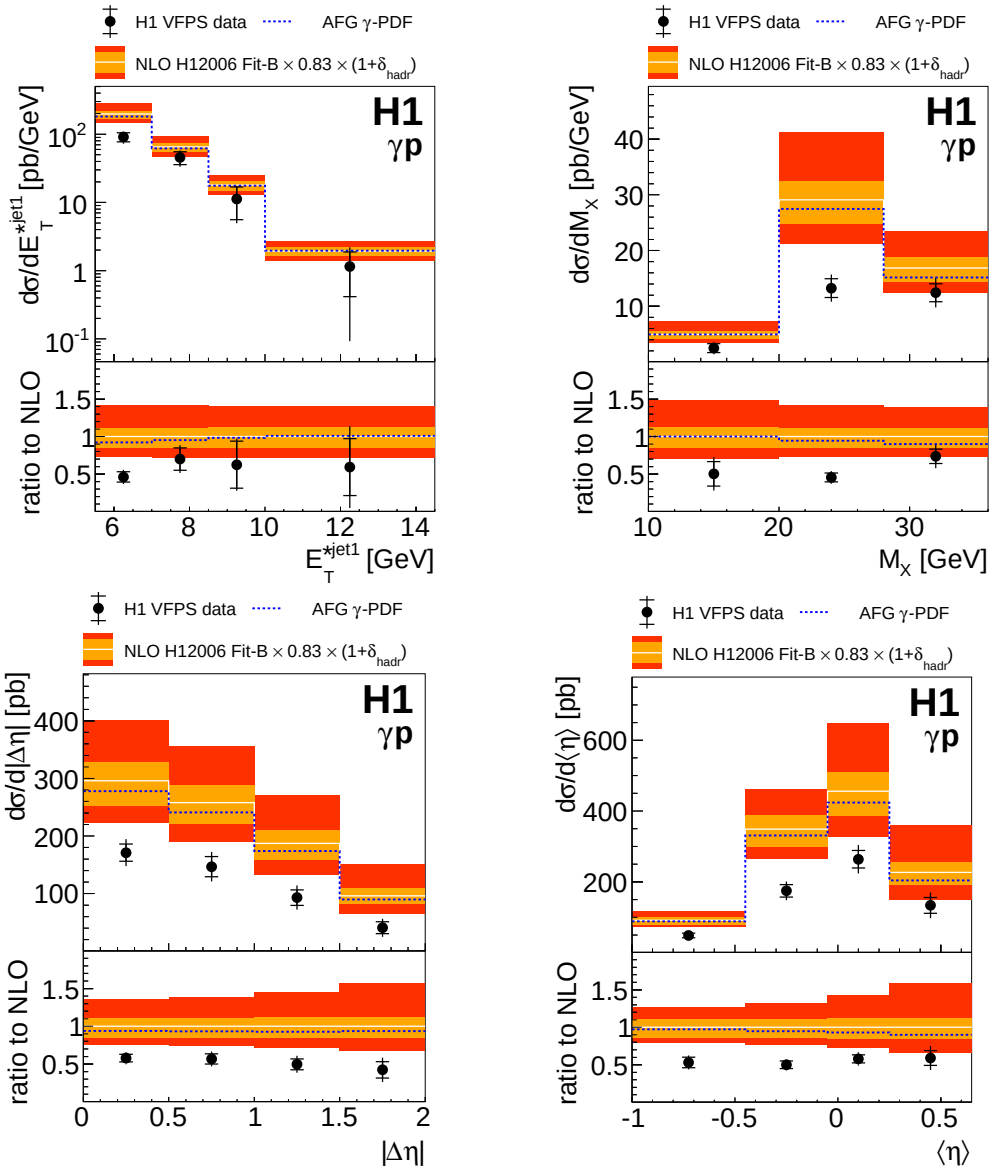

Fig. 7.4: The diffractive PHP cross sections differential in $E_T^{*\mathrm{jet1}}$, M_X, $|\Delta\eta^{\mathrm{jets}}|$ and $\langle\eta^{\mathrm{jets}}\rangle$. The detailed description is given in caption of Fig. 7.1.

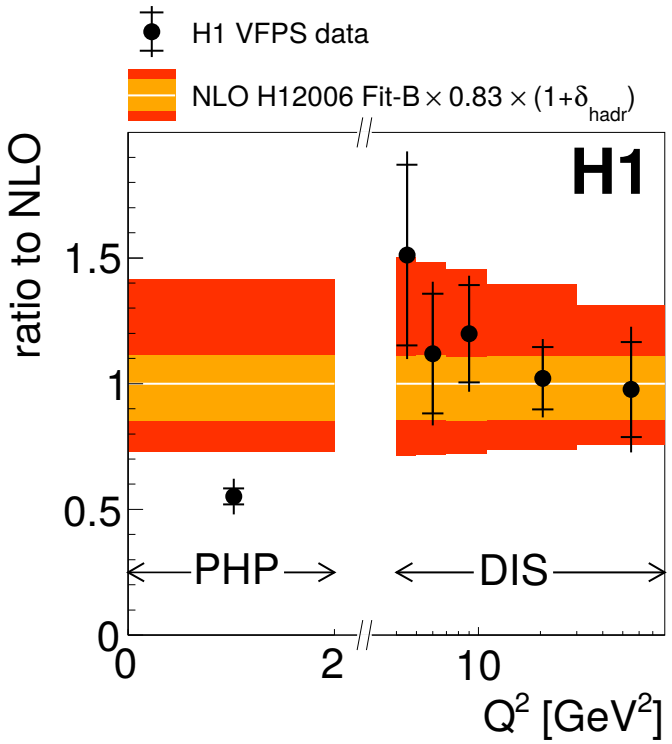

Fig. 7.5: The diffractive dijet cross section in the PHP ($Q^2 < 2\,\mathrm{GeV}^2$) and DIS ($Q^2 > 4\,\mathrm{GeV}^2$) regime normalized to the NLO QCD prediction differential in the photon virtuality Q^2. The inner bars represent the statistical uncertainties. The outer bars shows statistical and systematic uncertainties added in quadrature. The data points are shown in the geometrical bin centres. The NLO QCD predictions based on the H12006 Fit-B DPDF set and, in case of photoproduction, on the GRV γ-PDF are shown as a white line. These predictions are corrected for the effects of hadronization and proton dissociation. The inner orange band indicates the size of the DPDF uncertainties and the hadronization corrections added in quadrature. The outer red band indicates the total uncertainty of the NLO QCD cross sections, also including the QCD scale μ variation by a factor of 0.5 and 2. Note that the linear scale on the horizontal axis changes to logarithmic at $Q^2 = 2\,\mathrm{GeV}^2$.

	Ratio of photoproduction to DIS
Data	7.78 ± 0.60 (stat) ± 1.14 (syst)
NLO QCD	$15.21\,^{+0.00}_{-0.04}$ (scale) $^{+0.21}_{-0.10}$ (DPDF) ± 0.65 (hadr)
	14.22 with AFG γPDF
	14.17 with scale $\mu^2 = (E_T^{*\mathrm{jet1}})^2 + Q^2/4$
Data/NLO	0.511 ± 0.085 (data) $^{+0.022}_{-0.021}$ (theory)
	0.547 with AFG γPDF
	0.548 with scale $\mu^2 = (E_T^{*\mathrm{jet1}})^2 + Q^2/4$

Tab. 7.2: Ratio of integrated e^+p diffractive dijet cross sections for $Q^2 < 2\,\mathrm{GeV}^2$ (photoproduction) to $Q^2 > 4\,\mathrm{GeV}^2$ (DIS). Shown are the ratios for data and for the NLO calculation including two variants. The data and NLO uncertainties are indicated. The double ratios of data to NLO and its uncertainties are also given.

cross sections normalized to the NLO QCD predictions in Fig. 7.6. Due to reduced theoretical uncertainty the double ratio deviates significantly from unity indicating that the factorization does not hold in diffractive dijet photoproduction with respect to the same process in DIS. This conclusion is valid if the QCD scales are varied simultaneously in both regimes as suggested by [131] and as it was done in the previous dijets and open charm H1 diffractive analyses [7, 17].

The model dependence of this double ratio was studied by using an alternative QCD scale and photon distribution function. The usage of AFG γ-PDF set instead of default GRV rises the double ratio by 6%. Using an alternative[4] QCD scale $\mu^2 = (E_T^{*\mathrm{jet1}})^2 + Q^2/4$ leads to increase of the double ratio by 7%. The higher order corrections (NNLO) can also affect the resulting double ratio. The possible size of these corrections was determined as a difference between the leading-order and NLO QCD calculations scaled by $\alpha_s/2$, which amounts to 5%.

To summarise, the estimated double ratio which tests the validity of the QCD collinear factorization theorem significantly differs from unity and the possible model dependence of the QCD predictions cannot change this conclusion. The observed double ratio is consistent with the previous H1 large rapidity gap measurement 0.5 ± 0.1 [17], whereas no measurement of this double ratio by the ZEUS collaboration exists.

The possible shape dependencies of the double ratio are studied in Fig. 7.7 for variables $|\Delta\eta^{\mathrm{jets}}|$, y, z_{IP}^{obs} and $E_T^{*\mathrm{jet1}}$. The apparent shapes of the $|\Delta\eta^{\mathrm{jets}}|$ and y distribution differ form the NLO QCD predictions, but large uncertainties does not allow for any strong conclusion[5]. The shapes of z_{IP}^{obs} and $E_T^{*\mathrm{jet1}}$ seem to be in good agreement with

[4] The default scale is $\mu^2 = \langle E_T^{*\mathrm{jets}} \rangle^2 + Q^2$.

[5] The χ^2/N_{df} for the $|\Delta\eta^{\mathrm{jets}}|$ and y is 5.3/3 and 3.3/3, corresponding to p-value of 15% and 37%,

constant, especially there is no indication of the $E_T^{*\mathrm{jet1}}$ dependence of the double ratio as suggested in [15].

respectively.

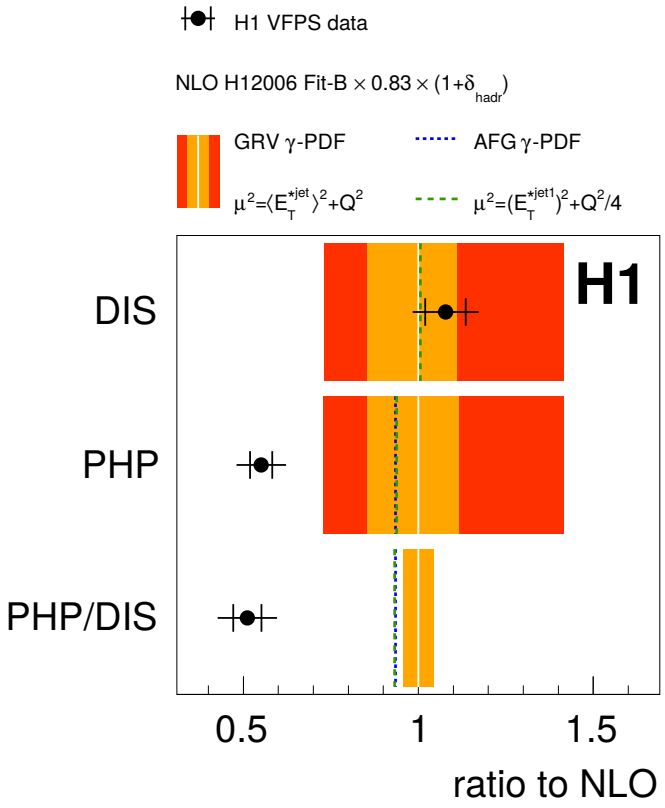

Fig. 7.6: The diffractive dijet cross section in the PHP and DIS regime normalized to the NLO QCD calculations. The double ratio of the of the PHP to DIS cross sections, normalized to the corresponding ratio of the NLO QCD predictions is also presented. The inner error bars represent the statistical uncertainties. The outer error bars show statistical and systematic uncertainties added in quadrature. The NLO QCD predictions based on the H12006 Fit-B DPDF set and, in case of photoproduction, on the GRV γ-PDF are shown as a white line. These predictions are corrected for the effects of hadronization and proton dissociation. The inner orange band indicates the size of the DPDF uncertainties and the hadronization corrections added in quadrature. The outer red band indicates the total uncertainty of the NLO QCD cross sections, also including the QCD scale μ variation by a factor of 0.5 and 2. Two alternative NLO QCD predictions normalized to the default one are also presented. The effect of an alternative AFG γ-PDF is studied in photoproduction and an alternative functional form of the QCD scale is studied both for photoproduction and DIS.

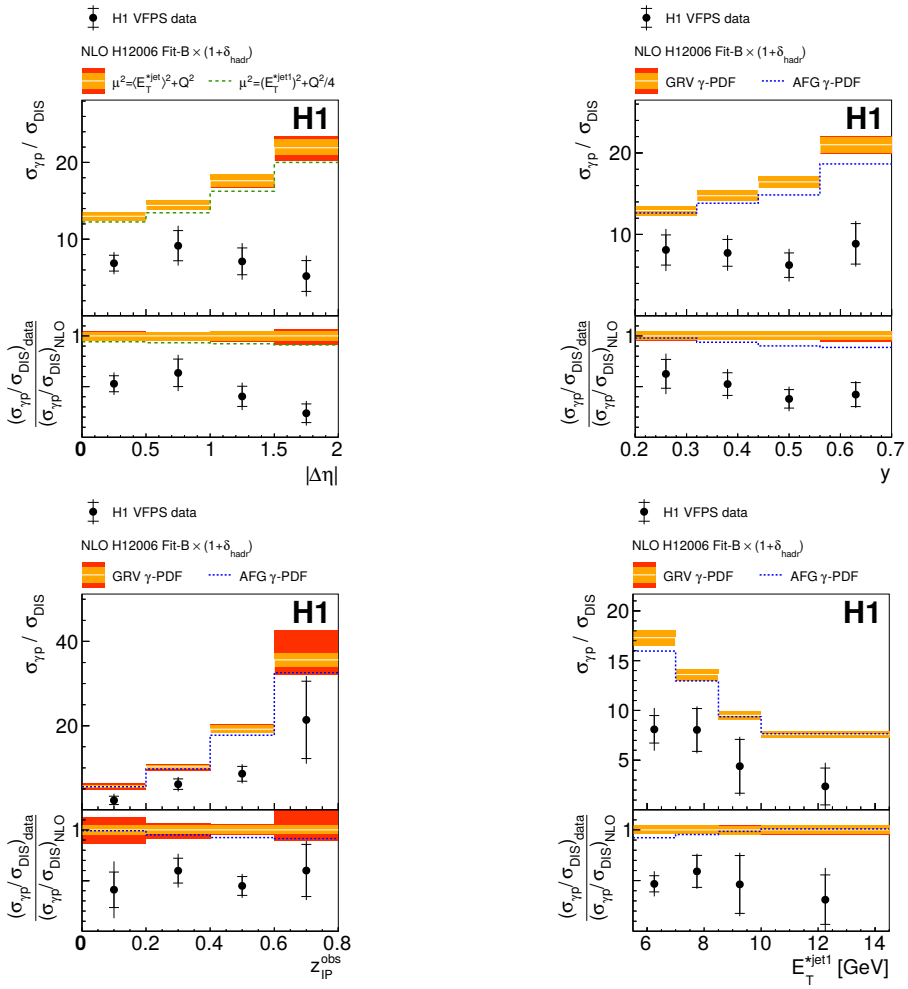

Fig. 7.7: Ratios of diffractive dijet photoproduction to DIS cross sections differential in $|\Delta\eta^{\text{jets}}|$, y, z_{IP}^{obs} and $E_T^{*\text{jet1}}$. The inner error bars represent the statistical uncertainties, the outer error bars indicate statistical and systematic uncertainties added in quadrature. The NLO QCD predictions are based on the H12006 Fit-B DPDF set and GRV γ-PDF and are corrected to the level of stable hadrons. The NLO QCD predictions are shown as a white line accompanied by the orange band which indicates the size of the DPDF and hadronization corrections uncertainties added in quadrature. The outer red band represent the total theoretical uncertainty, also including QCD scale μ variation by a factor of 0.5 and 2. Variants of the NLO QCD predictions with an alternative functional form of the scale (for $\Delta\eta$ distribution) and AFG γ-PDF are also presented. The possible shape dependencies can be studied in the double ratios presented in the bottom panel of each distribution.

Chapter 8

Conclusion

The diffractive dijet production was measured at HERA in photoproduction and deep-inelastic scattering (DIS) in the same kinematic range with only exception of photon virtuality which is $Q^2 < 2\,\mathrm{GeV}^2$ in photoproduction and $4 < Q^2 < 80\,\mathrm{GeV}^2$ in DIS. This work represents the first published physical analysis using the H1 Very Forward Proton Spectrometer which allows to measure leading protons in kinematic range $0.010 < x_{IP} < 0.024$ and $|t| < 0.6\,\mathrm{GeV}^2$. Furthermore, the leading proton detection was used in the photoproduction regime for the first time.

In DIS, the next-to-leading order (NLO) QCD calculations based on H12006 Fit-B diffractive parton densities (DPDF) of proton well describe the measured cross sections within the theoretical and experimental uncertainties both in normalization and shape. This result is consistent with previous H1 and ZEUS measurements and confirms validity of the QCD collinear factorization in this regime.

In photoproduction the NLO QCD calculation based on H12006 Fit-B DPDF and relaying on validity of the collinear QCD factorization theorem in this process overestimates the measured cross section by almost a factor of two. This result confirms previous H1 measurements, where the large rapidity gap method for the selection of the diffractive events was used. The shapes of the measured distributions are described within the uncertainties, especially there is no hint of dependence of the observed suppression on the variable x_γ^{obs} representing the fraction of the photon momentum entering to the hard subprocess. Indeed, the direct processes which contribute at higher values of x_γ^{obs} were found to be suppressed by a similar factor as resolved photon processes, which agrees which previous measurements of both HERA experiments.

In order to reduce the uncertainties in the suppression factor, the ratios of photoproduction to DIS cross sections and the double ratios of data to NLO were analysed. The integrated double ratio was found to be equal to 0.51 ± 0.09, suggesting the factorization breaking in the diffractive dijet photoproduction with high statistical significance. In addition, within the uncertainties, no dependence of the differential

double ratio on the leading jet transverse energy $E_T^{*\mathrm{jet1}}$ is observed. The measured double ratio agrees with older H1 analysis where the complementary experimental methods have been used. Contributions from proton dissociative processes present in the previous analyses but absent here are ruled out as a cause of the observed suppression.

To conclude, the H1 collaboration observe the factorization breaking in the diffractive dijets photoproduction in three independent measurements. The confidence level of this conclusion in the presented analysis is around 5σ, albeit the statistical interpretation of model uncertainties may be problematic.

Bibliography

[1] J. C. Collins, "Proof of factorization for diffractive hard scattering," *Phys.Rev.* **D57** (1998) 3051–3056, [hep-ph/9709499].

[2] P. Van Esch, M. Kapishin, A. Morozov, V. Spaskov, W. Bartel *et al.*, "The H1 forward proton spectrometer at HERA," *Nucl.Instrum.Meth.* **A446** (2000) 409–425, [hep-ex/0001046].

[3] A. Astvatsatourov, K. Černý, J. Delvax, L. Favart, T. Hreus *et al.*, "The H1 very forward proton spectrometer at HERA," *Nucl.Instrum.Meth.* **A736** (2014) 46–65.

[4] A. Aktas *et al.* [H1 Collaboration], "Measurement and QCD analysis of the diffractive deep-inelastic scattering cross section at HERA," *Eur. Phys. J.* **C48** (2006) 715–748, [hep-ex/0606004].

[5] S. Chekanov *et al.* [ZEUS Collaboration], "Dissociation of virtual photons in events with a leading proton at HERA," *Eur.Phys.J.* **C38** (2004) 43–67, [hep-ex/0408009].

[6] A. Aktas *et al.* [H1 Collaboration], "Dijet cross sections and parton densities in diffractive DIS at HERA," *JHEP* **0710** (2007) 042, [arXiv:0708.3217].

[7] A. Aktas *et al.* [H1 Collaboration], "Diffractive open charm production in deep-inelastic scattering and photoproduction at HERA," *Eur.Phys.J.* **C50** (2007) 1–20, [hep-ex/0610076].

[8] S. Chekanov *et al.* [ZEUS Collaboration], "Dijet production in diffractive deep inelastic scattering at HERA," *Eur.Phys.J.* **C52** (2007) 813–832, [arXiv:0708.1415].

[9] S. Chekanov *et al.* [ZEUS Collaboration], "Measurement of diffractive production of $D^{*\pm}$ (2010) mesons in deep inelastic scattering at HERA," *Phys.Lett.* **B545** (2002) 244–260, [hep-ex/0206020].

[10] T. Affolder *et al.* [CDF Collaboration], "Diffractive dijets with a leading antiproton in $\bar{p}p$ collisions at $\sqrt{s} = 1800$ GeV," *Phys.Rev.Lett.* **84** (2000) 5043–5048.

[11] S. Chatrchyan *et al.* [CMS Collaboration], "Observation of a diffractive contribution to dijet production in proton-proton collisions at $\sqrt{s} = 7$ TeV," *Phys.Rev.* **D87** (2013) 012006, [arXiv:1209.1805].

[12] A. Kaidalov, V. Khoze, A. Martin and M. Ryskin, "Unitarity effects in hard diffraction at HERA," *Phys.Lett.* **B567** (2003) 61–68, [hep-ph/0306134].

[13] A. B. Kaidalov, V. A. Khoze, A. D. Martin and M. G. Ryskin, "Factorization breaking in diffractive dijet production," *Phys. Lett.* **B559** (2003) 235–238, [hep-ph/0302091].

[14] E. Witten, "Anomalous cross section for photon-photon scattering in gauge theories," *Nucl.Phys.* **B120** (1977) 189–202.

[15] A. Kaidalov, V. Khoze, A. Martin and M. Ryskin, "Factorization breaking in diffractive dijet photoproduction at HERA," *Eur.Phys.J.* **C66** (2010) 373–376, [arXiv:0911.3716].

[16] F. D. Aaron *et al.* [H1 Collaboration], "Diffractive dijet photoproduction in *ep* collisions at HERA," *Eur. Phys. J.* **C70** (2010) 15–37, [arXiv:1006.0946].

[17] A. Aktas *et al.* [H1 Collaboration], "Tests of QCD factorisation in the diffractive production of dijets in deep-inelastic scattering and photoproduction at HERA," *Eur.Phys.J.* **C51** (2007) 549–568, [hep-ex/0703022].

[18] S. Chekanov *et al.* [ZEUS Collaboration], "Diffractive photoproduction of dijetsin *ep* collisions at HERA," *Eur. Phys. J.* **C55** (2008) 177–191, [arXiv:0710.1498].

[19] E. D. Bloom, D. Coward, H. DeStaebler, J. Drees, G. Miller *et al.*, "High energy inelastic *ep* scattering at 6-degrees and 10-degrees," *Phys.Rev.Lett.* **23** (1969) 930–934.

[20] J. Chýla, "Quarks, partons and Quantum Chromodynamics," 2004. Available at http://www-hep2.fzu.cz/Theory/notes/text.pdf.

[21] J. Callan, Curtis G. and D. J. Gross, "High-energy electroproduction and the constitution of the electric current," *Phys.Rev.Lett.* **22** (1969) 156–159.

[22] M. Gell-Mann, "A schematic model of baryons and mesons," *Phys.Lett.* **8** (1964) 214–215.

[23] E. Stueckelberg and A. Petermann, "Normalization of constants in the quanta theory," *Helv.Phys.Acta* **26** (1953) 499–520.

[24] M. Gell-Mann and F. Low, "Quantum electrodynamics at small distances," *Phys.Rev.* **95** (1954) 1300–1312.

[25] G. 't Hooft, "Dimensional regularization and the renormalization group," *Nucl.Phys.* **B61** (1973) 455–468.

[26] J. Callan, Curtis G., "Broken scale invariance in scalar field theory,"

Phys.Rev. **D2** (1970) 1541–1547.

[27] K. Symanzik, "Small distance behavior in field theory and power counting," *Commun.Math.Phys.* **18** (1970) 227–246.

[28] D. J. Gross and F. Wilczek, "Ultraviolet behavior of nonabelian gauge theories," *Phys.Rev.Lett.* **30** (1973) 1343–1346.

[29] K. Olive *et al.* [Particle Data Group], "Review of Particle Physics," *Chin.Phys.* **C38** (2014) 090001.

[30] K. G. Wilson, "Confinement of quarks," *Phys.Rev.* **D10** (1974) 2445–2459.

[31] G. Altarelli and G. Parisi, "Asymptotic freedom in parton language," *Nucl.Phys.* **B126** (1977) 298.

[32] R. Ellis, W. Stirling and B. Webber, *QCD and collider physics*, vol. 8. Cambridge University Press, 1996.

[33] V. N. Gribov and L. N. Lipatov, "Deep-inelastic *ep* scattering in perturbation theory," *Sov. J. Nucl. Phys.* **15** (1972) 438–450. [Yad. Fiz.15,781(1972)].

[34] F. Aaron *et al.* [H1 Collaboration], "Inclusive deep inelastic scattering at high Q^2 with longitudinally polarised lepton beams at HERA," *JHEP* **1209** (2012) 061, [arXiv:1206.7007].

[35] J. Vermaseren, A. Vogt and S. Moch, "The third-order QCD corrections to deep-inelastic scattering by photon exchange," *Nucl.Phys.* **B724** (2005) 3–182, [hep-ph/0504242].

[36] J. C. Collins, D. E. Soper and G. F. Sterman, "Factorization of hard processes in QCD," *Adv. Ser. Direct. High Energy Phys.* **5** (1989) 1–91, [hep-ph/0409313].

[37] G. F. Chew, *S-matrix theory of strong interactions*. Pearson Benjamin Cummings, 1962.

[38] A. Donnachie and P. V. Landshoff, "Total cross sections," *Phys. Lett.* **B296** (1992) 227–232, [hep-ph/9209205].

[39] E. Klempt and A. Zaitsev, "Glueballs, Hybrids, Multiquarks. Experimental facts versus QCD inspired concepts," *Phys.Rept.* **454** (2007) 1–202, [arXiv:0708.4016].

[40] C. J. Morningstar and M. J. Peardon, "The Glueball spectrum from an anisotropic lattice study," *Phys.Rev.* **D60** (1999) 034509, [hep-lat/9901004].

[41] M. Froissart, "Asymptotic behavior and subtractions in the Mandelstam representation," *Phys.Rev.* **123** (1961) 1053–1057.

[42] A. Martin, "Extension of the axiomatic analyticity domain of scattering amplitudes by unitarity-I," *Nuovo Cim.* **A42** (1965) 930–953.

[43] A. H. Mueller, "O(2,1) analysis of single particle spectra at high energy," *Phys.Rev.* **D2** (1970) 2963–2968.

[44] L. Landau and I. Pomeranchuk, "Limits of applicability of the theory of bremsstrahlung electrons and pair production at high-energies," *Dokl.Akad.Nauk Ser.Fiz.* **92** (1953) 535–536.

[45] M. Good and W. Walker, "Diffraction disssociation of beam particles," *Phys.Rev.* **120** (1960) 1857–1860.

[46] J. Bjorken, "Rapidity gaps and jets as a new physics signature in very high-energy hadron hadron collisions," *Phys.Rev.* **D47** (1993) 101–113.

[47] V. Barone and E. Predazzi, *High energy particle diffraction*. Springer, 2002.

[48] G. Abbiendi *et al.* [OPAL Collaboration], "Measurement of the low x behavior of the photon structure function F_2^γ," *Eur.Phys.J.* **C18** (2000) 15–39, [hep-ex/0007018].

[49] M. Gluck, E. Reya and A. Vogt, "Parton structure of the photon beyond the leading order," *Phys. Rev.* **D45** (1992) 3986–3994.

[50] P. Aurenche, J. P. Guillet and M. Fontannaz, "Parton distributions in the photon," *Z. Phys.* **C64** (1994) 621–630, [hep-ph/9406382].

[51] C. von Weizsacker, "Radiation emitted in collisions of very fast electrons," *Z.Phys.* **88** (1934) 612–625.

[52] E. Williams, "Nature of the high-energy particles of penetrating radiation and status of ionization and radiation formulae," *Phys.Rev.* **45** (1934) 729–730.

[53] L. Alvero, J. C. Collins, J. Terron and J. J. Whitmore, "Diffractive production of jets and weak bosons, and tests of hard scattering factorization," *Phys. Rev.* **D59** (1999) 074022, [hep-ph/9805268].

[54] E. Gotsman, E. Levin, U. Maor, E. Naftali and A. Prygarin, "Survival probability of large rapidity gaps," in *HERA and the LHC: A Workshop on the Implications of HERA for LHC Physics*. 2005. [hep-ph/0511060].

[55] V. A. Khoze, A. D. Martin and M. Ryskin, "Soft diffraction and the elastic slope at Tevatron and LHC energies: A Multi-Pomeron approach," *Eur.Phys.J.* **C18** (2000) 167–179, [hep-ph/0007359].

[56] J. Breitweg *et al.* [ZEUS Collaboration], "Measurement of the diffractive cross-section in deep inelastic scattering using ZEUS 1994 data," *Eur.Phys.J.* **C6** (1999) 43–66, [hep-ex/9807010].

[57] J. Breitweg *et al.* [ZEUS Collaboration], "Measurement of the diffractive structure function $F_2^{D(4)}$ at HERA," *Eur.Phys.J.* **C1** (1998) 81–96, [hep-ex/9709021].

[58] M. Derrick *et al.* [ZEUS Collaboration], "Study of elastic ρ^0 photoproduction

at HERA using the ZEUS leading proton spectrometer," *Z.Phys.* **C73** (1997) 253–268, [hep-ex/9609003].

[59] H. Jung, "Hard diffractive scattering in high-energy e p collisions and the Monte Carlo generator RAPGAP," *Comp. Phys. Commun.* **86** (1995) 147–161.

[60] G. Veneziano, "Some aspects of a unified approach to gauge, dual and Gribov theories," *Nucl.Phys.* **B117** (1976) 519–545.

[61] T. Sjostrand, "High energy physics event generation with PYTHIA 5.7 and JETSET 7.4," *Comput.Phys.Commun.* **82** (1994) 74–90.

[62] G. Marchesini, B. Webber, G. Abbiendi, I. Knowles, M. Seymour *et al.*, "HERWIG: A Monte Carlo event generator for simulating hadron emission reactions with interfering gluons. Version 5.1 - April 1991," *Comput.Phys.Commun.* **67** (1992) 465–508.

[63] B. E. Cox and J. R. Forshaw, "POMWIG: HERWIG for diffractive interactions," *Comput.Phys.Commun.* **144** (2002) 104–110, [hep-ph/0010303].

[64] A. Kwiatkowski, H. Spiesberger and H. Mohring, "HERACLES: an event generator for *ep* interactions at HERA energies including radiative processes," *Comput.Phys.Commun.* **69** (1992) 155–172.

[65] R. Brun, F. Bruyant, M. Maire, A. McPherson and P. Zanarini, "GEANT Detector Description and Simulation Tool." CERN Program Library Long Writeup W5013, 1987.

[66] S. Frixione, Z. Kunszt and A. Signer, "Three-jet cross sections to next-to-leading order," *Nucl.Phys.* **B467** (1996) 399–442, [hep-ph/9512328].

[67] Z. Nagy, "Next-to-leading order calculation of three jet observables in hadron hadron collision," *Phys.Rev.* **D68** (2003) 094002, [hep-ph/0307268].

[68] G. Ingelman and P. Schlein, "Jet structure in high mass diffractive scattering," *Phys.Lett.* **B152** (1985) 256.

[69] M. Klasen and G. Kramer, "Inclusive two jet production at HERA: Direct and resolved cross sections in next-to-leading order QCD," *Z.Phys.* **C76** (1997) 67–74, [hep-ph/9611450].

[70] K. Černý, *Tests of QCD hard factorization in diffractive photoproduction of dijets at HERA*. PhD thesis, Charles University, 2008. Available at http://www-h1.desy.de/psfiles/theses/h1th-493.pdf.

[71] J. Chýla, J. Cvach, K. Sedlák and M. Taševský, "QCD analysis of dijet production at low Q^2 at HERA," *Eur.Phys.J.* **C40** (2005) 469–472, [hep-ph/0501065].

[72] S. Catani, Y. L. Dokshitzer and B. Webber, "The K-perpendicular clustering

algorithm for jets in deep inelastic scattering and hadron collisions," *Phys.Lett.* **B285** (1992) 291–299.

[73] M. Cacciari, G. P. Salam and G. Soyez, "The anti-k(t) jet clustering algorithm," *JHEP* **0804** (2008) 063, [arXiv:0802.1189].

[74] V. Andreev *et al.* [H1 Collaboration], "Measurement of multijet production in *ep* collisions at high Q^2 and determination of the strong coupling α_s," *Eur.Phys.J.* **C75** no. 2, (2015) 65, [arXiv:1406.4709].

[75] I. Abt *et al.* [H1 Collaboration], "The H1 detector at HERA," *Nucl.Instrum.Meth.* **A386** (1997) 310–347.

[76] I. Abt *et al.* [H1 Collaboration], "The tracking, calorimeter and muon detectors of the H1 experiment at HERA," *Nucl.Instrum.Meth.* **A386** (1997) 348–396.

[77] R. Appuhn *et al.* [H1 SPACAL Group], "The H1 lead/scintillating fiber calorimeter," *Nucl.Instrum.Meth.* **A386** (1997) 397–408.

[78] H. Bethe and W. Heitler, "On the stopping of fast particles and on the creation of positive electrons," *Proc.Roy.Soc.Lond.* **A146** (1934) 83–112.

[79] A. Schoning [H1 Collaboration], "The Fast Track Trigger at the H1 experiment design concepts and algorithms," *Nucl.Instrum.Meth.* **A566** (2006) 130–132.

[80] F. Aaron *et al.* [H1 Collaboration], "Inclusive measurement of diffractive deep-inelastic scattering at HERA," *Eur.Phys.J.* **C72** (2012) 2074, [arXiv:1203.4495].

[81] F. Aaron *et al.* [H1 Collaboration, ZEUS Collaboration], "Combined inclusive diffractive cross sections measured with forward proton spectrometers in deep inelastic *ep* scattering at HERA," *Eur.Phys.J.* **C72** (2012) 2175, [arXiv:1207.4864].

[82] C. Marquet, "A unified description of diffractive deep inelastic scattering with saturation," *Phys.Rev.* **D76** (2007) 094017, [arXiv:0706.2682].

[83] F. Aaron *et al.* [H1 Collaboration], "Measurement of the cross section for diffractive deep-inelastic scattering with a leading proton at HERA," *Eur.Phys.J.* **C71** (2011) 1578, [arXiv:1010.1476].

[84] B. List and A. Mastroberardino, "DIFFVM: A Monte Carlo generator for diffractive processes in *ep* scattering," *Conf.Proc.* **C980427** (1998) 396–404.

[85] S. Chekanov *et al.* [ZEUS Collaboration], "Deep inelastic scattering with leading protons or large rapidity gaps at HERA," *Nucl.Phys.* **B816** (2009) 1–61, [arXiv:0812.2003].

[86] V. Andreev *et al.* [H1 Collaboration], "Measurement of dijet production in diffractive deep-inelastic *ep* scattering at HERA," *JHEP* **1503** (2015) 092, [arXiv:1412.0928].

[87] F. Aaron *et al.* [H1 Collaboration], "Measurement of dijet production in diffractive deep-inelastic scattering with a leading proton at HERA," *Eur.Phys.J.* **C72** (2012) 1970, [arXiv:1111.0584].

[88] S. Chekanov *et al.* [ZEUS Collaboration], "A QCD analysis of ZEUS diffractive data," *Nucl. Phys.* **B831** (2010) 1–25, [arXiv:0911.4119].

[89] R. Bonino *et al.* [UA8 Collaboration], "Evidence for transverse jets in high mass diffraction," *Phys.Lett.* **B211** (1988) 239.

[90] F. Abe *et al.* [CDF Collaboration], "Observation of diffractive W boson production at the Tevatron," *Phys.Rev.Lett.* **78** (1997) 2698–2703, [hep-ex/9703010].

[91] T. Sjostrand, S. Mrenna and P. Z. Skands, "A brief introduction to PYTHIA 8.1," *Comput.Phys.Commun.* **178** (2008) 852–867, [arXiv:0710.3820].

[92] S. Navin, "Diffraction in Pythia," [arXiv:1005.3894]. Available at http://arxiv.org/pdf/1005.3894.pdf.

[93] P. Bruni and G. Ingelman, "Diffractive W and Z production at $p\bar{p}$ colliders and the pomeron parton content," *Phys.Lett.* **B311** (1993) 317–323.

[94] A. Kaidalov, V. A. Khoze, A. D. Martin and M. Ryskin, "Probabilities of rapidity gaps in high-energy interactions," *Eur.Phys.J.* **C21** (2001) 521–529, [hep-ph/0105145].

[95] M. Klasen and G. Kramer, "Factorization breaking in diffractive dijet photoproduction," *Eur.Phys.J.* **C38** (2004) 93–104, [hep-ph/0408203].

[96] M. Klasen and G. Kramer, "Review of factorization breaking in diffractive photoproduction of dijets," *Mod.Phys.Lett.* **A23** (2008) 1885–1907, [arXiv:0806.2269].

[97] W. Slominski and A. Valkárová, "Diffractive final states and factorisation at HERA," in *Proceedings of the workshop HERA and the LHC*, pp. 412–420. 2009. [DESY-PROC-2009-02].

[98] R. Žlebčík, K. Černý and A. Valkárová, "Factorisation breaking in diffractive dijet photoproduction at HERA?," *Eur.Phys.J.* **C71** (2011) 1741, [arXiv:1102.3806].

[99] R. Žlebčík, "The study of diffractive dijet production in photoproduction at HERA," Master's thesis, Charles University, 2011.

[100] M. Peez, "The new object oriented analysis framework for H1," in *Proceedings of Computing in High energy and Nuclear Physics*. June, 2003. [physics/0306124].

[101] M. Jansová, "The presentation to the H1 Diffractive working group given in Apr 15, 2015 in Hamburg," 2015.

[102] L. Favart, "The presentation to the H1 Diffractive working group given in Dec 18, 2009 in Hamburg," 2009.

[103] T. Hreus, "Measurement of inclusive diffractive deep inelastic scattering using VFPS at H1," *PoS* **DIS2010** (2010) 068, [arXiv:1008.2725].

[104] M. Peez, B. Portheault and E. Sauvan, "An energy flow algorithm for hadronic reconstruction in OO: Hadroo2," *H1 internal note* (2005) 1–34. Available at http://marh1.in2p3.fr/doc/h1-0105-616.pdf.

[105] M. Cacciari, G. P. Salam and G. Soyez, "FastJet user manual," *Eur.Phys.J.* **C72** (2012) 1896, [arXiv:1111.6097].

[106] C. Adloff *et al.* [H1 Collaboration], "Inclusive measurement of diffractive deep inelastic ep scattering," *Z.Phys.* **C76** (1997) 613–629, [hep-ex/9708016].

[107] J. Jacqued and A. Blondel, "The kinematic of ep interactions," in *Study of an ep Facility for Europe*, pp. 412–420. 1979. [DESY-PROC-1979-048].

[108] S. Egli *et al.*, "Calculating event weights in case of downscaling on trigger levels 1-4," *H1 internal note* (1997) 1–6. Available at http://pia.desy.de:8136/TWDM/cgi/twdmproto.pm/h1_publ/Get/ROOT/_2/_1/_2/19981113130010/h1-0497-517.pdf.

[109] V. Blobel, "The presentation to the H1 Tracking working group given in Nov 3, 2004 in Hamburg," 2004. Available at https://www-h1.desy.de/idet/itracker/TrackingGroup/AgnMin/Meet041103/blobel041103.pdf.

[110] J. Chyla and K. Sedlak, "Dijet cross-sections in *ep* collisions: Who is afraid of symmetric cuts?," [hep-ph/0308116].

[111] F. Aaron *et al.* [H1 Collaboration], "Measurement of inclusive and dijet D^* meson cross sections in photoproduction at HERA," *Eur.Phys.J.* **C72** (2012) 1995, [arXiv:1203.1170].

[112] F. Aaron *et al.* [H1 Collaboration], "Measurement of beauty and charm photoproduction using semi-muonic decays in dijet events at HERA," *Eur.Phys.J.* **C72** (2012) 2047, [arXiv:1205.2495].

[113] A. Glazov, N. Raicevic and A. Zhokin, "Fast simulation of showers in the H1 calorimeter," *Comput.Phys.Commun.* **181** (2010) 1008–1012.

[114] J. C. Collins, "Light cone variables, rapidity and all that," [hep-ph/9705393].

[115] S. Schmitt, "Correction of detector effects: bin-by-bin and unfolding," *H1 internal note* (2011) 1–10. Available at http://www-h1.desy.de/general/home/intra_home.html.

[116] A. Tikhonov, "Solution of incorrectly formulated problems and the regularization method," *Soviet Mathematics* **4** (1963) 1035–1038.

[117] S. Schmitt, "TUnfold: an algorithm for correcting migration effects in high energy physics," *JINST* **7** (2012) T10003, [arXiv:1205.6201].

[118] G. Cowan, *Statistical data analysis*. Clarendon Press, 1998. Available at http://dfpch.ujf.cas.cz/~rusnak/statistika/literatura/Cowan.pdf.

[119] V. Blobel, "Data unfolding." https://indico.desy.de/getFile.py/access?contribId=9&sessionId=7&resId=0&materialId=slides&confId=2786, 2010. Lecture at the Terascale statistics school https://indico.desy.de/getFile.py/access?contribId=9&sessionId=7&resId=0&materialId=slides&confId=2786.

[120] P. C. Hansen, "The L-curve and its use in the numerical treatment of inverse problems," in *Computational Inverse Problems in Electrocardiology*, pp. 119–142. 2000.

[121] W. Schutte, M. Wendt and K. Mess, "The new directional coupler pick-up for the HERA proton beam position monitoring system," in *Proceedings of IEEE Particle Accelerator Conference*, vol. C870316, p. 1725. 1987.

[122] F. Aaron *et al.* [H1 Collaboration], "Measurement of the diffractive longitudinal structure function F_L^D at HERA," *Eur.Phys.J.* **C72** (2012) 1836, [arXiv:1107.3420].

[123] D. Šálek, *Measurement of the longitudinal proton structure function in diffraction at the H1 experiment and prospects for diffraction at LHC*. PhD thesis, Charles University, 2011. Available at http://www-h1.desy.de/psfiles/theses/h1th-617.pdf.

[124] R. Polifka, *Analysis of dijet events in diffractive ep interactions with tagged leading proton at the H1 experiment*. PhD thesis, Charles University, 2011. Available at http://www-h1.desy.de/psfiles/theses/h1th-655.pdf.

[125] F. Aaron *et al.* [H1 Collaboration], "Determination of the integrated luminosity at HERA using elastic QED Compton events," *Eur.Phys.J.* **C72** (2012) 2163, [arXiv:1205.2448].

[126] T. Sjostrand, L. Lonnblad and S. Mrenna, "PYTHIA 6.2: Physics and manual," [hep-ph/0108264].

[127] G. Aad *et al.* [ATLAS Collaboration], "Rapidity gap cross sections measured with the ATLAS detector in *pp* collisions at $\sqrt{s} = 7$ TeV," *Eur.Phys.J.* **C72** (2012) 1926, [arXiv:1201.2808].

[128] A. Aktas *et al.* [H1 Collaboration], "Diffractive deep-inelastic scattering with a leading proton at HERA," *Eur.Phys.J.* **C48** (2006) 749–766, [hep-ex/0606003].

[129] K. J. Golec-Biernat and A. Luszczak, "Diffractive parton distributions from the analysis with higher twist," *Phys.Rev.* **D76** (2007) 114014, [arXiv:0704.1608].

[130] A. Aktas *et al.* [H1 Collaboration], "Measurement of dijet production at low Q^2 at HERA," *Eur.Phys.J.* **C37** (2004) 141–159, [hep-ex/0401010].

[131] M. Ryskin, "Private communication about the scale variation in double ratios," 2013.